

Development of PGM-Free Catalysts for Fuel Cells Using Advanced Polymerization Techniques

Submitted in partial fulfillment of the requirements for

the degree of

Doctor of Philosophy

in

Mechanical Engineering

Rudy Martin Torres

B.S., Mechanical Engineering, University of Texas at Austin
M.S., Mechanical Engineering, Carnegie Mellon University

Carnegie Mellon University
Pittsburgh, PA

August 2021

© Rudy Martin Torres, 2021

All Rights Reserved

Acknowledgements

I would like to thank my advisor Philip R. LeDuc and my co-advisor Shawn Litster, who have been a wonderful influence on my development as a researcher. Dr. LeDuc has been an invaluable source of advice and has always kept me focused when I wanted to go on different tangents in my research. If it were not for him, I would have started many different projects and would have never finished my PhD. He has also always been able to help me, whether directly or by finding the exact person that I needed to talk to, it seemed there was no issue he could not find a solution to. Also, the fact that he allowed me the freedom to choose my own research topic and supporting me through its development. I love what I do and it has always kept me motivated and I am so thankful to have been given the freedom to choose it. Dr. Litster too, always able to give me comprehensive advice on my work, always aware of the things I need to do to improve my results and at any time willing to sit down and discuss any of the many challenges that came up. I am very thankful for all the resources he allowed me use to even though I was originally not even one of his students until later in my PhD. Both professors are always willing to put their students' success first, I was truly fortunate to have both as my mentors.

I would like to thank Dr. LeDuc and the university for having funded my graduate education through the GEM fellowship program. In addition, I'd like to thank the Nam Pyo and Young Suh Fellowship Foundation and the Mary Jane and Milton C. Shaw Fellowship Foundation for contributing to the funds.

I would also like to thank the members of my committee: Krzysztof Matyjaszewski and Reeya Jayan. Dr. Matyjaszewski allowed me into his lab despite my complete lack of experience with polymers and even though my initial results at the beginning of my PhD were anything but

stellar he remained as a pillar of support to make my project possible. I am very fortunate and thankful to have gotten his help and support. Dr. Reeja Jayan, though only included in my committee less than a year ago was also very open and willing to help when I needed to analyze the carbon of my catalyst, I am very thankful for her help.

I would also like to thank my project teammates Rui Yuan and Mingkang Sun who have been amazing at every turn. Making the complex and work-intensive copolymers, helping with TEM, TGA and BET and always having feedback. Thank you both for making my research possible through your support.

Thanks to all my past and present lab mates, I am honored to learn side by side with some amazing minds and personalities. Adam Wood, whom I always scrambled around with looking for a tube furnace. Leiming Hu and Jon Braaten who taught me everything about the fuel cells lab and who somehow always knew how to solve some issue or where to find a certain tool or material. Stephen Coyle, Utku, Andres, Susana and Justin with whom I often had lunchtime discussions in the office. Lisa Dunsmore, the person to vent stress with. Lisha White, who always has the best stories in the office. Mohamed and Zhitao for their help in testing my samples. I am glad I will get to stay a bit longer after I finish, that way I will get to enjoy their company for a little longer.

I would also like to thank my partner Jordan Bowers; it was he who always reminded me to put my dreams and aspirations of getting my PhD first and was always incredibly helpful when I was applying for graduate school. It has been a rough ride, but he has always supported me, and I am very grateful for it. My family as well, my mom and dad and three sisters and little brother, thank you both for your love and support. I especially want to thank my abuelita Chucha, who always has unrelenting trust and belief in me and whose blessings and prayers have always helped me through hard times, I love her, and I always want to make her feel proud. I only wish I could

get her to come see me walk during graduation but unfortunately, she cannot travel anymore. I love you abuelita and I dedicate this dissertation to you.

Finally, I would like to thank all the people who have helped me in many small and large ways during my time at Carnegie Mellon University. Edward Wajciechowski, William Pingitore, Laisuo Su, Marco Fantin, Zhitao Guo, Kyle Justus, Chris Hertz, Melissa Brown, etc. It has been a very intense five years but I was able to get through everything thanks to all the help from so many people.

Some of the figures, tables and text in this paper was previously included in a manuscript submitted to ACS applied Energy Materials

Abstract

Platinum Group Metal Free (PGM-Free) catalysts present a promising opportunity to make hydrogen fuel cells more affordable, however, issues with stability and electrochemical activity continue to hinder their application. Recent studies point to the availability of nitrogen and a well-defined pore structure as avenues of improvement. To address this need, copolymer templated nitrogen-enriched carbon (CTNC) was used as precursor to prepare PGM-free catalysts for oxygen reduction reaction. By employing its rich nitrogen content and interconnected, controlled porous structure, a significant amount of Fe-N-C active sites were formed by co-annealing CTNC with an iron source. The formed N/Fe co-doped nanocarbon (CTNC-Fe) catalyst exhibits high electrochemical activity in oxygen reduction reaction (ORR) under acidic conditions and can function remarkably well as a catalyst in fuel cell under standard procedures. FeN_x active sites were detected and the nanostructure of CTNC was retained despite the various processing steps involved during synthesis.

The use of CTNC allows for control of the pore morphology of the catalyst using controlled/ “living” radical polymerization to synthesize the block copolymer (BCP) precursor. This allowed a greater level of control in tuning the formation of active sites, their energy activation barrier and therefore the electrochemical activity of the catalyst. The interaction between pore morphology and formation of active sites remains unclear, even though the produced catalysts were confirmed to be influenced significantly by the composition and degree of polymerization of the BCP precursors.

This work describes a novel and revolutionary method of PGM-free catalyst synthesis using advanced polymerization techniques. Much work remains to be done in improving and

optimizing the methods of synthesis of the catalyst. This includes improving the Fe-doping process either by use of standard procedures with transition metal salt precursors or by a newly developed method presented in this work using poly(vinyl ferrocene), an iron containing metallopolymer. In addition, further experimentation with different CTNCs made by varying the composition and degree of polymerization. At any rate, the catalyst presented here has already reached a level of electrochemical activity competitive with other PGM-free catalysts (half-wave potential of 0.8 V vs NHE) and presents a new approach to the development and scalability of affordable fuel cells as a sustainable clean energy alternative.

Table of Contents

Acknowledgements	i
Abstract.....	iv
List of Figures.....	x
List of Tables	xv
Chapter 1: Introduction.....	1
1.1 Motivation	1
1.2 Thesis Statement	6
1.3 Organization.....	7
Chapter 2: Development of a Reliable Fe-Doping Process	8
2.1 Introduction.....	8
2.2 Materials and Methods	8
2.2.1 Materials	8
2.2.2 Synthesis and Characterization of PAN ₁₀₃ - <i>b</i> -PBA ₆₀	9
2.2.3 Methods: Electrochemical Activity Measurements	10
2.2.4 Methods: Pore size characterization.....	13
2.2.5 Methods: Initial Iteration of CTNC-Fe Synthesis	13
2.3 The Effects of Iron Component Source and Concentration.....	14
2.3.1 Effects of Iron Component Source.....	14
2.3.2 Effects of Iron Precursor Concentration	16
2.4 The Effects of Heat Treatment Temperature.....	18
2.4.1 Effects of first Heat Treatment Temperature and Duration.....	18

2.4.2 Effects of Second Heat Treatment Temperature	21
2.5 The Effects of Gas Flow Conditions During Heat Treatment	23
2.6 The Effects of Fe-doping before and after Carbonization of CTNC	27
2.7 Summary on the Optimization of CTNC-Fe	30
2.7.1 Summary of Results	30
2.7.2 Comparison of Pristine CTNC and CTNC-Fe catalyst	32
2.7.3 Latest Iteration of CTNC-Fe Synthesis Process Using Fe Salts.....	33
Chapter 3: Materials Characterization and Fuel Cell Testing of CTNC-Fe Catalyst.....	35
3.1 Abstract	35
3.2 Introduction	36
3.3 Experimental Section	40
3.3.1 Materials	40
3.3.2 Preparation of PAN-b-PBA copolymers.....	41
3.3.3 Preparation of CTNC-Fe Catalyst.....	42
3.3.4 Testing Electrochemical Activity.....	42
3.3.5 Materials Characterization	43
3.3.6 Fuel Cell Testing.....	43
3.4 Results and Discussion.....	44
3.4.1 Morphology and Porosity of the Catalyst	44
3.4.2 Elemental Analysis and the Influence of Fe-doping	49
3.4.3 Electrochemical Activity and Fuel Cell Performance	56
3.5 Conclusions	61
Chapter 4: Using Poly(vinyl-ferrocene) Metallopolymer as an Iron Precursor in CTNC-Fe Catalyst Synthesis	63

4.1 Introduction	63
4.2 Experimental Section	65
4.2.1 Materials	65
4.2.2 Preparation of PAN-b-PBA copolymers	65
4.2.3 Preparation of CTNC-Fe and CTNC-vFe Catalysts	65
4.2.4 Testing Electrochemical Activity	68
4.2.5 Materials Characterization	68
4.3 Results and Discussion	69
4.3.1 Electrochemical Activity Results	69
4.3.2 Chemical Composition Analysis	72
4.3.3 Morphology and Porosity	73
4.4 Conclusions and Future Work	75
Chapter 5: The Effects of Pore Morphology on CTNC-Fe Catalyst Electrochemical Performance	77
5.1 Introduction	77
5.2 Experimental Section	78
5.2.1 Materials	78
5.2.2 Preparation of PAN-b-PBA copolymers	79
5.2.3 Preparation of CTNC-Fe Catalysts	79
5.2.4 Testing Electrochemical Activity	80
5.2.5 Materials Characterization	80
5.3 Results and Discussion	81
5.3.1 Electrochemical Activity	81
5.3.2 Catalyst Porosity and Morphology	82

5.3.3 Elemental Composition of CTNC-Fe Catalysts	86
5.4 Conclusion.....	90
Chapter 6: Conclusions.....	92
6.1 Overview	92
6.2 Contributions.....	94
6.3 Future Work	96
6.3.1 Using Additional Nitrogen Source in the Synthesis.....	97
6.3.2 Use of Surface Area Activation Methods	98
6.3.3 Reducing Catalyst Particle Size	99
6.3.4 Composition Analysis of CTNC-Fe Catalysts	99
6.3.5 Fuel Cell Testing.....	100
6.3.6 Testing Other BCP Degrees of Polymerization	100
6.3.7 Optimization of Fe-doping Process for each Type of CTNC.....	101
6.3.8 Optimization of the Fe-doping Process using Poly(vinyl-ferrocene).....	101
References	102

List of Figures

Figure 1.1. Molecular structures of different transition metal active sites coordinated by nitrogen atoms in a graphitic carbon plane.....2

Figure 1.2. Quantum chemically optimized structure of Cytochrome C Oxidase binuclear center with bound O₂ molecule. The silver atom represents iron, coordinated by the four nitrogen atoms of a heme molecule and the orange atom represents copper bound by histidine.....3

Figure 2.1. (a) ¹H NMR spectrum and (b) GPC trace of PAN₁₀₃-*b*-PBA₆₀ block copolymer. PMMA calibration with DMF as solvent was used to analyze GPC curve, and d-DMSO is the solvent to confirm the composition of the block copolymer.....10

Figure 2.2. Electrochemical test results obtained from RDE potentiometry for catalysts with different iron sources a) Linear sweep voltammetry b) Cyclic voltammetry.....16

Figure 2.3. Electrochemical test results obtained from RDE potentiometry for catalysts with different iron concentrations and no post-treatment a) Linear sweep voltammetry b) Cyclic voltammetry.....18

Figure 2.4. Electrochemical test results obtained from RDE potentiometry for catalysts with different temperature heat treatment a) Linear sweep voltammetry b) Cyclic voltammetry.....20

Figure 2.5. Electrochemical test results obtained from RDE potentiometry for catalysts heat treated at 600°C with different duration a) Linear sweep voltammetry b) Cyclic voltammetry.....21

Figure 2.6. Electrochemical test results obtained from RDE potentiometry for catalysts heat treated at 900°C with different 2nd heat treatment protocols a) Linear sweep voltammetry b) Cyclic voltammetry.....23

Figure 2.7. Electrochemical test results obtained from RDE potentiometry for catalysts heat treated at 900°C with different N₂ flow rates a)-b) Linear sweep voltammetry c)-d) Cyclic voltammetry.....26

Figure 2.8. RDE potentiometry and BET surface area results for samples of Fe-doping before and after carbonization. a) Linear sweep voltammetry curve obtained at room temp under oxygen flow at 900 rpm, b) Cyclic voltammetry curve obtained at room temp with nitrogen flow and 200 rpm, c) adsorption-desorption isotherms at -196 °C, and d) Pore width distribution.....28

Figure 2.9. Summary of results for all optimization experiments a) Half-wave potential b) Capacitive surface area.....31

Figure 2.10. ORR electrochemical activity curves of CTNC-Fe (Fe-N-C) vs. P-CTNC in 0.5 M H₂SO₄ solution under oxygen flow at room temperature obtained using chronoamperometry scans at 900 rpm.....32

Figure 3.1. Preparation of CTNC-Fe from PAN-*b*-PBA copolymer.....39

Figure 3.2. TEM photographs of pristine CTNC and CTNC-Fe catalyst at different stages during synthesis. a) Pristine CTNC (P-CTNC), b) CTNC-Fe Catalyst, c) CTNC-Fe after first heat treatment at 600 °C, and d) CTNC-Fe after acid treatment.....45

Figure 3.3. TEM scan photographs of CTNC-Fe during various stages of the synthesis process. a) CTNC-Fe after heat treatment at 600 °C for 30 mins, b) CTNC-Fe after treatment in 0.5 M H₂SO₄ solution at 80 °C, and c) Completed CTNC-Fe catalyst, after 900 °C heat treatment for 3 hours....46

Figure 3.4. BET surface area analysis results for a)-b) CTNC-Fe catalyst and pristine CTNC (P-CTNC), c)-d) CTNC-Fe during the synthesis process and e)-f) pristine CTNC heat treated at 600 °C. Nitrogen adsorption-desorption isotherms at -196 °C on the left and pore size distribution on the right.....48

Figure 3.5. High resolution XPS spectra of a) CTNC-Fe N 1s, b) CTNC-Fe Fe 2p, c) CTNC-Fe-600 N 1s, d) CTNC-Fe-AT N 1s, e) CTNC-600 and f) P-CTNC N 1s. Peak shape of Gaussian/Lorentzian convolve was used for the fitting, with a L/G Mix ratio of 30% for all peaks.....	50
Figure 3.6. Energy dispersive x-ray spectroscopy (EDS) scan of CTNC-Fe at three steps during synthesis a) CTNC-Fe, b) CTNC-Fe-600, and c) CTNC-Fe-AT.....	52
Figure 3.7. SEM photograph scans of the particle size and structure of a) P-CTNC and b) CTNC-Fe.....	53
Figure 3.8. High resolution XPS S 2p spectra for CTNC-Fe at different steps during synthesis....	54
Figure 3.9. High resolution XPS C 1s spectra for CTNC-Fe at different steps during synthesis and pristine CTNC.....	55
Figure 3.10. XRD profile of CTNC-Fe catalyst with labeled diffraction peaks for detecting π -stacking of nanographitic platelets (002) and assessing their lateral size (100).....	56
Figure 3.11. Electrochemical activity results on ORR of the CTNC-Fe catalyst tested at different steps in the synthesis process. a) Polarization curve of ORR in acidic environment obtained using chronoamperometry scans in oxygen saturated 0.5 M H ₂ SO ₄ solution at room temperature. b) Cyclic voltammetry curve obtained in nitrogen saturated 0.5 M H ₂ SO ₄ solution at room temperature.....	57
Figure 3.12. Results of fuel cell tests performed using a 4 mg/cm ² CTNC-Fe cathode and 0.3 mg/cm ² anode at 80 °C, 100% relative humidity, 50 kPa backpressure hydrogen in the anode and either a) 100% relative humidity, 50 kPa backpressure oxygen or b) 100% relative humidity, 50 kPa backpressure air in the anode.....	58

Figure 3.13. Potentiostatic electrochemical impedance spectroscopy scan of membrane electrode assembly with CTNC-Fe catalyst.....	59
Figure 3.14. Cyclic voltammetry curve of fuel cell with CTNC-Fe cathode performed using N ₂ flow with 100% RH at 80 °C with 50 kPa backpressure.....	60
Figure 4.1. Summary RDE potentiometry results for CTNC-vFe samples with varied AIBN initiator concentrations. a) Half-wave potential results (V vs NHE) performed in 0.5 M H ₂ SO ₄ solution under O ₂ flow at 900 rpm b) Capacitive surface area results performed in 0.5 M H ₂ SO ₄ solution under N ₂ flow at 200 rpm.....	70
Figure 4.2. Summary RDE potentiometry results for CTNC-vFe samples with varied monomer concentration and Fe mass content a) Half-wave potential results (V vs NHE) performed in 0.5 M H ₂ SO ₄ solution under O ₂ flow at 900 rpm b) Capacitive surface area results performed in 0.5 M H ₂ SO ₄ solution under N ₂ flow at 200 rpm.....	70
Figure 4.3. Comparison of RDE potentiometry results for CTNC-vFe and CTNC-Fe. a) Half-wave potential obtained in 0.5 M H ₂ SO ₄ solution in O ₂ flow at 900 rpm. b) Capacitive surface area obtained in 0.5 M H ₂ SO ₄ solution in N ₂ flow at 200 rpm.....	71
Figure 4.4. XPS high resolution spectra of CTNC-vFe and CTNC-Fe catalysts. a) CTNC-vFe N 1s spectrum, b) CTNC-vFe Fe 2p spectrum, c) CTNC-Fe N 1s spectrum, and d) CTNC-Fe Fe 2p spectrum.....	72
Figure 4.5. TEM images of a) CTNC-vFe and b) CTNC-Fe.....	74
Figure 5.1. Electrochemical activity results on ORR of CTNC-Fe catalysts made with different BCP compositions. a) Polarization curve of ORR in acidic environment obtained using chronoamperometry scans in oxygen saturated 0.5 M H ₂ SO ₄ solution at room temperature. b)	

Cyclic voltammetry curve obtained in nitrogen saturated 0.5 M H₂SO₄ solution at room temperature.....81

Figure 5.2. BET surface area analysis results for pristine CTNC and CTNC-Fe catalysts. a) Pore width distribution for CTNC-Fe catalysts, b) adsorption-desorption isotherms for CTNC-Fe catalysts, c) Pore width distribution for pristine CTNCs, and d) adsorption-desorption isotherms for pristine CTNCs.....83

Figure 5.3. Performance and BET results comparison for CTNC-Fe catalysts synthesized using different BCP degrees of polymerization (DP). a) Electrochemical activity, b) Peak and average pore sizes, c) Total, mesopore and micropore surface area values, and d) Total pore volumes.....84

Figure 5.4. TEM images of the pore morphology of CTNC-Fe catalysts synthesized from different BCP compositions. a) PAN₆₀-*b*-PBA₃₇, b) PAN₇₆-*b*-PBA₄₇, c) PAN₁₀₃-*b*-PBA₆₀ and d) PAN₁₆₅-*b*-PBA₉₉.....85

Figure 5.5. High resolution N 1s XPS spectra for CTNC-Fe catalysts. a) PAN₆₀-*b*-PBA₃₇, b) PAN₇₆-*b*-PBA₄₇, c) PAN₁₀₃-*b*-PBA₆₀ and d) PAN₁₆₅-*b*-PBA₉₉.....87

Figure 5.6. High resolution Fe 2p XPS spectra for CTNC-Fe catalysts. a) PAN₆₀-*b*-PBA₃₇, b) PAN₇₆-*b*-PBA₄₇, c) PAN₁₀₃-*b*-PBA₆₀ and d) PAN₁₆₅-*b*-PBA₉₉.....88

Figure 6.1. Electrochemical performance of other PGM-free catalysts currently under development. The red line represents the highest performance of CTNC-Fe. a) Half-wave potentials, b) Mass Activities.....94

List of Tables

Table 2.1. Electrochemical activity results for tests on iron component source.....	15
Table 2.2. Electrochemical activity results for tests on effects of iron concentration with no post-processing.....	17
Table 2.3. Electrochemical activity results for tests performed on catalyst samples heat treated at different temperatures.....	19
Table 2.4. Electrochemical activity results for tests performed on catalyst samples heat treated at 600°C with different duration.....	20
Table 2.5. Electrochemical activity results for tests performed on catalyst samples heat treated at 900°C with different second heat treatment protocols.....	22
Table 2.6. Electrochemical activity results for tests performed on catalyst samples heat treated with different N ₂ flow rates.....	25
Table 2.7. Summary of BET surface area analysis results for CTNC-Fe samples synthesized with Fe-doping step performed before and after carbonization of CTNC. The P-CTNC sample refers to pristine CTNC without any Fe-doping or any other process done to the CTNC-Fe samples other than similar heat treatment.....	29
Table 2.8. Summary of results for synthesis optimization experiments of CTNC-Fe.....	31
Table 3.1. BET surface area analysis results for CTNC-Fe catalyst after first heat treatment (CTNC-Fe-600), after acid treatment (CTNC-Fe-AT) and after completion of the synthesis process (CTNC-Fe). P-CTNC-600 is pristine CTNC with similar heat treatment to CTNC-Fe-600 and P-CTNC has similar heat treatment to CTNC-Fe.....	47

Table 3.2. Nitrogen species amounts calculated from N 1s deconvoluted peaks analysis for CTNC-Fe and pristine CTNC.....	51
Table 3.3. Elemental composition of CTNC-Fe catalyst throughout the synthesis process and pristine CTNC.....	51
Table 3.4. C 1s deconvoluted peaks analysis for CTNC-Fe and pristine CTNC.....	56
Table 4.1. List of vFe monomer solutions prepared for experiment in CTNC-vFe synthesis.....	66
Table 4.2. List of different CTNC-vFe samples synthesized with different solutions, volumes, and Fe amounts.....	67
Table 4.3. Surface elemental composition of CTNC-vFe and CTNC-Fe catalysts obtained using XPS.....	73
Table 4.4. BET surface area analysis results for CTNC-vFe and CTNC-Fe catalysts.....	74
Table 5.1. RDE potentiometry results for the CTNC-Fe catalysts synthesized using different BCP compositions.....	82
Table 5.2. BET surface area analysis results for pristine CTNCs and CTNC-Fe catalysts.....	82
Table 5.3. CTNC-Fe surface elemental composition according to 200 eV scan using XPS.....	86
Table 5.4. Binding energy values for deconvoluted peaks of Fe 2p XPS spectra.....	89
Table 5.5. Fe content of CTNC-Fe catalysts made from different BCP compositions obtained from TGA.....	90

Chapter 1: Introduction

1.1 Motivation

Over the years, researchers have actively explored new sustainable energy sources and energy conversion systems to deal with the increasing demand for clean energy and concerns over global climate change.¹ From the available renewable energy sources, solar and wind are the most abundant and readily accessible.² However, to be able to rely on these energy sources, the development of efficient electrochemical energy conversion and energy storage processes is essential.³ One such example of a sustainable and non-polluting energy storage compound is H₂ which can be used in both mobile and stationary power generation.⁴ It has a specific energy density of 143 MJ/kg which is almost three times higher than hydrocarbon fuel cells like natural gas (53.6 MJ/kg) and gasoline (46.4 MJ/kg).⁵ Moreover, it can be produced from renewable energy sources such as by electrolysis using solar and/or wind energy⁶ and can be directly converted into electrical energy through electrochemical conversion in fuel cells which curtails the limits of Carnot efficiency by the heat engine. This is achieved through two electrochemical reactions: the hydrogen oxidation reaction (HOR) and the oxygen reduction reaction (ORR) which are possible through use of polymer-electrolyte fuel cells (PEFC). However, one important drawback to fuel cells is the sluggish kinetics of ORR which can only, for the most part, be catalyzed reliably by using platinum group metals (PGM).⁵ This understandably limits mass application of PEFCs as the cost of the catalyst for fuel cells is approximately 41% compared to the rest of the fuel cell pack according to the U.S. Fuel Cell Technologies Office.⁷ To address the limitation caused by the cost of catalysts, development of low cost PGM-free catalysts produced from inexpensive,

abundant, and easily sourced materials like transition metals, nitrogen and carbon has been the most feasible option.⁸⁻²⁰

The discovery of ORR activity of cobalt phthalocyanine by Jasinski in 1964 was the first instance of use of macromolecules such as phthalocyanine and porphyrin which contain CoN_4 and FeN_4 .²¹ These transition metal-nitrogen centers and other similar configurations (seen in Fig. 1.1) have become the pivotal component around which a great deal of research has been performed as they act as catalytic active sites that can successfully perform ORR in an acidic environment.⁸⁻²⁰

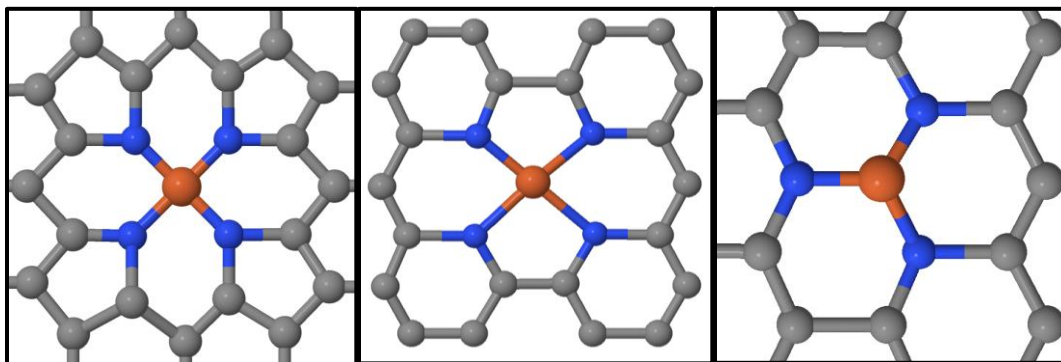


Figure 1.1. Molecular structures of different transition metal active sites coordinated by nitrogen atoms in a graphitic carbon plane.

Perhaps one of the best examples of the ability of this type of macromolecules to perform ORR can be seen in the binuclear center of cytochrome c oxidase (seen in Fig. 1.2), the last transmembrane enzyme in the line of proteins of the cellular respiratory chain of mitochondria membranes in animal cells.²² Although ORR entails the transfer of 4 electrons and the breakage of a double bond, the reasons why ORR can be so sluggish, the binuclear center is able to reduce oxygen one electron and proton at the time without releasing oxygen radicals, hydroxide ions or hydrogen peroxide, which are all toxic intermediates of the reaction that if released could poison the environment inside the cell. However, the binuclear center which is composed of an iron ion

coordinated by four nitrogen atoms and a copper ion bound by a histidine amino acid, separated by 2.48 Å, can fully bind the oxygen until the last electron and proton is transferred.²² The binuclear center is asymmetric for this reason, as there is only one direction for the reaction to take place (as seen in Eq. 1-5) and the surrounding part of the enzyme shuttle the necessary electrons and protons one at a time at the exact time to keep the reaction moving forward and prevent backward reactions.

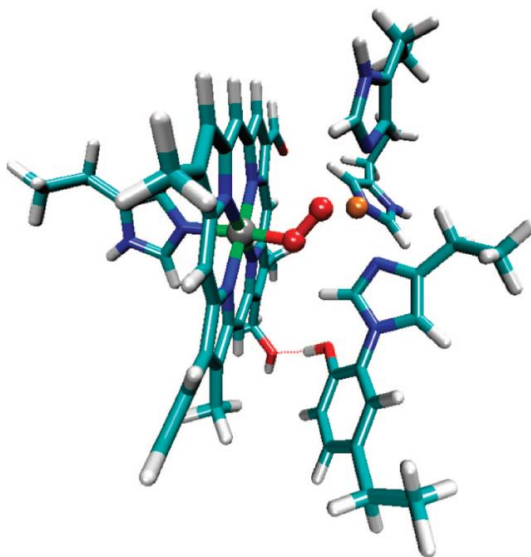
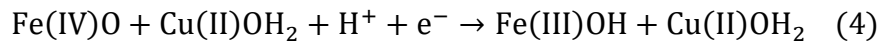
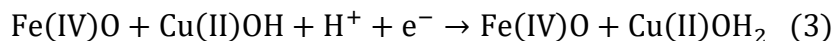
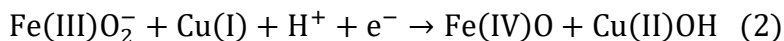
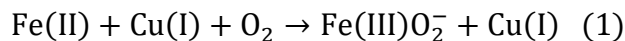
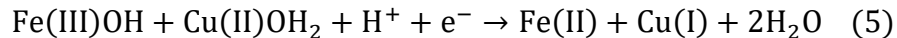


Figure 1.2. Quantum chemically optimized structure of Cytochrome C Oxidase binuclear center with bound O₂ molecule. The silver atom represents iron, coordinated by the four nitrogen atoms of a heme molecule and the orange atom represents copper bound by histidine.²²





Although perfect control of ORR as seen in cytochrome c oxidase is virtually impossible to recreate, the process can still be approximated and with enough control and under the right conditions a catalyst that works for PEFCs is possible. To make a working catalyst a high density of active sites is necessary, so a high surface area is required. Furthermore, availability of electrons and reactants is needed so an electrically conductive mesoporous area is necessary. To meet all these requirements a great deal of control must be achieved during synthesis of the catalyst. Indeed, many synthesis methods have been developed and continue to be optimized in order to approach and/or match the catalytic activity of PGMs.⁸⁻¹⁶

Although phthalocyanines and porphyrins contain the desired molecular structure as active sites, the lack of electrical conductivity resultant from the structure of the macromolecule makes use as a catalyst in electrodes for fuel cells insufficient as the ORR results in irreversible reactions such as formation of iron oxide and quick degradation of the active sites.^{8,21} Synthesis of the catalyst, therefore, tends to include nitrogen, transition metals such as iron or cobalt, and carbon precursors which under heat treatment at temperatures above 600°C generate mesoporous, electrically conductive carbon rich in nitrogen with transition metal (M-N_x) moieties which act as active sites; these PGM-free catalysts are generally named M-N-C catalysts.⁸⁻²⁰

There are three major methods of synthesis for producing M-N-C catalysts:

- 1) Carbon-Based: One of the earliest methods used for synthesis of TM-N-C relied heavily on a high surface, electrically conductive carbon such as Ketjenblack,²³ Vulcan XC72,²⁴ Black Pearls,²⁵ acetylene black,²⁶ carbon nanotubes,²⁷ reduced graphene oxide²⁸ and ordered mesoporous carbons²⁹ used as a base for the formation of active sites. The carbon

can be pre-treated with nitrogen compounds such as nitric acid or ammonia gas during temperature treatment to form nitrogen moieties on the carbon surface. Small organic compounds rich in nitrogen such as phenanthroline, melamine, hexamethylene diamine, urea, cyanamide, etc. are then mixed into the carbon in conjunction with transition metal salt to be able to form $M-N_x$ moieties after high temperature treatment.¹⁵

- 2) Polymer Based: In this synthesis approach, the carbon and nitrogen come from a polymer although some carbon support such as carbon nanotubes, Vulcan XC72 or Ketjen Black is sometimes used. The polymer is used as the nitrogen and carbon source and a metal salt is included in the precursor mixture. Electroconductive polymers are usually the choice although other types such as polyacrylonitrile, polyamides, and porous organic polymers can also be used.³⁰⁻³⁷
- 3) Metal-Organic Framework Based: Metal organic frameworks (MOFs) are one of the latest discoveries in their use as a template and precursor for TM-N-C catalysts. The solvothermal reaction of nitrogen containing cyclic compounds like imidazolate and transition metal containing salts like acetates or nitrides generates a zeolitic imidazolate framework where the transition metal ions are directly coordinated by four nitrogen atoms which when heat treated at temperatures above 500°C generate a carbon surface with uniformly scattered $M-N_x$ moieties.³⁸⁻⁴³

Although all these methods have their advantages, in over 25 years of research no catalyst has been able to completely match the electrochemical activity of Pt/C catalysts despite significant progress in development. Therefore, a new approach to the development of M-N-C catalyst is prudent. One major drawback in the processes mentioned before is the lack of control over pore

size and structure. This lack can be an impediment for forming a high density of active sites, as their formation is greatly influenced by the size and structure of the pores.⁴⁴⁻⁴⁹

1.2 Thesis Statement

Copolymer templated nitrogen rich carbons can be used as a base for M-N-C fuel cell catalysts; their tunable nanostructure achieved by their synthesis through atom transfer radical polymerization could serve to tailor the formation of M-N_x active sites and therefore continuously improve the electrochemical activity of the resultant M-N-C catalyst.

This thesis will be supported by two main stages of work. The first one focuses on the development of a reliable synthesis process to use on copolymer templated nitrogen rich carbon to produce a working and significantly electrochemically active M-N-C fuel cell catalyst. The optimization of the synthesis process was performed and certain major synthesis variables affecting catalyst performance were found. Furthermore, the characterization of the best performing catalyst was done by using different materials characterization techniques to measure chemical composition, carbon chemical structure, mesoporous structure, presence and identity of moieties, and electrochemical activity. This was finally proved by testing in an actual fuel cell hardware assembly with hydrogen, oxygen and air gas flows.

The second stage introduces the effects of varying the carbon nanostructure by varying the composition of the block copolymer precursor. This variation depends on the control afforded using controlled/“living” radical polymerization (in this case atom transfer radical polymerization) and we measure the effects by testing electrochemical activity, mesoporous structure, chemical composition and presence and identity of moieties.

1.3 Organization

The organization of this dissertation is as follows. Chapter 2 provides background on M-N-C catalysts and information on the optimization of the synthesis process of the catalyst using CTNC (named CTNC-Fe) obtained from a singular composition of block copolymer precursor (PAN₁₀₃-b-PBA₆₀) which includes major synthesis variables and their effects on catalyst performance measured using RDE potentiometry. Chapter 3 provides a thorough characterization of the best CTNC-Fe catalyst found in Chapter 2 using various techniques including XPS, TEM, SEM, BET, XRD and fuel cell hardware. Chapter 4 presents the use of a metallopolymer as an iron source for the synthesis of CTNC-Fe catalyst. Chapter 5 presents an introduction to the effects of the variability of CTNC structure and its effects on catalyst performance. Finally, Chapter 6 provides an overall summary of the work, this work's contributions to science and includes future work.

Chapter 2: Development of a Reliable Fe-Doping Process

2.1 Introduction

Use of copolymer templated nitrogen rich carbon as a base for the PGM-free catalyst, CTNC-Fe, is a novel method of synthesis, therefore, to obtain a working catalyst was a matter of rigorous experimentation with various synthesis methods and sometimes light variation of synthesis variables such as concentration, temperature, gas flow, etc. Herein, is a presentation of some of the major variables affecting the electrochemical activity of the catalyst. Various experiments are presented to inform the reader of the systematic method used to improve the catalyst performance purely by the process of transition metal doping. Because of the volume of samples tested, most of this experimentation was performed by only testing the electrochemical activity of the catalyst samples in an acidic environment. The initial and latest iterations of the synthesis process are described at the beginning and end of this chapter.

2.2 Materials and Methods

2.2.1 Materials

Azobisisobutyronitrile (AIBN), dimethylsulfoxide (DMSO), dimethylformamide (DMF) CuBr_2 , tris(2-pyridylmethyl)amine (TPMA), acrylonitrile (AN), bipyridine nitrate (BPN), n-butyl acrylate (BA), HCl, methanol, ultrapure water, $\text{FeSO}_4 \cdot 7\text{H}_2\text{O}$, 0.5 M sulfuric acid aqueous solution, Nafion 5 wt% solution and ultra-pure water were used. All materials were obtained from Millipore

Sigma. CuBr₂ was purified by stirring in glacial acetic acid followed by washing with ether and dried overnight under vacuum. Monomers were passed through alumina column prior to use.

2.2.2 Synthesis and Characterization of PAN₁₀₃-*b*-PBA₆₀

The BCP chosen to perform all optimization experiments was PAN₁₀₃-*b*-PBA₆₀. PAN₁₀₃ was synthesized by initiator for continuous activator regeneration (ICAR) ATRP using a previously reported technique.⁵⁰ In a typical procedure, 17 mg of AIBN (0.1 mmol, 0.1 equiv.), 30 mL of DMSO and 3 mL of DMF were charged into a Schlenk flask and degassed with N₂ for 30 min. A stock solution of CuBr₂ and 3 mL of DMF was prepared and degassed for 10 min, then 9 mg (0.04 mmol, 0.04 equiv.) of CuBr₂, 36 mg (0.12 mmol, 0.12 equiv.) of TPMA were added to the Schlenk flask. 27 mL (415 mmol, 400 equiv.) of degassed AN was added to the above flask, and finally 139 mg (1.0 mmol, 1 equiv.) of BPN was added and the polymerization was started by immersing the flask in an oil bath at 65 °C and conducted for 5 h to reach 26% conversion. The final polymer was isolated by precipitation resulting from addition of the reaction mixture to methanol/water (4:1, v/v), and dried under vacuum at room temperature overnight.

PAN₁₀₃-*b*-PBA₆₀ block copolymer was synthesized by supplemental activator reducing agent atom transfer radical polymerization (SARA ATRP) developed previously.^{45,46} Using this approach, 5 g (0.9 mmol, 1 equiv.) of PAN-Br macroinitiator (M_n, NMR = 5600) was dissolved in 50 mL of DMF. The solution was then added to a 100 mL Schlenk flask containing 1.5 mg of CuBr₂ (0.0067 mmol, 0.0075 equiv.) and 5.8 mg of TPMA (0.02 mmol, 0.0225 equiv.) and bubbled with nitrogen for 20 min. 19 mL of deoxygenated BA (134 mmol, 150 equiv.) was then carefully added under vigorous stirring to prevent PAN precipitation. Cu wire (8 cm length x 1 mm diameter), previously cleaned with HCl: MeOH solution (1:1, v/v) was added to start polymerization at room temperature. The reaction was stopped after 4.2 h with conversion reaching

40%. The resulting block copolymer was precipitated by adding the reaction solution to methanol/water (6:4, v/v), then it was filtered and dried under vacuum overnight. Figure 2.1a demonstrates that the composition of the BCP to be PAN₁₀₃-*b*-PBA₆₀ by integration of peak b and e. GPC trace (Fig. 2.1b) shows a low molecular weight distribution ($M_w/M_n = 1.24$) manifesting excellent control over polymerization.

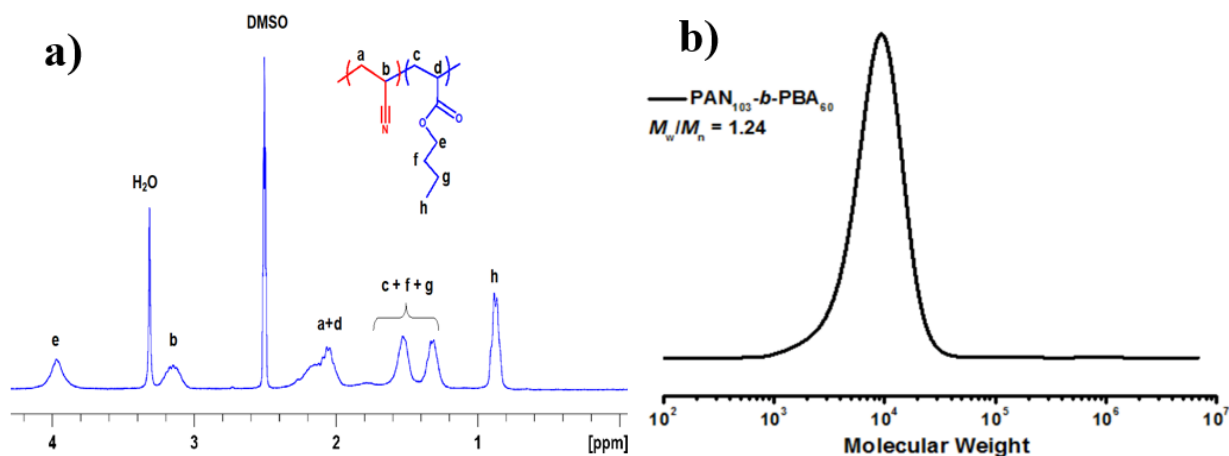


Figure 2.1. (a) ¹H NMR spectrum and (b) GPC trace of PAN₁₀₃-*b*-PBA₆₀ block copolymer. PMMA calibration with DMF as solvent was used to analyze GPC curve, and d-DMSO is the solvent to confirm the composition of the block copolymer.

2.2.3 Methods: Electrochemical Activity Measurements

Initially, the catalyst samples were tested in a fuel cell assembly. Each sample was cast onto gas diffusion layer paper to create a cathode. The ink was prepared by mixing 25 mg of catalyst, 65 mg of 5% Nafion solution in a mixture of 25 μ L deionized water, 175 μ L isopropanol and 300 μ L ethanol. The ink was sonicated in an ice bath for 2 hours then it was drop-casted onto the gas diffusion layer until achieving a catalyst loading of approximately 2 mg/cm². After drying at 80°C in air, the electrode was cold pressed on Nafion 115 electrolyte membrane as a cathode with a 0.3 mg/cm² 40% Platinum on Vulcan carbon paper electrode as anode to make a membrane

electrode assembly. The fuel cell was subjected to a two-hour heating period for the fuel cell to reach steady state at 80°C while flowing 100% relative humidity nitrogen gas. During testing 100% relative humidity oxygen was flowed through the cathode while 100% relative humidity hydrogen gas was flowed through the anode. The fuel cell was held at 0.5 V for 1 hour to get rid of any unreacted irreversible species, then a chronoamperometry scan was performed at 50 mV steps from 0 to 1 V vs NHE.

Although acquiring direct fuel cell electrochemical activity data was a direct method to test the performance of the catalyst in close to real-life applications, the mass required to cast fuel cell electrodes severely limited the number of samples that could be synthesized since the availability of BCP is limited. Furthermore, issues resulting from mass transport and ohmic overpotential, which are difficult to predict when casting electrodes and assembly a fuel cell by hand, sometimes caused issues when attempting to compare catalyst performance. Each catalyst type usually must go through its own optimization process when testing application on a fuel cell configuration. Therefore, fuel cell testing was replaced by RDE potentiometry testing platform. Data obtained from fuel cell tests can be accessed from the link provided in Supporting Information.

Measurements of electrochemical activity were obtained using rotary disk electrode (RDE) potentiometry. An ink was prepared using 5 mg of catalyst with 40 μL of 5% Nafion solution in alcohol dissolved in 0.5 mL n-propanol. The ink was sonicated in an ice bath for 1 hour and an aliquot of 17 μL was casted onto the polished glassy carbon electrode for a 0.8 mg/cm^2 catalyst loading. A 0.5 M sulfuric acid solution at room temperature with a mercury/mercurous sulfate reference electrode and a graphite counter electrode was used. Cyclic voltammetry was implemented from 0 to 1 V (vs. NHE) in 50 mV/sec steps at 200 rpm in nitrogen flow and chronoamperometry scans were ran at 50 mV per 30 second steps at 900 rpm under oxygen flow.

There were two major properties from the RDE Potentiometry tests that were extracted and taken into consideration for quantifying the electrochemical activity of each sample; these were the half-wave potential ($E_{1/2}$) obtained from the linear sweep voltammetry which was obtained from the chronoamperometry scans and capacity surface area (CSA) obtained from cyclic voltammetry scans performed under nitrogen flow. $E_{1/2}$ was used to estimate the level of ORR activation overpotential for the catalyst as conditions in the RDE testing environment minimize issues of ohmic and mass transport overpotential.⁵¹ From the chronoamperometry scan, the last 30% of data points from each sustained voltage step (chosen to give each voltage step time to stabilize and reach steady state) were averaged out into one current value. Data was then assembled into a linear sweep voltammetry graph and values of minimum (I_{Min}) and limiting current (I_{Lim}) were extracted and averaged out to obtain $E_{1/2}$ as shown by Eq. 6.

$$E\left(\frac{I_{Lim} + I_{Min}}{2}\right) = E_{1/2} \quad (6)$$

Capacitive surface area was obtained from cyclic voltammetry curves as shown by Eq. 7.⁵²

$$CSA = \frac{i}{vmAC_{GC}} \quad (7)$$

where A stands for geometric area of the glassy carbon electrode (cm^2), i is double layer current at 0.4 V (vs. NHE) in 0.5 M H_2SO_4 solution (mA), v is potentiometer scan rate (mV/s), m is catalyst loading (g/cm^2), and C_{GC} is double layer capacitance of glassy carbon electrode ($0.2 \text{ F}/\text{m}^2$).

Different properties such as onset potential and I_{Lim} were also taken into consideration when deciding the best catalyst performance, however, when catalysts showed very similar properties the mass activity⁵³ (A_{mass}) of a catalyst was examined and compared between different catalysts. A_{mass} can be calculated by dividing the current density averaged at 0.85V of the linear

sweep voltammetry curve by the mass density of catalyst casted on the rotating disk electrode surface as shown by Eq. 8.

$$A_{mass} = \frac{i(E = 0.85 V)}{m_{catalyst}} \quad (8)$$

For most catalyst samples, multiple electrodes were tested and, in some cases, multiple inks and separate electrodes were tested to avoid confusion due to effects of electrode roughness and ink catalyst concentration differentials.

2.2.4 Methods: Pore size characterization

This method was only used later in the process of optimization of the synthesis of CTNC-Fe, when comparing the performance of CTNC-Fe samples made with Fe-doping process before and after carbonization at the first heat treatment. The surface area and pore size were measured using Brunauer-Emmett-Teller (BET) surface area analysis. Powder samples were first degassed at 120 °C for at least 4 hours before N₂ sorption measurement. The micropores were analyzed using the t-plot method with the Halsey equation. The slope of the t-plot was used to calculate the external SSA, while the micropore surface area (S_{micro}) was obtained from subtracting $S_{external}$ from S_{BET} . The mesoporous size distribution was obtained from Barrett-Joyner-Halenda (BJH) method from the adsorption branch with KJS correction. Finally, the presence of mesopores was tested using a JEOL JEM 2000EX transmission electron microscope (TEM).

2.2.5 Methods: Initial Iteration of CTNC-Fe Synthesis

As already mentioned, the synthesis process has been continuously updated to take into consideration data from all samples tested. Each catalyst sample completed was subject to either minor or major changes in process to continue to improve the electrochemical performance.

The baseline synthesis process first used was as follows:

1. BCP was stabilized at 280°C for 1 hour at a heating and cooling rate of 1°C/min under 150 mL/min standard air flow.
2. Stabilized BCP was then ground in an agate mortar and pestle for 20 mins.
3. 120 mg of stabilized BCP was mixed with 240 mg FeCl₂ in 10 mL ultra-pure water and stirred at 80°C until water was evaporated (approximately 2 hours).
4. The dried mixture was further dried in a vacuum oven at 60°C for 4 hours.
5. Mixture was then heat treated at 800°C for 1 hour at 10°C/min heat and cool rate under 150 mL/min N₂ flow.
6. Catalyst product was then ground in agate mortar and pestle for 30 minutes before making into electrode ink.

The method of synthesis of CTNC-Fe has continued to evolve as more electrochemical data is obtained from synthesis steps and processes that either hinder or enhance catalyst electrochemical activity. In the following three sections, several processes and the electrochemical results are presented that showed significant insight on the behavior of the CTNC-Fe.

2.3 The Effects of Iron Component Source and Concentration

2.3.1 Effects of Iron Component Source

As the CTNC obtained from PAN_{103-b}-PBA₆₀ is meant to act as the main source of carbon, nitrogen and formation of porosity and nanostructure, one of the first things to consider was to find an iron precursor that can produce FeN_x moieties when mixed with BCP without hindering the formation of nanostructure. There are many different iron precursors often used in the synthesis of Fe-N-C, however, two of the most often used in any type of catalyst involving a polymer and/or carbon base are iron chloride and iron sulfate.^{9-16,36,54-59}

For the synthesis of the catalyst, 150 mg of stabilized BCP were ground in a mortar and pestle and mixed in a 0.045 M solution of iron salt. Three different iron salts were tested: $\text{FeCl}_2 \cdot 4\text{H}_2\text{O}$, $\text{FeCl}_3 \cdot 6\text{H}_2\text{O}$ and $\text{FeSO}_4 \cdot 7\text{H}_2\text{O}$ and the iron percentage to stabilized BCP was 14.5 wt.%. The solution was stirred for 12 hours at room temperature then was heated to 80°C and stirred for approximately 3 hours till all water evaporated. The product was collected and dried in air at 60°C for 4 hours then heat treated at 900°C for 1 hour at 10°C/min heating and cooling rate under 150 mL/min N_2 flow rate. The resulting catalyst was then ground in agate mortar for 30 mins then acid leached in 5 mL 0.5 M H_2SO_4 solution for 8 hours at 80°C. Catalyst was then vacuum filtered and thoroughly washed with ultra-pure water, it was dried for 12 hours in air at 60°C then heat treated a second time at 900°C for 3 hours at 10°C/min heating and cooling rate in 150 mL/min N_2 flow rate.

As presented in Table 2.1 and Figure 2.2, it is clear to see that use of iron (II) sulfate as the iron source for the Fe-N-C catalyst is the better choice. Though the difference in the half-wave potential does not seem that pronounced, the differences in capacity surface area and mass activity are very large.

Table 2.1. Electrochemical activity results for tests on iron component source.

Iron Precursor	$E_{1/2}$ (V)	CSA (m^2/g)	A_{mass} (A/g)
FeCl₂	0.601	333.4	0.05
FeCl₃	0.638	460.1	0.18
FeSO₄	0.652	563.1	0.27

Although it has been noted that any sulfur containing precursor is likely to affect electrochemical activity by formation of graphitized sulfide species,⁵⁴ this can be overlooked due

to the presence of the $\text{Fe}^{2+/3+}$ redox peak in the FeSO_4 sample, which can be observed in Figure 2.2b. The iron peak is much more prevalent in the FeSO_4 sample than the other two, therefore, it is a clear conclusion that the greater amount of electrochemical activity can be attributed to the stable, reversible iron moieties.

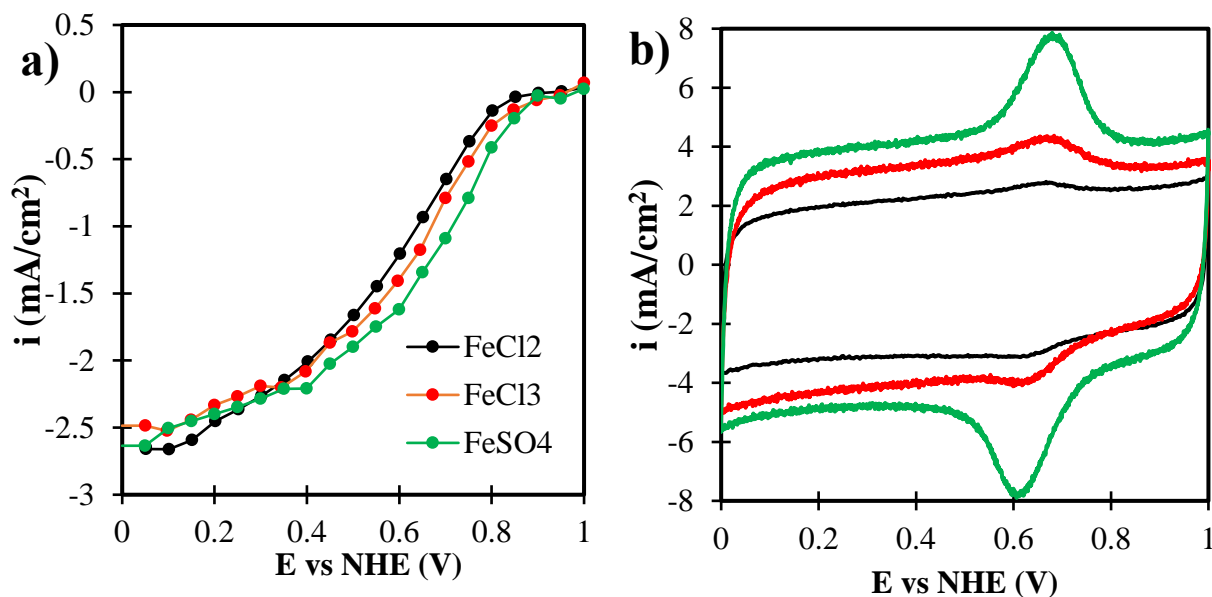


Figure 2.2. Electrochemical test results obtained from RDE potentiometry for catalysts with different iron sources a) Linear sweep voltammetry b) Cyclic voltammetry.

2.3.2 Effects of Iron Precursor Concentration

Five samples were prepared with stabilized BCP powder mixed in 0.01 M $\text{FeSO}_4 \cdot 7\text{H}_2\text{O}$ aqueous solution with 50%, 33.5%, 26%, 16.7% and 9.5% amounts of $\text{FeSO}_4 \cdot 7\text{H}_2\text{O}$ in overall solid mixture mass. Solutions were stirred for 12 hours at room temperatures then at 80 °C until most of the water was evaporated. Samples were dried in air at 60 °C for 2 hours, then pyrolyzed at 900 °C for one hour at 10°C heating and cooling rate in 150 mL/min N_2 flow. One sample of stabilized BCP was heat treated at the same conditions but left without any iron doping process. Results for the electrochemical activity tests can be seen in Table 2.2 and Figure 2.3.

Table 2.2. Electrochemical activity results for tests on effects of iron concentration with no post-processing.

Precursor mass (%)	E_{1/2} (V)	CSA (m²/g)	A_{mass} (A/g)
0	0.422	242.1	0.01
9.5	0.624	362.3	0.15
16.5	0.631	415.5	0.13
26	0.612	249.8	0.06
33.5	0.604	251.5	0.04
50	0.604	256.8	0.01

The addition of an iron precursor noticeably increases the electrochemical activity of CTNC in an acidic environment from 0.42 to 0.63V (Fig. 2.3a), on the other hand, cyclic voltammetry shows that there is a limit to how much iron precursor can be added before electrochemical activity drops (Fig. 2.3b). Although half-wave potential decreased only slightly from 0.63V at 9.5% to 0.61V at 16.5% precursor, CSA had a major change as it decreased from 415 to 250 m²/g. CSA appears to increase with the addition of the iron precursor during the iron doping step, although this change is offset by excessive addition of iron precursor. According to Zhong et al,⁴² Pristine CTNC usually shows a BET surface area of 500 m²/g whereas its capacitive surface area is 242 m²/g as seen in Table 2.1. The addition of an iron precursor, like iron (II) sulfate heptahydrate in this case, increases electrochemically accessible surface area of the nanocarbon as seen by the CSA values of the samples with iron content of 16.7 wt.% and lower. Furthermore, mass activity of the catalyst increases with addition of iron content, however, as shown by both E_{1/2} and CSA, the mass activity decreases the more iron is added.

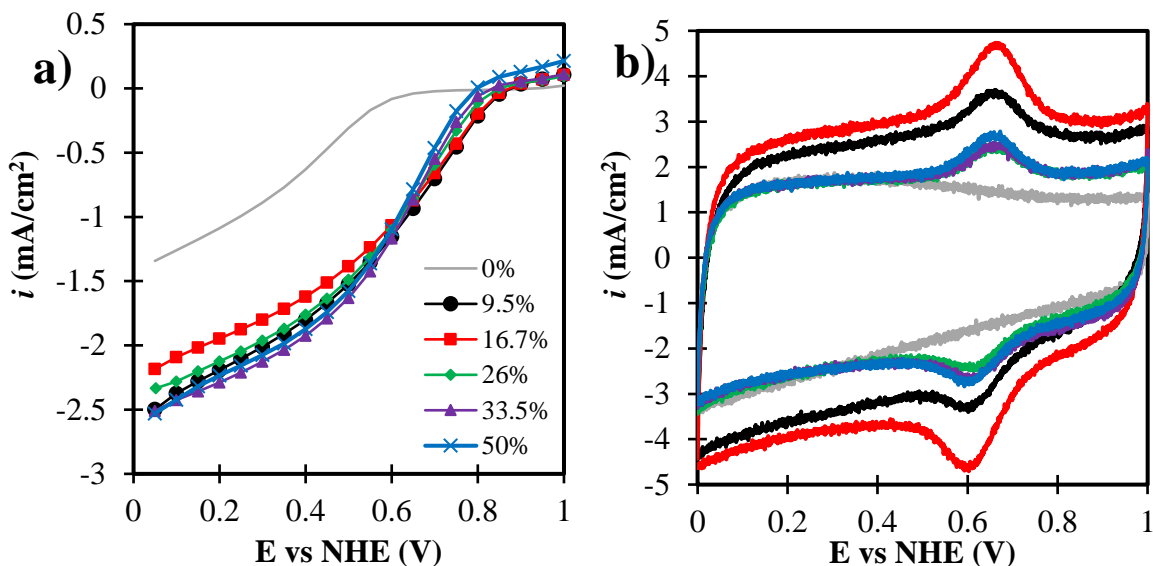


Figure 2.3. Electrochemical test results obtained from RDE potentiometry for catalysts with different iron concentrations and no post-treatment a) Linear sweep voltammetry b) Cyclic voltammetry.

2.4 The Effects of Heat Treatment Temperature

2.4.1 Effects of first Heat Treatment Temperature and Duration

The first heat treatment of the catalyst is meant to form the FeN_x moieties by generating porosity of the carbon from volatilization of the butyl acrylate and causing N heteroatoms to migrate to the carbon surface. However, excessive heat treatment can cause too much loss of nitrogen⁴⁴ through evaporation of the nitrogen moieties into nitrogen gas. However, not enough heat treatment of the catalyst, and the ohmic overpotential due to lack of electrical conductivity in the carbon can lead to low electrochemical activity. Therefore, the problem comes down to an optimization of heat treatment temperature and duration: enough time and energy for formation of active sites and graphitization but not enough to cause excessive volatilization of N heteroatoms.

Eight samples were prepared by mixing ball milled stabilized BCP into 0.01 M $\text{FeSO}_4 \cdot 7\text{H}_2\text{O}$ aqueous solution with mass concentration of 16.7 wt% iron precursor in overall solid mixture. Samples were stirred at room temperature for 12 hours, then heat stirred at 80°C for 2 hours until all water evaporated. Each sample was dried for 4 hours in air at 60°C then heat treated at temperatures of 600°C , 700°C , 800°C and 900°C for 1 hour at $10^\circ\text{C}/\text{min}$ heating rate in 50 mL/min N_2 flow. The remaining four samples were heat treated at 600°C for 0.5 hours, 2 hours, 3 hours and 4 hours with similar heating rate and N_2 flow. All samples were then ground in agate mortar and soaked in 0.5 M H_2SO_4 solution at 80°C for 2 hours. The catalysts were extracted using vacuum filtering and were washed thoroughly with ultra-pure water then they were all heat treated a second time at 900°C for 3 hours at $10^\circ\text{C}/\text{min}$ heating rate in 100 mL/min N_2 flow, this final heat treating step was performed in order to be able to test and directly compare the electrochemical activity of each sample, as those treated at lower temperatures are bound to suffer from extreme ohmic overpotential due to lower graphitization of the carbon base. The results from electrochemical tests can be seen in Figures 2.4 and 2.5 and in Tables 2.3 and 2.4.

Table 2.3. Electrochemical activity results for tests performed on catalyst samples heat treated at different temperatures.

Sample Temperatures ($^\circ\text{C}$)	$E_{1/2}$ (V)	CSA (m^2/g)	A_{mass} (A/g)
600	0.7372	643.6	0.46
700	0.73	680.7	0.35
800	0.729	644.3	0.35
900	0.7126	755.4	0.25

According to results, the initial heat treatment cannot be overdone, otherwise electrochemical activity decreases. Even though higher temperatures produce a greater CSA value, half-wave potential and mass activity both decreased the higher the temperature was increased.

Furthermore, even at the lowest temperature, too much heat treatment time slowly decreases electrochemical activity as shown by the half-wave potential but especially by the values of the mass activity since half-wave potential did not show much of a change between one and two hours of heat treatment at 600°C.

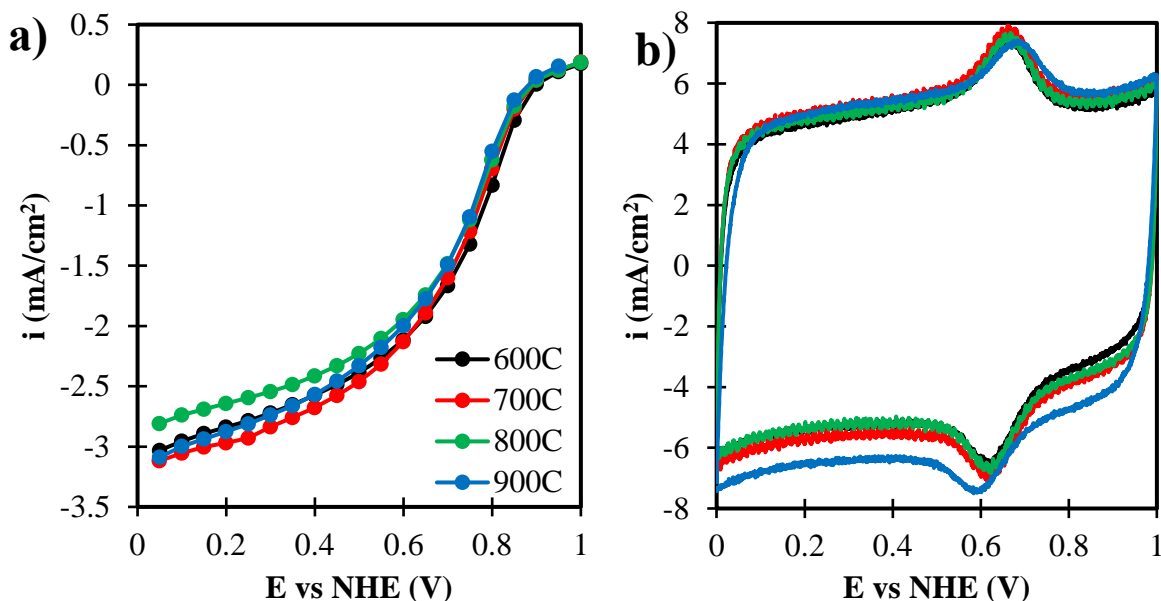


Figure 2.4. Electrochemical test results obtained from RDE potentiometry for catalysts with different temperature heat treatment a) Linear sweep voltammetry b) Cyclic voltammetry.

Table 2.4. Electrochemical activity results for tests performed on catalyst samples heat treated at 600°C with different duration.

Heat Treatment Duration (Hrs)	$E_{1/2}$ (V)	CSA (m^2/g)	A_{mass} (A/g)
0.5	0.7745	758.5	0.52
1	0.7372	643.6	0.46
2	0.7386	681.6	0.41
3	0.7227	656.4	0.36
4	0.6961	659.4	0.20

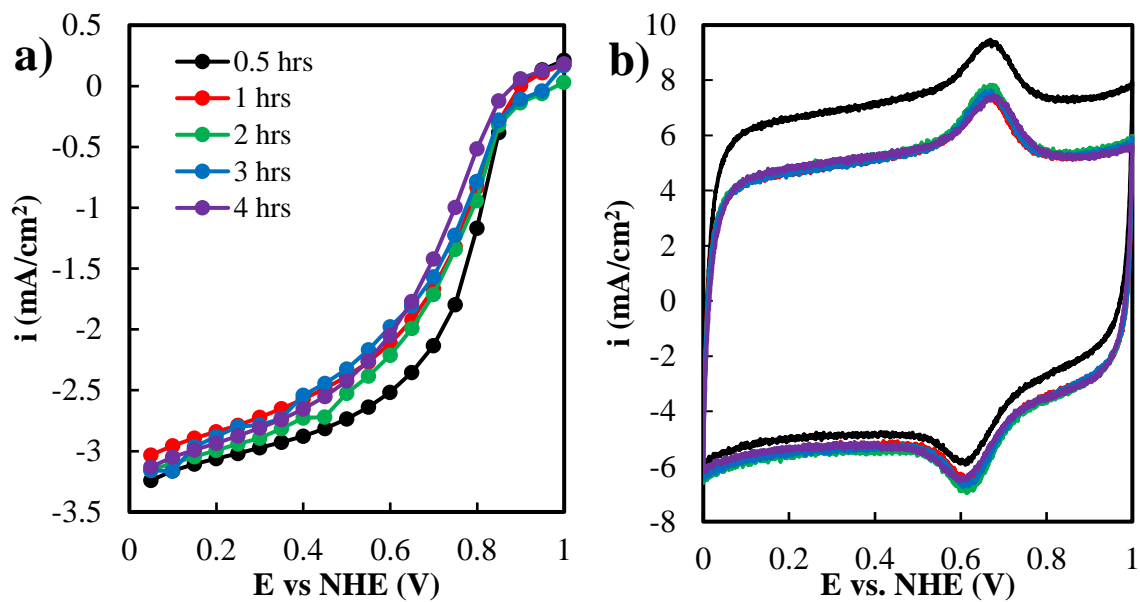


Figure 2.5. Electrochemical test results obtained from RDE potentiometry for catalysts heat treated at 600°C with different duration a) Linear sweep voltammetry b) Cyclic voltammetry.

2.4.2 Effects of Second Heat Treatment Temperature

To make sure that the catalyst sample reaches an acceptable level of graphitization, a second heat treatment is necessary. The higher the temperature, the higher the level of graphitization and the higher the electrical conductivity of the carbon base, however, higher heat treatment temperatures cause greater volatilization of heteroatoms from the carbon matrix.⁶⁰

Five samples were prepared by mixing ball milled stabilized BCP into 0.01 M FeSO₄·7H₂O aqueous solution with mass concentration of 16.7 wt% iron precursor in overall solid mixture. Samples were stirred at room temperature for 12 hours, then heat stirred at 80°C for 2 hours until all water evaporated. Each sample was dried for 4 hours in air at 60°C then heat treated at 900°C for 1 hour at 10°C/min heating rate in 150 mL/min N₂ flow. All samples were then ground in agate mortar and soaked in 0.5 M H₂SO₄ solution at 80°C for 2 hours. The catalysts were extracted using vacuum filtering and were washed thoroughly with ultra-pure water then they were all heat treated

a second time at 900°C for 3 hours, 900°C for 6 hours, 950°C for 3 hours and 1000°C for 3 hours respectively all at 10°C/min heating rate in 100 mL/min N₂ flow. One sample was left without a second heat treatment.

Table 2.5. Electrochemical activity results for tests performed on catalyst samples heat treated at 900°C with different second heat treatment protocols.

2nd Heat Treatment	E_{1/2} (V)	CSA (m²/g)	A_{mass} (A/g)
None	0.6204	414.6	0.04
900C, 6 hrs	0.7007	624.7	0.22
900, 3 hrs	0.693	546.7	0.18
950C, 3 hrs	0.692	321	0.19
1000C, 3 hrs	0.668	297.3	0.21

Results from electrochemical activity tests are shown in Figure 2.6 and Table 2.5. A significant increase in electrochemical activity is found as the half-wave potential increased noticeably after an acid soak and a second heat treatment (Fig. 9a). Furthermore, CSA increased by over 50% from 415 m²/g for sample with no 2nd heat treatment to 625 m²/g for the sample heat treated at 900°C for 6 hours. Since the sample with no heat treatment, which was only subjected to acid treatment after pyrolysis, has a CSA similar to the 16.7% sample from Figure 2.3, it can be concluded that acid treatment did little to increase surface area, at least in absence of a second heat treatment. However, the increase in higher temperatures resulted in lower CSA and half-wave potential. This could be due to an increase in volatilization of heteroatoms from the carbon matrix at higher temperatures where the formation from amorphous to graphitic carbon is more prevalent.⁶¹ As opposed to the 1st heat treatment, the mass activity did little to reveal any pattern in heat treatment, furthermore, it is CSA which is most affected by higher temperatures after acid

soaking of the samples. Therefore, it is likely that higher temperatures under these conditions have a greater impact on the nanostructure of the catalyst itself as the mass activity difference between the 900°C and 1000°C samples is minimal. So, it can be concluded that under these conditions, a second heat treatment is likely to negatively affect the mesoporous surface and therefore decrease the half-wave potential of the CTNC-Fe catalyst.

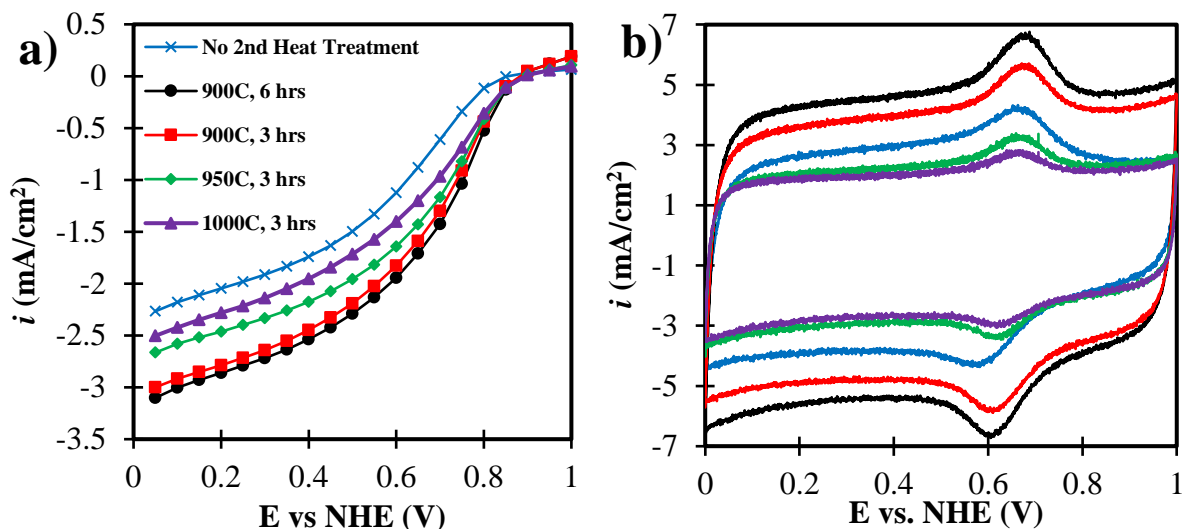


Figure 2.6. Electrochemical test results obtained from RDE potentiometry for catalysts heat treated at 900°C with different 2nd heat treatment protocols a) Linear sweep voltammetry b) Cyclic voltammetry.

2.5 The Effects of Gas Flow Conditions During Heat Treatment

There is a level of variability in results of samples synthesized in different furnaces. After testing the temperatures of the furnaces using a K-type thermocouple, the variation in temperature amongst different furnaces was found minimal if at all. What varied significantly, however, was the diameter of the tube used. This may seem insignificant, unless we calculate the variation in flow velocity using Eq. 9.

$$Q = VA \quad (9)$$

Where Q stands for flow rate (mL/min), V is flow velocity (cm/sec) and A is cross-sectional area of tube furnace (cm²). Calculations for flow velocities found a difference of 16.5 cm/sec between the two furnaces being used. Other instances related to this issue become evident when testing samples heat treated in the same furnace at the same time. Multiple crucibles interrupt the flow inside the tube furnace, and it is likely that volatile products could affect the reactions of down-stream samples as well. These instances led to unpredictable and sometimes erratic results in electrochemical activity and caused a great deal of setbacks in the progress of optimization of CTNC-Fe.

Six samples were prepared by mixing ball milled stabilized BCP into 0.01 M FeSO₄·7H₂O aqueous solution with mass concentration of 16.7 wt.% iron precursor in overall solid mixture. Samples were stirred at room temperature for 12 hours, then heat stirred at 80°C for 2 hours until all water evaporated. Each sample was dried for 4 hours in air at 60°C then heat treated at 900°C for 1 hour at 10°C/min heating rate in N₂ flow rates of 150, 100 and 50 mL/min. The remaining three samples were heat treated at 900°C for 1 hour at 10C/min heating rate in 50 mL/min N₂ flow rate then they were ground in agate mortar and soaked in 0.5 M H₂SO₄ solution at 80°C for 2 hours. The catalysts were extracted using vacuum filtering and were washed thoroughly with ultra-pure water then they were all heat treated a second time at 900°C for 3 hours at 10°C/min heating rate in 150, 100 and 50 mL/min N₂ flow rates. The results of the electrochemical activity tests can be seen in Figure 2.7 and Table 2.6 which also includes mass yield for all catalysts after their last heat treatment.

Table 2.6. Electrochemical activity results for tests performed on catalyst samples heat treated with different N₂ flow rates.

Flow Rate (mL/min)	E _{1/2} (V)	CSA (m ² /g)	A _{mass} (A/g)	Mass Yield (%)
50	0.685	680.9	0.13	44.1
100	0.685	531.5	0.18	46.3
150	0.665	464.7	0.12	45.8
50, 50	0.664	554.6	0.12	58.7
50, 100	0.713	755.4	0.25	68.8
50, 150	0.702	471.3	0.2	75.5

Lower flows during the first heat treatment resulted in higher electrochemical activity (Figs. 2.7a-b) which show an increase from 0.64 to 0.68V and a significantly higher CSA which more than doubled by a decrease of 100 mL/min in nitrogen flow rate as shown by the 150 mL/min and 50 mL/min samples. However, the carbon yield (Table 2.6) shows that this is not due to carbon oxidation since the yields are similar for all nitrogen flows. Therefore, increase in CSA and half-wave potential could be due to greater graphitization caused by the change in nitrogen gas concentration and convection effects during pyrolysis resulting from the reduction in nitrogen gas flow rate. In addition, results for the 50, 50 mL/min to 50, 150 mL/min samples, can be linked to carbon oxidation during the second heat treatment since the carbon yield varied from 75.5% for 150 mL/flow rate during heat treatment to 58.7% for 50 mL/min. This caused an increase in half-wave potential from 0.68 to 0.72V, and in CSA from 681 to 755 m²/g which were the highest values obtained using CTNC as a catalyst base here. Although, the longer time during the second heat treatment provides more time for carbon oxidation which also affects ORR of catalyst, it is still unclear why the nitrogen flow variation significantly affects ORR activity during the first heat treatment since carbon oxidation is not apparently present during that step of catalyst treatment.

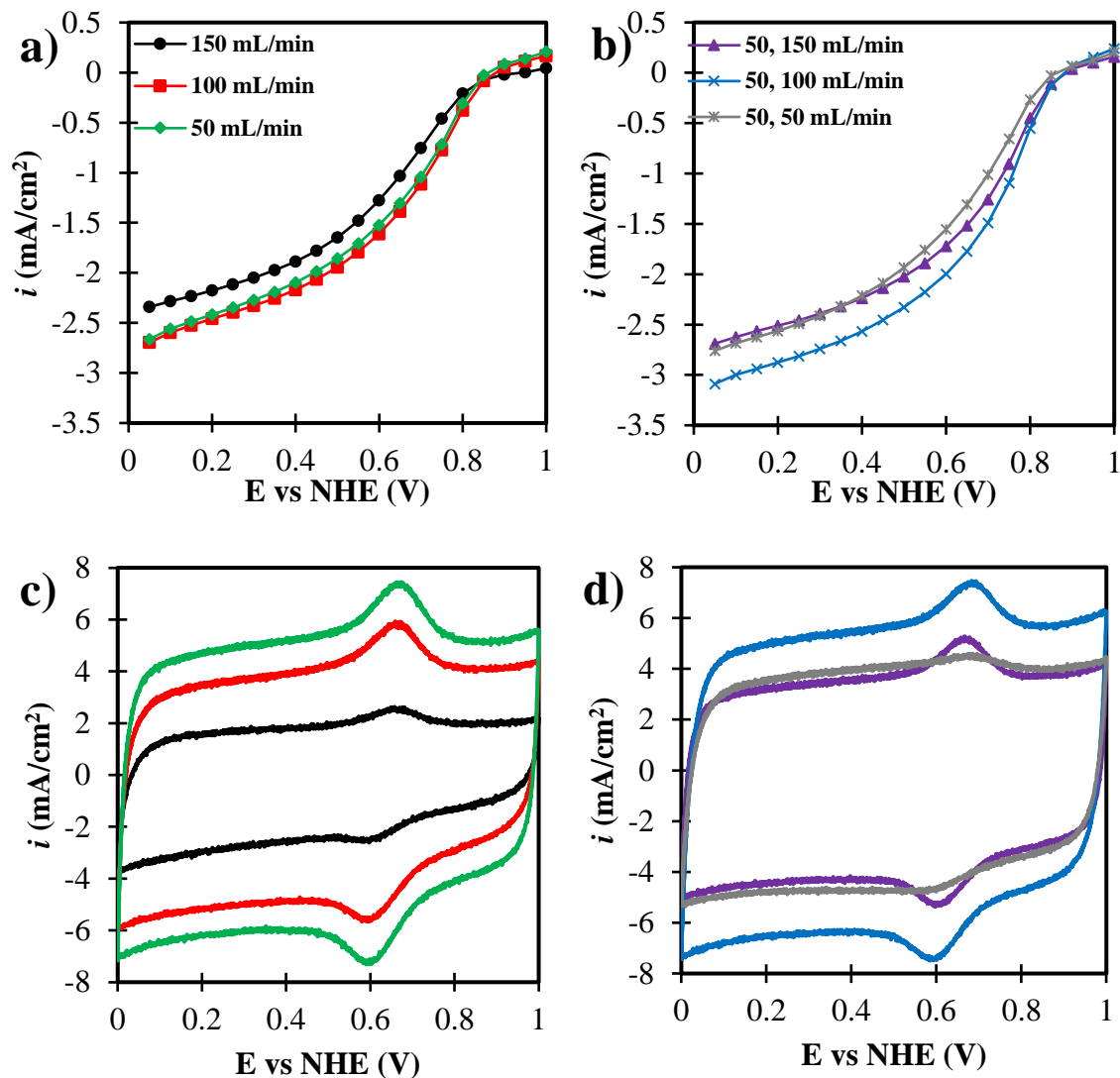


Figure 2.7. Electrochemical test results obtained from RDE potentiometry for catalysts heat treated at 900°C with different N₂ flow rates a)-b) Linear sweep voltammetry c)-d) Cyclic voltammetry.

It can be concluded that the nitrogen concentration varied by flow rate as well as convection affect the rate of graphitization as well as the concentration of nitrogen heteroatoms in the carbon matrix. Furthermore, this suggests that a key to optimizing the formation of active sites from the rich nitrogen content in CTNC-Fe lies on the manipulation of nitrogen atom migration from the carbon matrix bulk to the pore surface while avoiding too much volatilization. This is vastly

different to other methods of synthesis that require a nitrogen precursor to mix in with a carbon surface since in that case the nitrogen is being controlled to coalesce into the carbon surface.⁸⁻¹⁶

2.6 The Effects of Fe-doping before and after Carbonization of CTNC

Because the Fe-doping step had been done before carbonization of the CTNC, there was a possibility that this could be hindering the formation of the nanostructure and therefore decreasing the possible amount of surface area generated by CTNC. To test this, two samples were synthesized: one done with the Fe-doping step before the first heat treatment and therefore before carbonization of the CTNC and formation of its mesoporous structure, and the other was done with Fe-doping after the first heat treatment and/or carbonization of the CTNC.

One sample was prepared by mixing 90.0 mg of ball milled stabilized BCP into 0.01 M $\text{FeSO}_4 \cdot 7\text{H}_2\text{O}$ aqueous solution with mass concentration of 16.7 wt.% iron precursor in overall solid mixture. The second sample was prepared by mixing carbonized CTNC prepared from ball milled stabilized BCP at 600 °C for 30 mins. The known 32% yield of CTNC from BCP was used to calculate equivalent iron content to that of the first sample. Samples were stirred at room temperature for 12 hours, then heat stirred at 80°C for 2 hours until all water evaporated. Each sample was dried for 4 hours in air at 60°C then heat treated at 600°C for 30 mins at 10°C/min heating rate in N_2 flow rate of 50 mL/min. Both samples were acid treated for 2 hours at 80°C and vacuum filtered and washed then dried for 4 hours in air at 60°C. They were then heat treated at 900 °C for 3 hours at 10 °C/min in 100 mL/min N_2 flow rate.

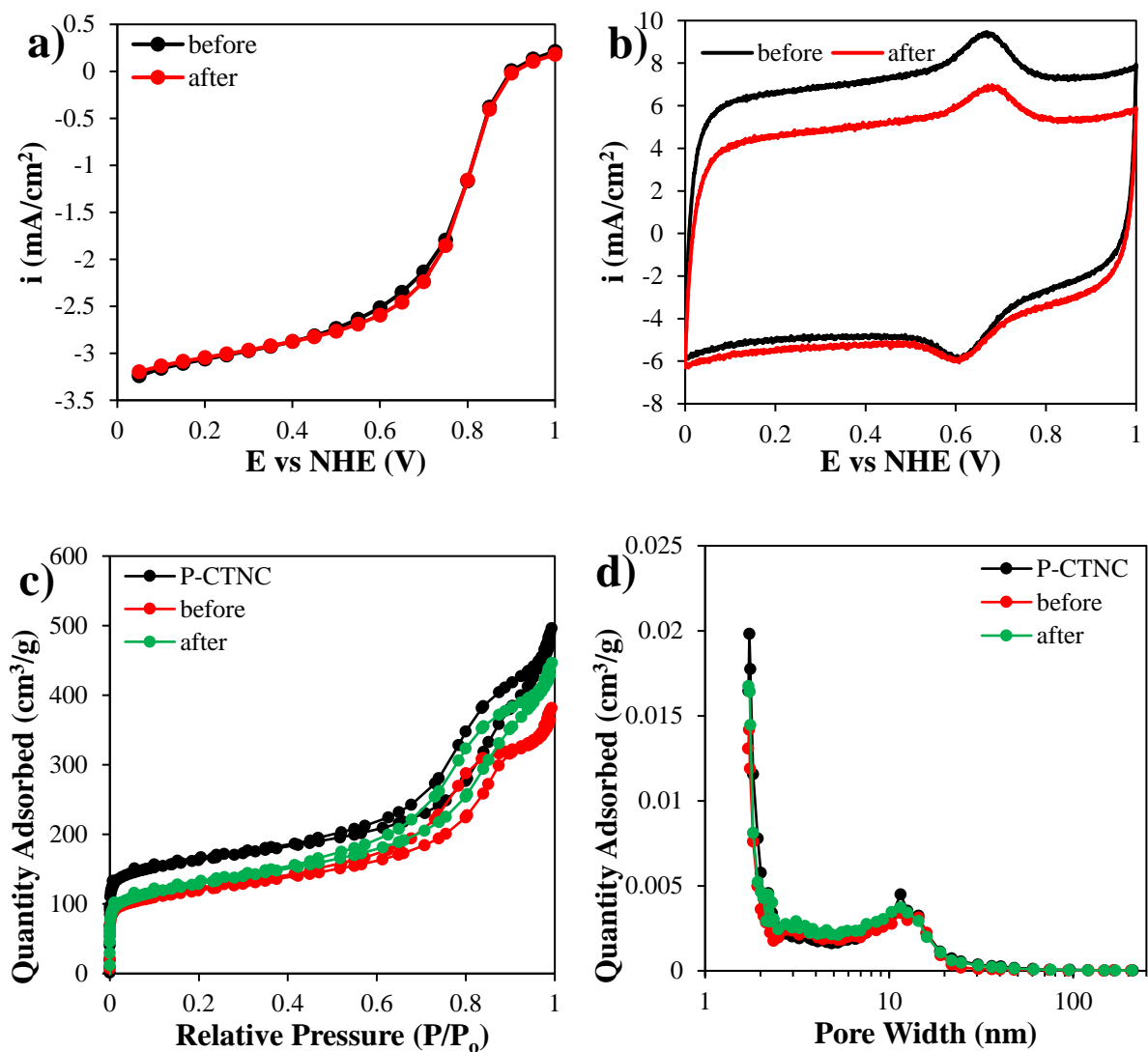


Figure 2.8. RDE potentiometry and BET surface area results for samples of Fe-doping before and after carbonization. a) Linear sweep voltammetry curve obtained at room temp under oxygen flow at 900 rpm, b) Cyclic voltammetry curve obtained at room temp with nitrogen flow and 200 rpm, c) adsorption-desorption isotherms at $-196\text{ }^{\circ}\text{C}$, and d) Pore width distribution.

The electrochemical activity results are shown in Fig. 2.8a-b, the half-wave potential average values for before and after Fe-doping process were 0.7745 V and 0.7767 V respectively. Mass activity also showed similar values of 0.536 A/g for the before-carbonization process and 0.565 A/g for the after-carbonization process.

Similarly, CSA showed a significant difference of 758.5 m²/g for the before-carbonization Fe-doping and 638.1 m²/g for the after-carbonization Fe-doping. BET surface area analysis, on the other hand, produced a higher surface area value for the after-carbonization Fe-doping sample as seen in Table 2.7.

Table 2.7. Summary of BET surface area analysis results for CTNC-Fe samples synthesized with Fe-doping step performed before and after carbonization of CTNC. The P-CTNC sample refers to pristine CTNC without any Fe-doping or any other process done to the CTNC-Fe samples other than similar heat treatment.

Fe-Doping	BET Surface Area (m ² /g)	Micropore (m ² /g)	Mesopore (m ² /g)	Average Pore size (nm)
P-CTNC	528.6	276.4	252.1	8.7
before	395.8	164.69	231.1	8.1
after	430.4	157.7	272.7	8.3

It was when comparing the Fe content of the catalyst samples that the difference becomes more apparent. According to EDS, the before-carbonization sample retains a value of 12.04 wt% Fe and according to TGA the after-carbonization sample has a content of 4.612 wt% Fe. Using this value to calculate iron mass activity produces 4.45 A/g for before-carbonization and 12.25 A/g for after carbonization. This means that the after-carbonization sample's iron content is almost three times more active than that of the before-carbonization catalyst sample. In addition, the mesopore value of the after-carbonization sample is even higher than that of pristine CTNC. It is likely that Fe-doping after carbonization is retaining the structure of the CTNC a little better than the sample with Fe-doping before carbonization. Therefore, it can be concluded that the better method of CTNC-Fe synthesis is the one with Fe-doping after first carbonization. This means that the process requires an extra heat treatment step for a technicality in electrochemical activity and it makes the catalyst synthesis process more costly, however, this single step could prove to be the

key to improving the catalyst performance when testing different CTNCs produced by variation of the BCP composition.

2.7 Summary on the Optimization of CTNC-Fe

2.7.1 Summary of Results

Although there have been some setbacks, the quality of CTNC-Fe catalysts has continued to improve slowly. From an average of 0.62 V for the half-wave potential, we have reached a maximum of 0.781 V vs NHE for the use of PAN₁₀₃-*b*-PBA₆₀ when dealing only with methods of Fe-doping, acid treatment, heat treatment and other methods of handling the CTNC to generate an Fe-N-C catalyst. Although the use of other BCPs has been brief, we have been able to reach a half-wave potential of 0.8 V vs NHE with the best synthesis methods developed.

Capacitive surface area has shown a greater deal of variation, but it too has improved significantly over the last three years as it has more than doubled when compared to that of the earliest experiments. As shown in Figure 2.9, there has been an overall trend of improvement with successive number of experiments done on a mostly one single type of BCP, namely PAN₁₀₃-*b*-PBA₆₀. Table 2.8 shows a summary of the progress on optimization including the standard deviation for all samples. The most recent samples, which were synthesized by successfully combining the best protocols from some of all the optimization experiments that have been performed, are all clustered closest to the maximum data value achieved. This may be outside the one standard deviation value for the data set, however, enough RDE potentiometry tests have been performed to ensure that results are statistically significant and not subject to errors.

Table 2.8. Summary of results for synthesis optimization experiments of CTNC-Fe.

Electrochemical Activity Qualifier	Minimum	Maximum	Median	Average	Standard Deviation
$E_{1/2}$ (V vs NHE)	0.364	0.800	0.666	0.657	0.0831
CSA (m^2/g)	69.991	798.98	406.02	437.37	0.08

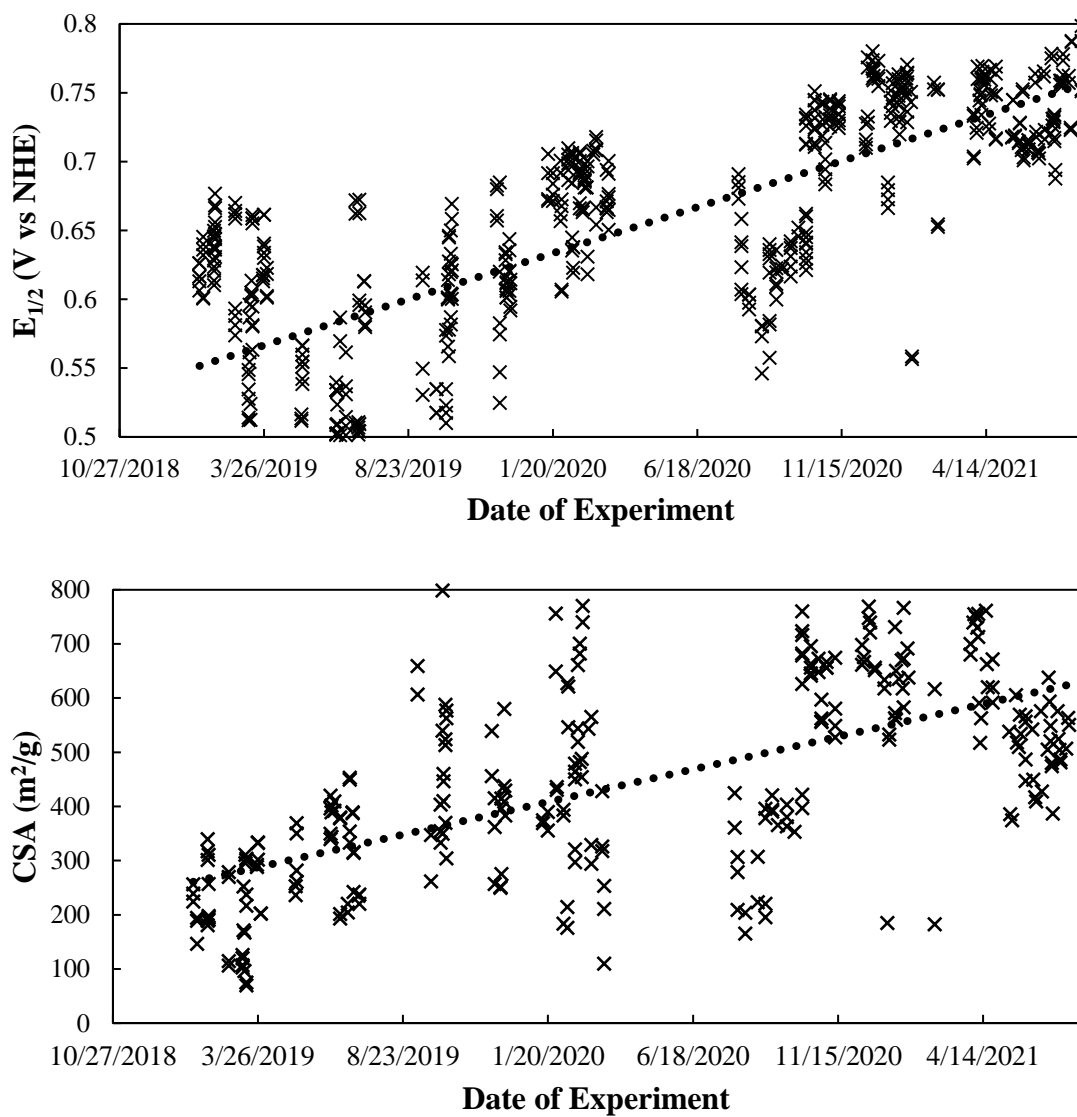


Figure 2.9. Summary of results for all optimization experiments a) Half-wave potential b) Capacitive surface area.

2.7.2 Comparison of Pristine CTNC and CTNC-Fe catalyst

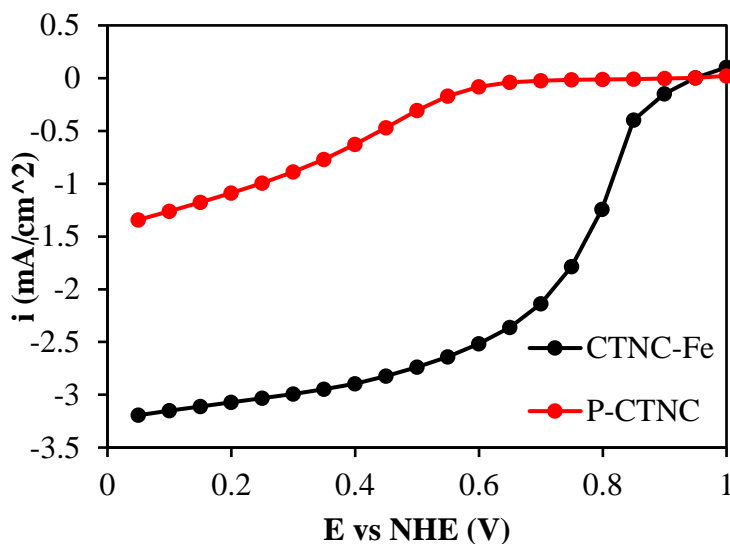


Figure 2.10. ORR electrochemical activity curves of CTNC-Fe (Fe-N-C) vs. P-CTNC in 0.5 M H₂SO₄ solution under oxygen flow at room temperature obtained using chronoamperometry scans at 900 rpm.

Additionally, we have performed tests that compare the ORR electrochemical activity of CTNC-Fe versus that of pristine CTNC (P-CTNC) in an acidic environment to ensure that the improvements in electrochemical activity are a product of proper incorporation of FeN_x moieties in the carbon. Figure 2.10 shows the results of one of the best CTNC-Fe samples obtained vs. that of P-CTNC, both samples were obtained from PAN₁₀₃-*b*-PBA₆₀ copolymer. The half-wave potential of P-CTNC is 0.42 V vs NHE while the half-wave potential of the CTNC-Fe sample is 0.78 V vs NHE. As can be seen, the presence of N moieties contributes to the ORR activity despite the lack of Fe in the pristine sample. However, this activity is very minor compared to that which is achieved through Fe-doped CTNC. There is little doubt though that any N presence in the catalyst, whether bonded to Fe ions (FeN_x) or not, still has a significant if not substantial effect on ORR.

2.7.3 Latest Iteration of CTNC-Fe Synthesis Process Using Fe Salts

Although it is all but inevitable that this method of synthesis will continue to improve with more experiments this is the latest method of synthesis used which produces the best performance in CTNC-Fe catalyst.

1. BCP is dissolved in 20 wt% NMP solution, then the solution is precipitated using ultra-pure water.
2. The precipitated copolymer is vacuum filtered and thoroughly washed with ultra-pure water.
3. The BCP is dried in air at 60 °C for 12 hours.
4. The BCP powder is stabilized at 280 °C in 150 mL/min air flow for 1 hour using 1 °C/min heating rate.
5. The stabilized BCP is ball-milled for 90 minutes using 7.3 mm diameter polymethylmethacrylate balls per 100 mg of material.
6. The ball milled material is heat treated at 600 °C for 30 mins in 50 mL/min N₂ flow using 10 °C/min.
7. 58.7 mg of ball milled stabilized BCP is added into 5 mL of 0.01 M FeSO₄·7H₂O aqueous solution (58.7 mg of stabilized BCP per 18.0 mg of FeSO₄·7H₂O) and stirred for 12 hours at room temperature.
8. The temperature of the hot plate is raised to 80 °C and the solution is stirred till water has evaporated completely.
9. The product is dried at 60 °C in air for 4 hours.
10. The product is heat treated at 600 °C for 30 mins under 50 mL/min N₂ flow using 10 °C/min heating rate.

11. The catalyst is soaked in 0.5 M H₂SO₄ water solution at 80 °C for 2 hours then it's vacuum filtered and washed thoroughly with ultra-pure water.
12. The product is dried for 4 hours in air at 60 °C.
13. The catalyst is heat treated at 900 °C for 3 hours in 100 mL/min using 10 °C/min heat rate.
14. The catalyst is ground in agate mortar before using to reduce the presence of macro-agglomerations.

Chapter 3: Materials Characterization and Fuel Cell Testing of CTNC-Fe Catalyst

3.1 Abstract

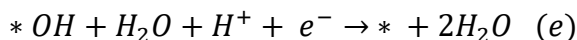
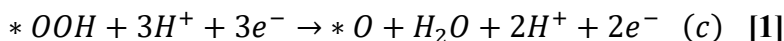
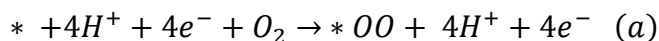
Platinum Group Metal free (PGM-free) catalysts present a promising opportunity to make hydrogen fuel cells more affordable, however, issues with stability and electrochemical activity continue to hinder their application. Recent studies point to the availability of nitrogen and a controlled mesoporous structure as avenues of improvement. To address this need, copolymer templated nitrogen-enriched carbon (CTNC) was used as the precursor to prepare PGM-free catalysts for oxygen reduction reaction (ORR). By employing its rich nitrogen content and interconnected mesoporous structure, a significant amount of Fe-N-C active sites were formed by co-annealing CTNC with FeSO₄. The formed N/Fe co-doped nanocarbon (CTNC-Fe) catalyst exhibits good electrochemical activity with a half-wave potential of 0.781 V vs NHE, a total surface area of 400 m²/g and a power density of 180 mW/cm². The block copolymer (BCP) was made by atom transfer radical polymerization (ATRP) which allows control and tunability of the block copolymer. This work opens new opportunities to improve the electrochemical activity and stability of PGM-Free catalyst by controlled polymerization techniques that precisely tune the pore structure and maximize nitrogen content to improve formation of active sites in the catalyst.

3.2 Introduction

In the search for sustainable and clean energy sources, proton exchange membrane fuel cells (PEMFCs) have become one of the most promising alternatives. The oxygen reduction reaction (ORR) and hydrogen evolution reaction (HER) make it possible to surpass the Carnot efficiency limit of heat engines. Furthermore, hydrogen is a sustainable and non-polluting energy resource with a specific energy density (143 MJ/kg) that is three times that of hydrocarbon fuels such as natural gas (53.6 MJ/kg) and gasoline (46.4 MJ/kg) and can be used in both mobile and stationary power generation.^{4,5} However, one major drawback to PEMFCs is the sluggish kinetics of ORR which require the use of noble metals such as platinum.⁵ This limits their large-scale application as the cost of the catalyst is approximately 41% compared to the rest of the fuel cell pack.⁷

To address these issues, the development of platinum group metal-free (PGM-free) catalysts has been a subject of intense research over the past decade.⁸⁻¹⁶ These catalysts, also referred as transition-metal-nitrogen-carbon catalysts (M-N-C), are synthesized with inexpensive, abundant precursors and show excellent compatibility with PEMFCs.^{8,11,15} They are usually made from a mixture of transition metal salts and organic nitrogen-rich compounds which when heat treated at temperatures in the range of 600-1100 °C result in a graphitic carbons with high porosity and surface area.¹⁵ The catalyst relies on heteroatom moieties in the graphitic surface composed of mainly nitrogen and transition metal atoms as the catalytic active sites.⁸⁻¹⁶ Moreover, it is generally agreed that atomically dispersed iron coordinated by nitrogen ligands is the most electrochemically active moiety in the catalyst as it is capable of a full $4e^-$ reduction from oxygen to water in acidic conditions.¹⁷⁻¹⁹ However, some studies suggest the presence of a persistent hydroxide radical ligand on the MN_4 active site as a significant factor in increasing electrochemical

activity of the active site, except when the metal ion is Co.⁶¹ The reaction pathway, Eq. 1, has been tentatively agreed on as the ORR for MN₄ active sites (where * is the active site), density functional theory calculations point to the fourth step being the potential determining step in the case of Fe as the metal component, however, this is a continued topic of debate in the research community.⁶¹



M-N-C catalysts were first reported in 1964, when metal containing macrocyclic molecules such as porphyrin were first tested as catalysts for ORR.²¹ Additionally, this type of ORR catalysis has similarities to biochemical processes such as hemoglobin oxygen binding and cellular respiration performed by cytochrome c oxidase, thereby prompting some researchers to follow a biomimetic approach to develop new catalysts.^{22,62,63} However, synthesizing a catalyst that achieves the same ORR activity of platinum catalysts has remained a great challenge, from both the electrochemical activity perspective and their stability.¹¹ Many methods of synthesis have been developed recently including, varying the source of carbon, nitrogen and transition metal to continuously improve the catalyst performance.⁸⁻¹⁶ There are three major types of processes that have been developed: 1) pyrolysis of metal organic frameworks (MOFs), 2) nitrogen and iron doping of high surface area carbon templates using transition metal salts and nitrogen rich gases, solutions and/or polymers and 3) mixture of nitrogen, carbon and metal precursors with a volatilizing agent which generates porous nitrogen and iron co-doped carbon structures after being heat treated.⁸⁻¹⁶ However, one issue is in their inability to reliably control the porous structure.⁸⁻¹⁶

In the case of MOFs and precursor mixtures, the porous structures are generated by evaporation of zinc chloride, cyanamide and other volatile agents.^{8,15} On the other hand, use of hard templates can generate a controlled structure in carbon⁶⁴, however, iron doping and the addition of salts tend to change the nanostructure of carbon, which makes it difficult to control the final structure of the catalyst¹⁵. The lack of control over pore size can be an impediment for forming a high density of active sites, as their formation is greatly influenced by the size and structure of the pores.⁴⁴⁻⁴⁷

To overcome this issue, block copolymers were used as templates for the synthesis of nanocarbons.²⁶⁻⁶⁸ In the case of A-B diblock copolymers, the thermodynamic incompatibility between blocks A and B drives A-B diblocks to self-organize via microphase separation to generate different morphologies. Additionally, self-assembly of BCPs is low-cost, fast, and easily scalable along with modern synthetic chemistry enabling the tailoring of the structure and hence the properties of individual blocks and the assembly.⁶⁹ To account for this, we employed a copolymer templated nitrogen-rich nanocarbon (CTNC) as a base for a PGM-free catalyst which was previously used as electrochemically active heteroatom enriched mesoporous carbons.⁷⁰⁻⁷⁶ The polymer precursor, poly(acrylonitrile)-*b*-poly(*n*-butyl-acrylate) (PAN-*b*-PBA), was synthesized by copolymerization of acrylonitrile (AN) and *n*-butyl acrylate (BA) using atom transfer radical polymerization (ATRP).⁷⁷⁻⁷⁹ PAN acts as both nitrogen and carbon precursor and PBA is the sacrificial component that generates porosity after pyrolysis at temperatures above 600 °C.⁸⁰ The well-defined nanostructure is generated by self-assembly driven by phase separation of the two immiscible polymer blocks,^{66,69} which is then fixed by using the oxidative stabilization of PAN, as is implemented in carbon fiber manufacturing.^{71,81} Among various self-assembled morphologies, of particular interest to this work are bicontinuous gyroid-like morphologies,^{69,70} which assure the overall pore connectivity and accessibility required for an improved

electrochemical performance. This is a potentially new advantageous approach to improving the electrochemical activity of PGM-free catalysts by “soft templates” rather than relying only on surface activation by compounds such as ZnCl_2 and KOH .⁸²⁻⁸⁴ ZIF/MOFs derived PGM-free catalysts, on the other hand, though highly electrochemically active and made with a method that allows excellent control over particle size, have a narrow pore size range compared to CTNC as proven by efforts to tailor their morphology through use of nanofibers and silica templates.⁸

The method using CTNC is unlike other previously tested methods of reactive polymerizations, where monomers such as phenylenediamine, aniline, pyrrole, 3-methylthiophene, etc. are polymerized in a mixture of carbon black or nanotubes.^{26,36,37,54-59,85-88} Although the presence of a volatile sacrificial component (PBA in this case) is similar to reports using a reactive polymerization process.⁸⁹⁻⁹¹ Our work is more reminiscent of synthesis methods with no added carbon sources other than the nitrogen precursors.

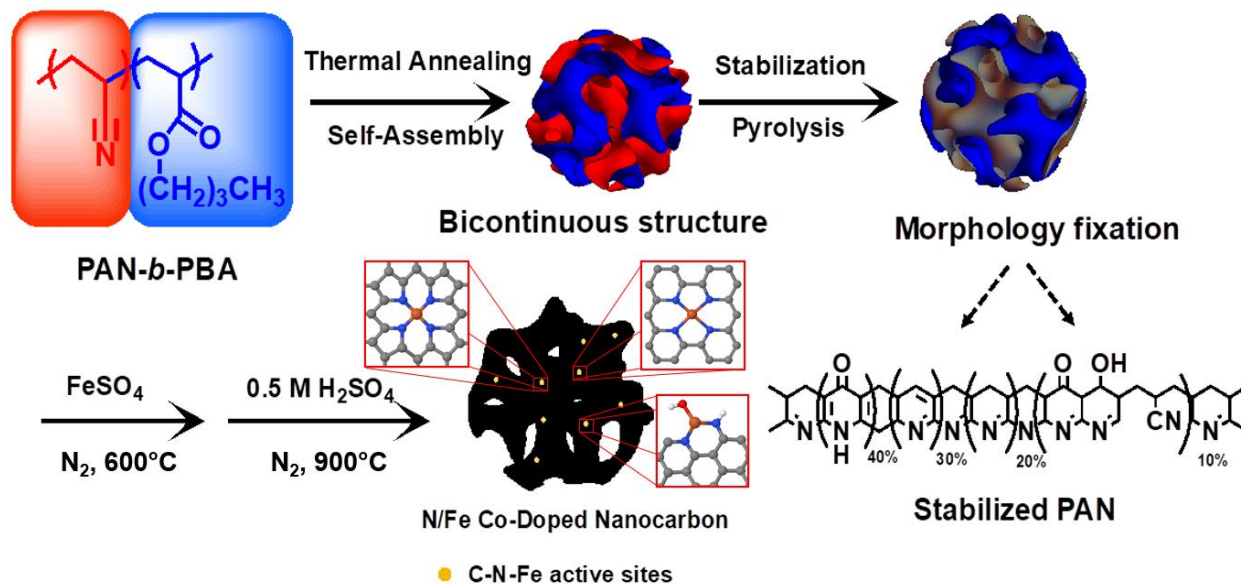


Figure 3.1. Preparation of CTNC-Fe from PAN-*b*-PBA copolymer

Fig. 3.1 illustrates the process of preparing CTNC-Fe, an Fe-N-C catalyst using the BCP-derived carbon as a base. In addition, the nitrogen content of CTNC measured in previous work

has been found to reach a maximum of 17 at. % at lower heat treatment temperatures of 600 °C,^{71,73} determined by measurements using X-ray photoelectron spectroscopy (XPS). This rich nitrogen content could prove very beneficial in formation of Fe-N_x active sites in the presence of an iron precursor.

In this work, we utilized CTNC with a unique bicontinuous morphology as a precursor to produce N/Fe co-doped nanocarbons (CTNC-Fe) for PGM-free fuel cells. For the carbon to retain the mesoporous structure, the metal doping process was performed after thermal stabilization in air. Iron (II) sulfate was used as the metal component since iron has been previously found to be the most electrochemically active transition metal in this type of catalyst and sulfate salts have been used as a precursor for Fe-N-C catalysts in several reports.^{47,54,91} The goal of this work is to determine whether CTNC could be applied to make a working Fe-N-C catalyst that retains its nanostructure. The proof-of-concept was supported by testing in a fuel cell assembly with hydrogen and oxygen flow at low temperature fuel cell conditions. The morphology and elemental composition of the catalyst were also analyzed by different characterization methods.

3.3 Experimental Section

3.3.1 Materials

Azobisisobutyronitrile (AIBN), dimethylsulfoxide (DMSO), dimethylformamide (DMF) CuBr₂, tris(2-pyridylmethyl)amine (TPMA), acrylonitrile (AN), bipyridine nitrate (BPN), n-butyl acrylate (BA), HCl, methanol, ultrapure water, FeSO₄·7H₂O, 0.5 M sulfuric acid aqueous solution, Nafion 5 wt% solution and ultra-pure water were used. All materials were obtained from Millipore Sigma. CuBr₂ was purified by stirring in glacial acetic acid followed by washing with ether and dried overnight under vacuum. Monomers were passed through a basic alumina column prior to use.

3.3.2 Preparation of PAN-*b*-PBA copolymers

PAN₁₀₃ was synthesized by initiator for continuous activator regeneration (ICAR) ATRP using a previously reported technique.⁵⁰ In a typical procedure, 17 mg of AIBN (0.1 mmol, 0.1 equiv.), 30 mL of DMSO and 3 mL of DMF were charged into a Schlenk flask and degassed with N₂ for 30 min. A stock solution of CuBr₂ and 3 mL of DMF was prepared and degassed for 10 min, then 9 mg (0.04 mmol, 0.04 equiv.) of CuBr₂, 36 mg (0.12 mmol, 0.12 equiv.) of TPMA were added to the Schlenk flask. 27 mL (415 mmol, 400 equiv.) of degassed AN was added to the above flask, and finally 139 mg (1.0 mmol, 1 equiv.) of BPN was added and the polymerization was started by immersing the flask in an oil bath at 65 °C and conducted for 5 h to reach 26% conversion. The final polymer was isolated by precipitation resulting from addition of the reaction mixture to methanol/water (4:1, v/v), and dried under vacuum at room temperature overnight.

PAN₁₀₃-*b*-PBA₆₀ block copolymer (BCP) was synthesized by supplemental activator and reducing agent atom transfer radical polymerization (SARA ATRP) developed previously.^{70,71} Using this approach, 5 g (0.9 mmol, 1 equiv.) of PAN-Br macroinitiator (M_n, NMR = 5600) was dissolved in 50 mL of DMF. The solution was then added to a 100 mL Schlenk flask containing 1.5 mg of CuBr₂ (0.0067 mmol, 0.0075 equiv.) and 5.8 mg of TPMA (0.02 mmol, 0.0225 equiv.) and bubbled with nitrogen for 20 min. 19 mL of deoxygenated BA (134 mmol, 150 equiv.) was then carefully added under vigorous stirring to prevent PAN precipitation. Cu wire (8 cm length x 1 mm diameter), previously cleaned with HCl: MeOH solution (1:1, v/v) was added to start polymerization at room temperature. The reaction was stopped after 4.2 h with conversion reaching 40%. The resulting block copolymer was precipitated by adding the reaction solution to methanol/water (6:4, v/v), then it was filtered and dried under vacuum overnight.

3.3.3 Preparation of CTNC-Fe Catalyst

PAN₁₀₃-*b*-PBA₆₀ BCP was stabilized in air at 280 °C for one hour then it was ball-milled for 90 min. 90 mg of ball-milled stabilized BCP was mixed in 5 mL of ultra-pure water with 18.0 mg of FeSO₄·7H₂O and was stirred for 12 hours. The solution was then heated to 80 °C and stirred for an additional 2 hours until water fully evaporated. The dry mixture was further dried for 4 hours in air at 60 °C and then it was heat treated at 600°C for 0.5 hours in 50 mL/min N₂ flow. The resulting product was ground in an agate mortar for 10 mins then was mixed into a 0.5 M H₂SO₄ solution at 80 °C and was stirred for 2 hours. Afterward, it was extracted using a vacuum filter and then was thoroughly rinsed with ultra-pure water followed by being dried in 60°C air for 4 hours. Finally, the product was heat treated a second time in 100 mL/min N₂ flow at 900 °C for 3 hours to complete the CTNC-Fe catalyst. Pristine CTNC was made from stabilized BCP heat treated at 600 °C for 30 minutes and then at 900 °C for 3 hours under nitrogen flow.

3.3.4 Testing Electrochemical Activity

Measurements of electrochemical activity were captured using rotary disk electrode (RDE) potentiometry. An ink was prepared using 5 mg of catalyst with 40 µL of 5% Nafion solution in alcohol dissolved in 0.5 mL n-propanol. The ink was sonicated in an ice bath for 1 hour and an aliquot of 17 µL was casted onto the glassy carbon electrode for a 0.8 mg/cm² catalyst loading. A 0.5 M sulfuric acid solution at room temperature with a mercury/mercurous sulfate reference electrode and a graphite counter electrode was used. Cyclic voltammetry was implemented from 0 to 1 V (vs. NHE) in 50 mV/sec steps at 200 rpm in nitrogen flow and chronoamperometry scans were captured at 50 mV per 30 second steps at 900 rpm under oxygen flow.

3.3.5 Materials Characterization

The polymer solution monomer conversion rate was tested at different times during the polymerization process to ensure proper controlled/ “living” radical polymerization using proton nuclear magnetic resonance ($^1\text{H-NMR}$). Polymer molecular mass and distribution was tested using gel permeation chromatography (GPC) equipped with a Wyatt Optilab T-rEX refractive index (RI) detector, using DMF as the mobile phase. Carbon and nitrogen content of the catalyst was found by volatilization of the catalyst and separately measuring the evaporated nitrogen and carbon products; this analysis was performed by MidwestMicro Labs and was used to accurately estimate the total amounts of N in the sample. Iron content was determined by energy dispersive spectroscopy (EDS) using a Quanta 600 Scanning Electron Microscope. The nature of the bonding of heteroatoms in the carbon matrix was determined using X-ray photoelectron spectroscopy (XPS) and X-ray diffraction (XRD) and the surface area and pore size were measured using Brunauer-Emmett-Teller (BET) surface area analysis. Powder samples were first degassed at 120 °C for at least 4 hours before N_2 sorption measurement. The micropores were analyzed using the t-plot method with the Halsey equation. The slope of the t-plot was used to calculate the external SSA, while the micropore surface area (S_{micro}) was obtained from subtracting S_{external} from S_{BET} . The mesoporous size distribution was obtained from Barrett-Joyner-Halenda (BJH) method from the adsorption branch with KJS correction. Finally, the presence of mesopores was tested using a JEOL JEM 2000EX transmission electron microscope (TEM).

3.3.6 Fuel Cell Testing

The catalyst ink was prepared in a 9:1 isopropanol and water solvent mixture with an ionomer to catalyst ratio of 0.6:1 and a solvent to ionomer ratio of 59:1. The ink was sonicated in an ice bath for 2 hours then blade coated onto a Freudenberg H23C6 gas diffusion layer with a

loading of 4 mg/cm², this served as the cathode. A commercially available 10% Pt/C gas diffusion electrode with a 0.3 mg_{Pt}/cm² loading was used for the anode. Both electrodes were hot-pressed onto a Nafion 212 membrane at a temperature of 130 °C and a pressure of 2.7 MPa to create the membrane electrode assembly (MEA).

The MEA was installed into commercial 5 cm² fuel cell hardware connected to a fuel cell stand for gas delivery and cell heating (Scribner Associates Inc., Southern Pines, NC). A BioLogic VSP Potentiostat was used to perform the polarization tests to characterize the fuel cell's overall performance. The cell was conditioned by purging with nitrogen on both anode and cathode at 100 % relative humidity, 80 °C temperature, and 50 kPa backpressure for two hours. For cyclic voltammetry, the gas flow in the anode was switched to 200 mL/min and for the polarization test the cathode gas flow was switched to 1 L/min of oxygen, both with 100 % relative humidity and 50 kPa backpressure. Each voltage step was held for 30 seconds and then averaged from the last 10 seconds of current readings during analysis.

3.4 Results and Discussion

3.4.1 Morphology and Porosity of the Catalyst

The pristine CTNC obtained from the stabilized block copolymer (Fig. 3.2a) was characterized as an isotropic structure of interconnected pores and channels. The CTNC-Fe catalyst in Fig. 3.2b shows that the interconnected pores were largely maintained. Figure 3.3 demonstrates the uniformity of the porous structure at lower magnification TEM scans. Further analysis was performed throughout the synthesis of the catalyst: one after the first heat treatment at 600 °C (Fig. 3.2c) and another after acid treatment (Fig 3.2d). Fig 3.2d shows less uniformity in the nanostructure which is likely due to residues from the acid treatment clogging the porous structure. This was corroborated by BET surface area analysis, which shows that CTNC-Fe after

the acid treatment (CTNC-Fe-AT) had a surface area of approximately half of the completed CTNC-Fe catalyst (Table 3.1).

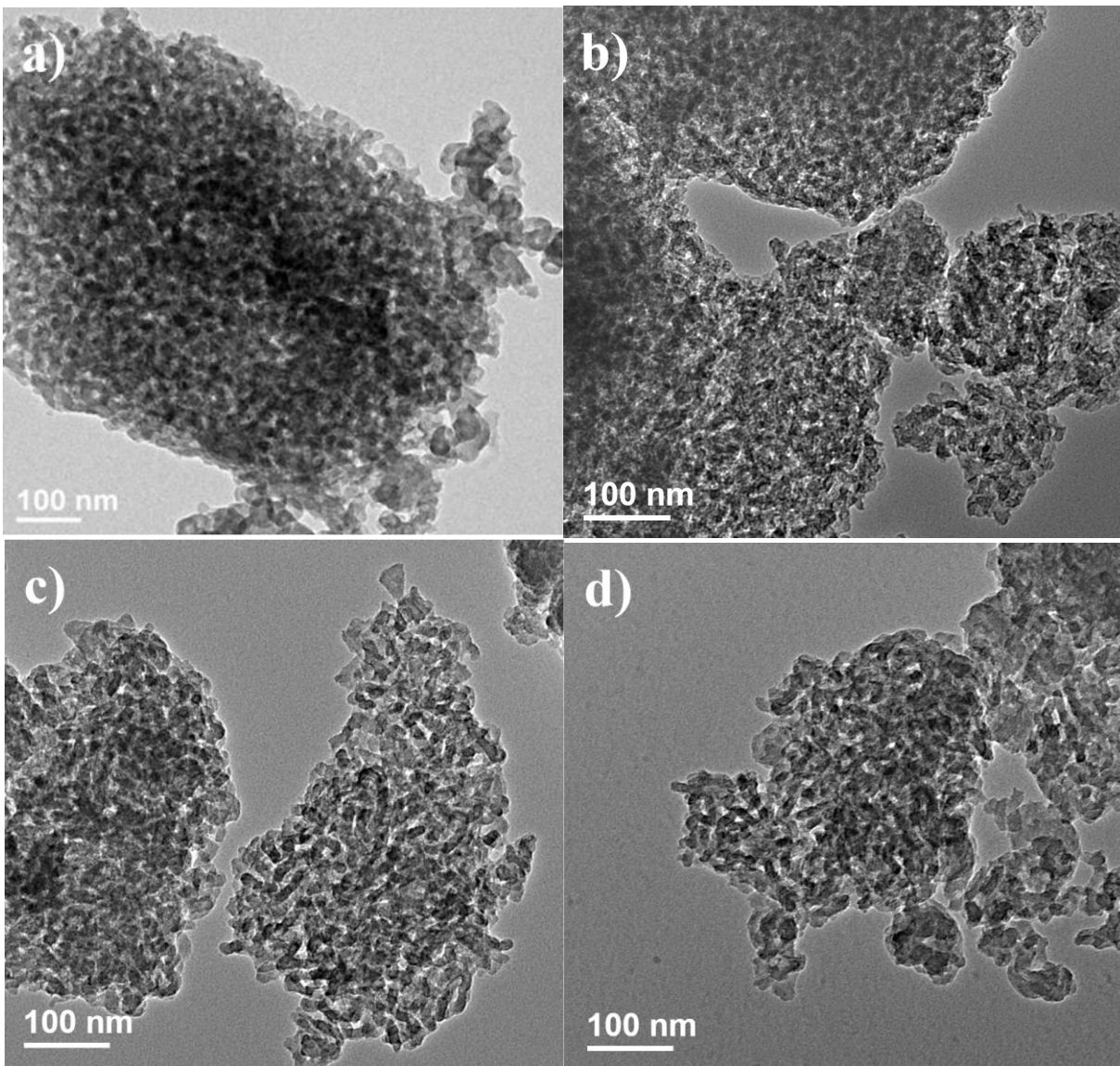


Figure 3.2. TEM photographs of pristine CTNC and CTNC-Fe catalyst at different stages during synthesis. a) Pristine CTNC (P-CTNC), b) CTNC-Fe Catalyst, c) CTNC-Fe after first heat treatment at 600 °C, and d) CTNC-Fe after acid treatment.

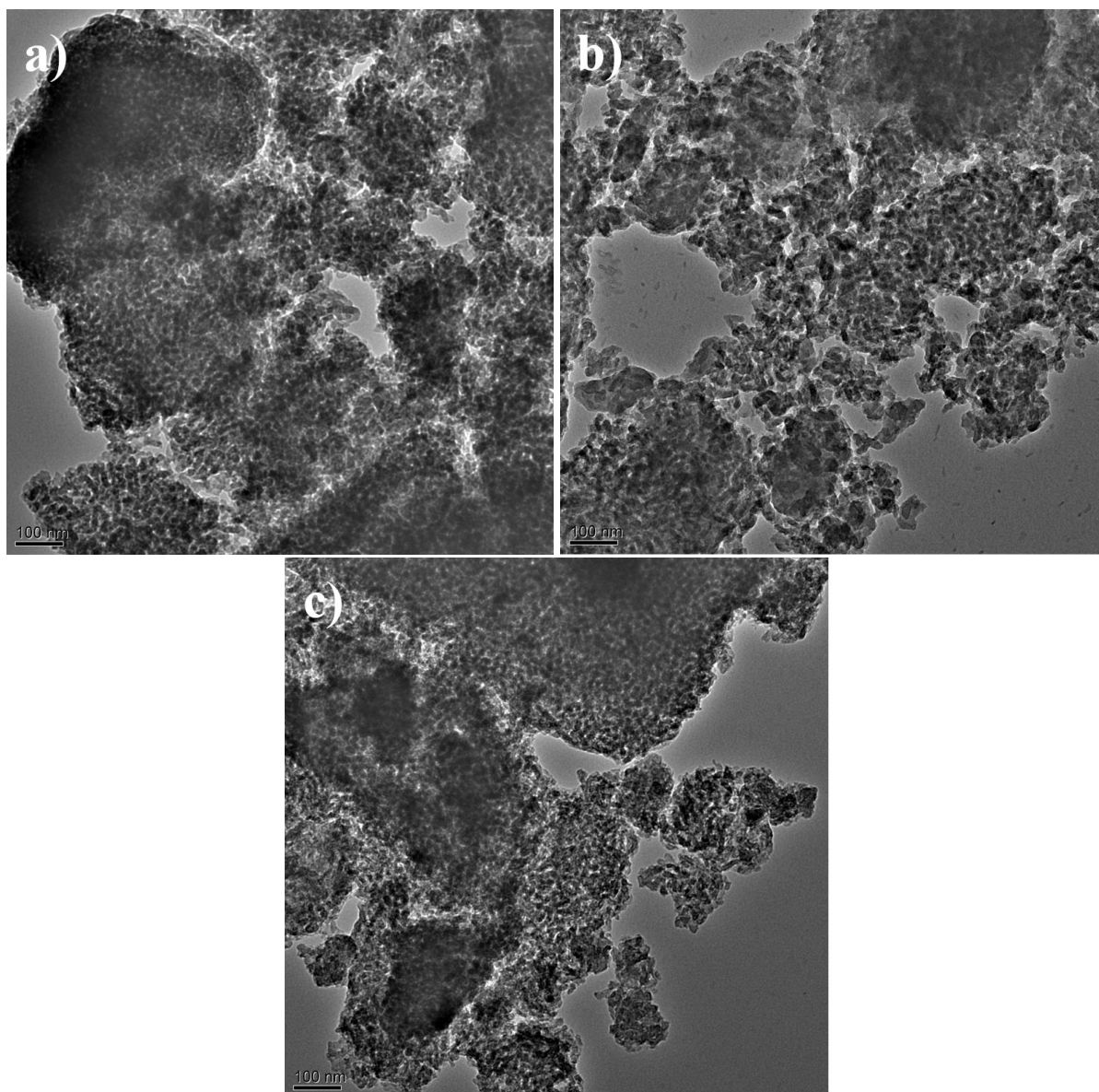


Figure 3.3. TEM scan photographs of CTNC-Fe during various stages of the synthesis process. a) CTNC-Fe after heat treatment at 600 °C for 30 mins, b) CTNC-Fe after treatment in 0.5 M H₂SO₄ solution at 80 °C, and c) Completed CTNC-Fe catalyst, after 900 °C heat treatment for 3 hours.

Figure 3.4 displays the BET N₂ adsorption-desorption isotherms and pore-width distribution of different CTNC samples during the synthesis process. The CTNC-Fe appears to undergo surface activation due to the acid treatment and the heat treatment at 900 °C, since the mesoporous surface area remains almost completely unchanged (227 m²/g after the first heat

treatment and 231.1 m²/g after the second heat treatment). However, Fe-doping only had minor effects on the nitrogen sorption isotherms (Fig. 3.4a) and the pore size distribution (Fig. 3.4b). In addition, the average pore size of the CTNC-Fe catalyst is approximately the same as P-CTNC at similar heat treatment conditions (Table 3.1), despite the total surface area of CTNC-Fe being 25% lower than that of P-CTNC.

Table 3.1. BET surface area analysis results for CTNC-Fe catalyst after first heat treatment (CTNC-Fe-600), after acid treatment (CTNC-Fe-AT) and after completion of the synthesis process (CTNC-Fe). P-CTNC-600 is pristine CTNC with similar heat treatment to CTNC-Fe-600 and P-CTNC has similar heat treatment to CTNC-Fe.

Sample	Total Surface area (m ² /g)	Micropore (m ² /g)	Mesopore (m ² /g)	Average pore size (nm)
CTNC-Fe	395.8	164.7	231.1	8.10
CTNC-Fe-600	332.7	105.7	227.0	8.67
CTNC-Fe-AT	183.1	34.6	148.6	9.58
P-CTNC-600	392.7	158.9	233.8	9.36
P-CTNC	528.6	276.4	252.2	8.72

As observed in Table 3.1, the difference in the surface area was mostly in the microporous region. This suggests that the addition of the iron precursor mainly affected the micropores, leaving the mesoporous region largely intact. The decrease in the surface area of micropores could potentially affect mass transport leading to excessive overpotential in the performance of the catalyst. However, as seen in Table 3.1, the acid treatment has a surface activation effect without significantly affecting the mesoporous region (when comparing CTNC-Fe to CTNC-Fe-600). Therefore, it is likely that a controlled amount of surface activation could negate the reduction of surface area effects caused by the introduction of iron to CTNC.

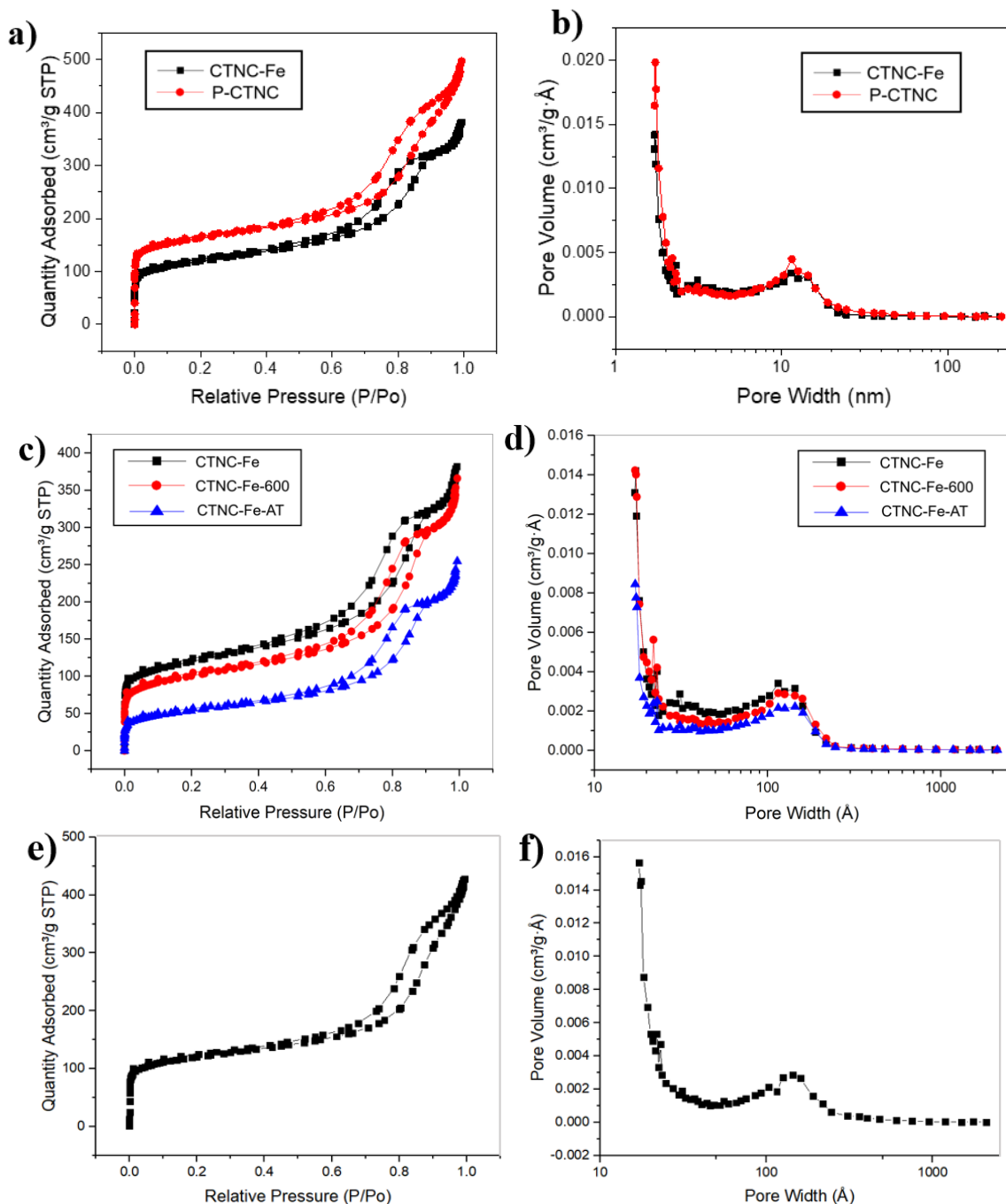


Figure 3.4. BET surface area analysis results for a)-b) CTNC-Fe catalyst and pristine CTNC (P-CTNC), c)-d) CTNC-Fe during the synthesis process and e)-f) pristine CTNC heat treated at 600 °C. Nitrogen adsorption-desorption isotherms at -196 °C on the left and pore size distribution on the right.

3.4.2 Elemental Analysis and the Influence of Fe-doping

The nitrogen and iron species present in CTNC-Fe were analyzed by high resolution XPS (Fig. 3.5). For the N-1s XPS signal (Fig. 3.5a), three main peaks at 399 eV (25.7 at%), 401.1 eV (48.8 at%) and 403 eV (25.4 at%) were observed. The peak at 403 eV can be identified as oxidized N,^{59,89,92} and the peak at 401.2 eV can either represent pyrrolic/quaternary N^{59,89} or graphitic N.⁹² The peak with the binding energy of 399 eV was identified as either N-Fe moieties^{57,84,94} or pyridinic N.^{58,59} According to the N-1s XPS spectra obtained from P-CTNC (Fig. 3.5f), the pyridinic N peak for this material is 398.6 eV. Thus, the 399 eV peak in CTNC-Fe in Figure 3.5a is more likely related to either N-Fe moieties, the Fe being coordinated by pyridinic N, or there is a mixture of N-Fe and pyridinic N. The same can be said for the pyrrolic/graphitic N peak as it manifests at 400.8 eV in P-CTNC (Figure 3.5f). The presence of Fe in CTNC-Fe increased the deconvoluted peak energy values of pyridinic N and pyrrolic/graphitic N approximately 0.4 eV, which means it is likely that N-Fe moieties are composed of not just pyridinic N but also graphitic and pyrrolic N.⁶⁵ Furthermore, the atom percent of pyrrolic and graphitic N is almost double that of pyridinic N as seen in Table 3.2. Therefore, even if it was less energetically favorable for Fe to interact with graphitic and pyrrolic N to form FeN_x active sites than it is with pyridinic N, the greater concentration of these N species would make up for it.

Fe-2p spectra (Fig. 3.5b), showed four peaks at 710.8 eV, 715.4 eV, 724 eV and 729.3 eV upon deconvolution. The two lower peaks at 710.8 eV and 715.4 eV pertain to Fe 2p_{3/2}. The binding energy of the main peak and satellite peak indicated that the catalyst likely contains both Fe²⁺ and Fe³⁺ with a larger fraction of Fe²⁺ as shown by the higher intensity of the lower energy peaks.^{84,90} The two higher-binding-energy peaks at 724 eV and 729.3 eV represent Fe 2p_{1/2}.⁹¹

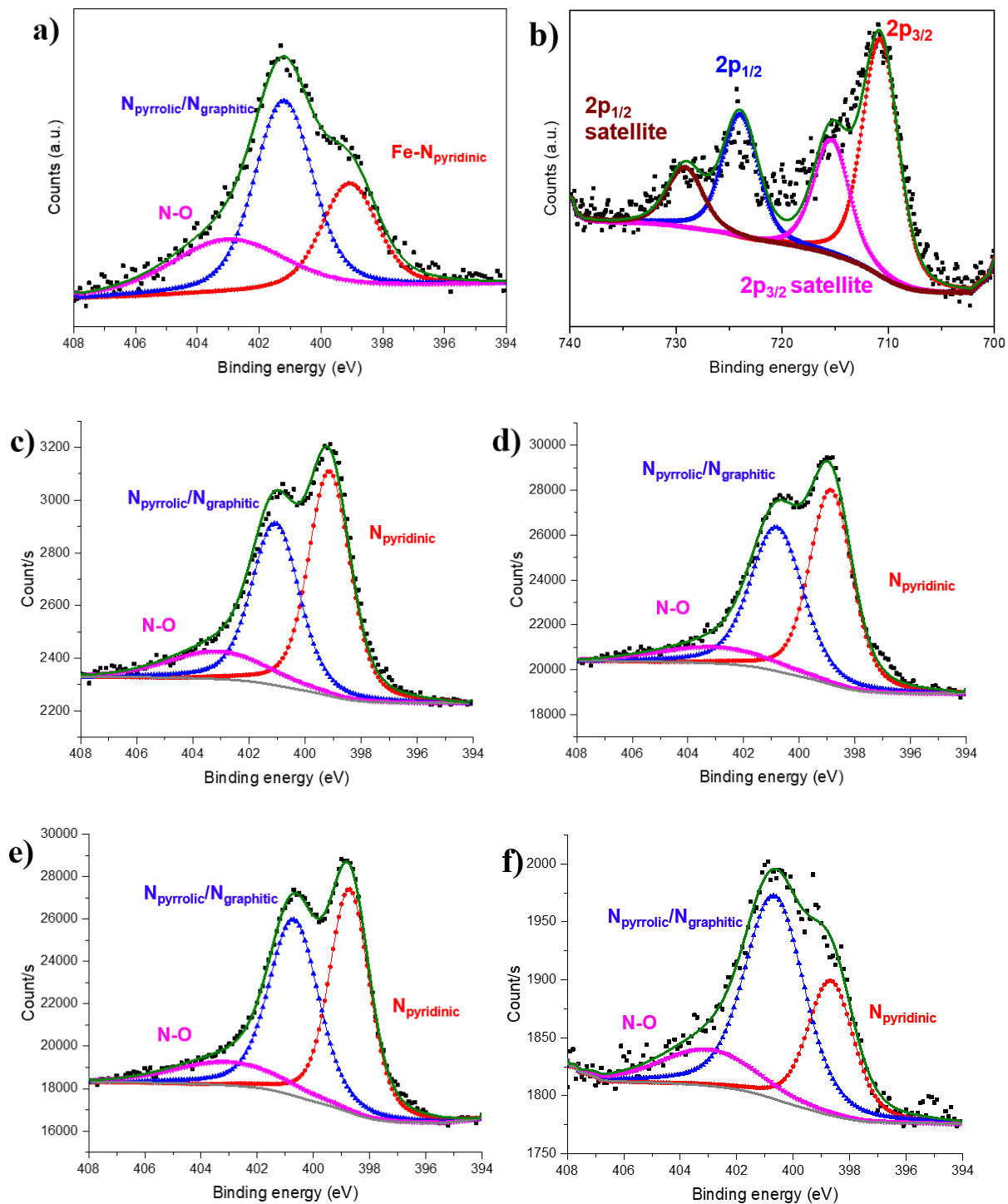


Figure 3.5. High resolution XPS spectra of a) CTNC-Fe N 1s, b) CTNC-Fe Fe 2p, c) CTNC-Fe-600 N 1s, d) CTNC-Fe-AT N 1s, e) CTNC-600 and f) P-CTNC N 1s. Peak shape of Gaussian/Lorentzian convolve was used for the fitting, with a L/G Mix ratio of 30% for all peaks.

This mix of oxidation states is likely a result of the following processes. On one hand, the highly oxidative H₂SO₄ during the synthesis of CTNC-Fe could possibly oxidize Fe²⁺ to Fe³⁺. On the other hand, the N-rich graphitic carbon could provide a reducing environment to regenerate Fe²⁺ from the newly formed Fe³⁺ species.

Table 3.2. Nitrogen species amounts calculated from N 1s deconvoluted peaks analysis for CTNC-Fe and pristine CTNC.

Binding Energy (eV)	Pyridinic N (%)	Pyrrolic/Graphitic N (%)	N-O (%)
CTNC-Fe	25.7	48.8	25.4
CTNC-Fe-600	47.5	39.1	13.4
CTNC-Fe-AT	47.0	43.0	10.0
CTNC-600	44.4	43.6	12.0
P-CTNC	24.5	55.9	15.4

Table 3.3. Elemental composition of CTNC-Fe catalyst throughout the synthesis process and pristine CTNC.

Analysis Type	Sample	N (wt%)	Fe (wt%)	C (wt%)	S (wt %)
XPS	CTNC-Fe	4.2	< 0.5	95.8	0
	CTNC-Fe-600	10.8	<0.5	89.2	0
	CTNC-Fe-AT	14.2	<0.5	84.1	1.7
	P-CTNC	3.2	0	95.5	0
	P-CTNC-600	13.7	0	86.3	0
EDS	CTNC-Fe	1.4	12.04	83.5	1.45
	CTNC-Fe-600	7.11	12.18	76.23	1.95
	CTNC-Fe-AT	8.73	7.17	75.99	3.42
Elemental Analysis	CTNC-Fe	5.3	-	82.6	-
	CTNC-Fe-600	16.5	-	63.6	-
	CTNC-Fe-AT	16.1	-	62.6	-

The elemental composition was also analyzed by dispersive X-ray electron spectroscopy (EDS, Fig. 3.6) and combustion based elemental analysis. As seen in Table 3.3, less than 0.5 wt% iron in CTNC-Fe catalyst was detected according to XPS, whereas EDS showed a value of 12.04 wt% iron in the catalyst. Considering that EDS has substantially greater penetration depth than XPS, this discrepancy would suggest that either most of the Fe is trapped in the carbon matrix or is too deep inside the mesoporous structure for the XPS signal to be detected. Figure 3.7 showed there were many massive particles close to and above 10 μm in diameter, which would indeed make it difficult for XPS to detect Fe.

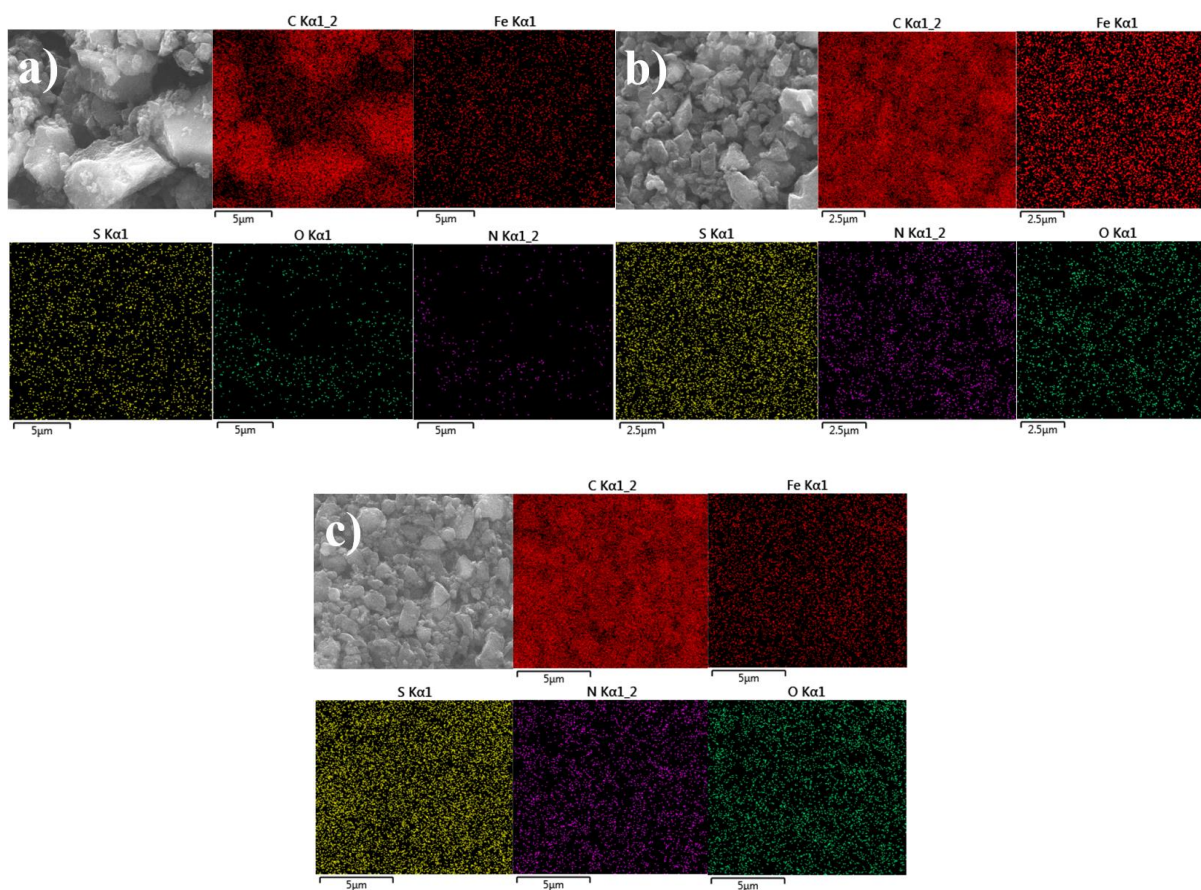


Figure 3.6. Energy dispersive x-ray spectroscopy (EDS) scan of CTNC-Fe at three steps during synthesis a) CTNC-Fe, b) CTNC-Fe-600, and c) CTNC-Fe-AT.

Furthermore, according to the EDS elemental analysis in Fig. 3.6 and listed in Table 3.3, acid treatment significantly reduced the Fe content from 12.18 wt% in CTNC-Fe-600 to 7.17 wt% in CTNC-Fe-AT. Since the carbon content remained similar during the acid treatment it can be inferred that approximately 40% of Fe initially included in the CTNC-Fe mixture during synthesis formed metallic Fe and other unstable species that were washed away by the acid treatment.

In addition, comparison of N content between XPS and the results obtained by gasification elemental analysis shows that the nitrogen present in CTNC-Fe is not completely present in the surface of the catalyst. There is some noticeable, if not substantially significant, amount of nitrogen that remains trapped in the carbon matrix. To improve on this catalyst, the method of synthesis will need to be adjusted so that CTNC-Fe is able to retain more of the nitrogen content when heat treated at higher temperatures than 600 °C and to affect N heteroatom migration from the bulk of the carbon to the surface.

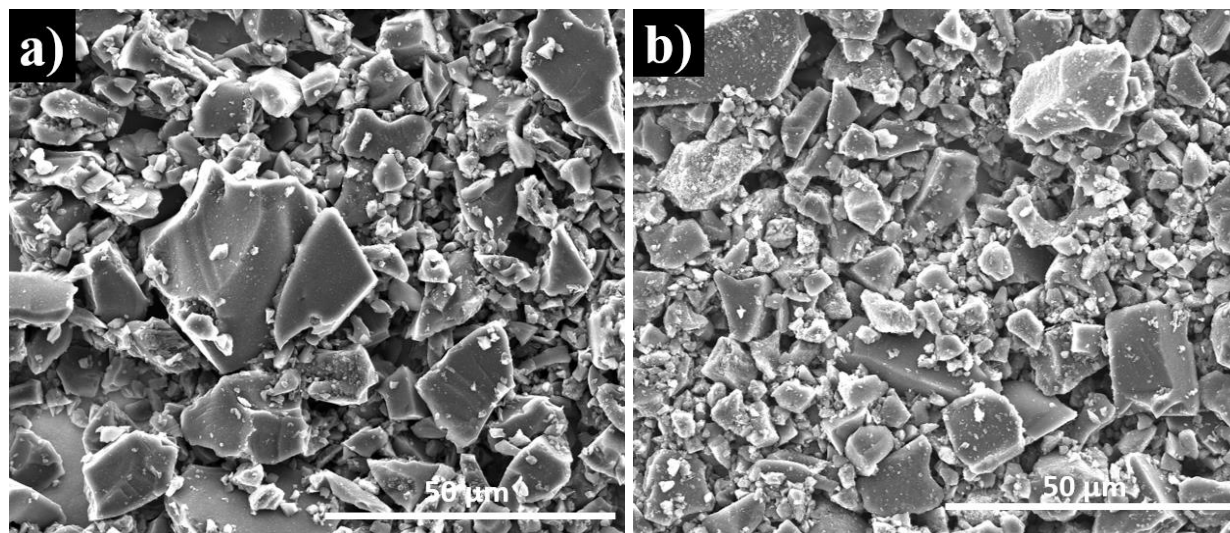


Figure 3.7. SEM photograph scans of the particle size and structure of a) P-CTNC and b) CTNC-Fe.

Regarding S content, there was none detected by XPS except in the case of CTNC-Fe after acid treatment with sulfuric acid, which is attributed to remnants from the acid treatment (Fig. 3.8).

As observed with Fe, EDS analysis showed significantly higher S content in the catalyst (Fig. 3.6), which points to sulfur being either trapped in the carbon matrix at a depth outside the range of XPS or deep inside the mesoporous structure that cannot be accessed due to CTNC-Fe particle size. This is supported by the lower surface area value of CTNC-Fe-AT, the catalyst tested right after the acid treatments, which suggests that there are some trapped residues from the acid washing that remain before final heat treatment at 900 °C. Since S content decreases after the final heat treatment then it is likely that these trapped residues were volatilized during the heat treatment.

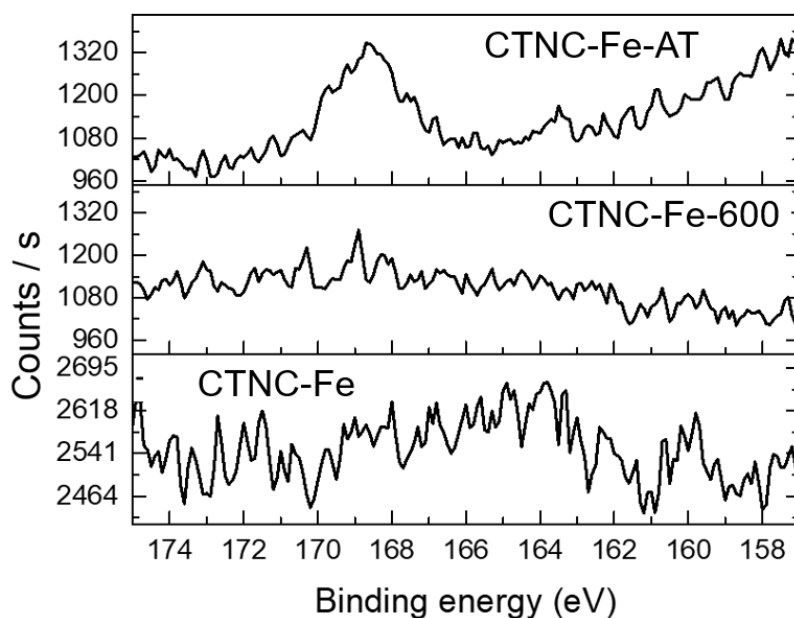


Figure 3.8. High resolution XPS S 2p spectra for CTNC-Fe at different steps during synthesis.

Moreover, high resolution XPS spectra for C 1s produced two deconvoluted peaks at 285.2 eV (84.0 at%) and 288.7 eV (16.0 at%) which can be attributed to a mixture of graphitic and amorphous carbon for the former, more likely graphitic according to Lesiak et al,⁹⁴ and for more complex coordination involving Fe, N and O for the latter. The value of graphitic carbon for CTNC-Fe was only slightly lower than pristine CTNC as seen in Fig. 3.9 and Table 3.4. Therefore,

we conclude that the addition of an iron precursor, in this case FeSO₄, had little effect in the chemical structure of the carbon.

The addition of iron to CTNC also had a pronounced effect on the XRD patterns of CTNC-Fe (Fig. 3.10) compared to pristine CTNC.⁷¹ Although the Bragg peaks at 25°, 44.3° and 82° (peaks associated with the presence of nanographitic structures commonly observed in pyrolytic carbons⁹⁵), are still present the one at 25° almost completely disappeared. We observed additional peaks at 38.5°, 65.3° and 78.3° which are likely associated with iron oxide particles or other type of crystallites such as FeS or CFe_{15.1}.⁴⁶ Analysis of the basal plane crystallite sizes calculated from the width of the (100) peak using the Scherrer Equation⁹⁶ produced a value of 4.6 nm for the carbon crystallite sizes.

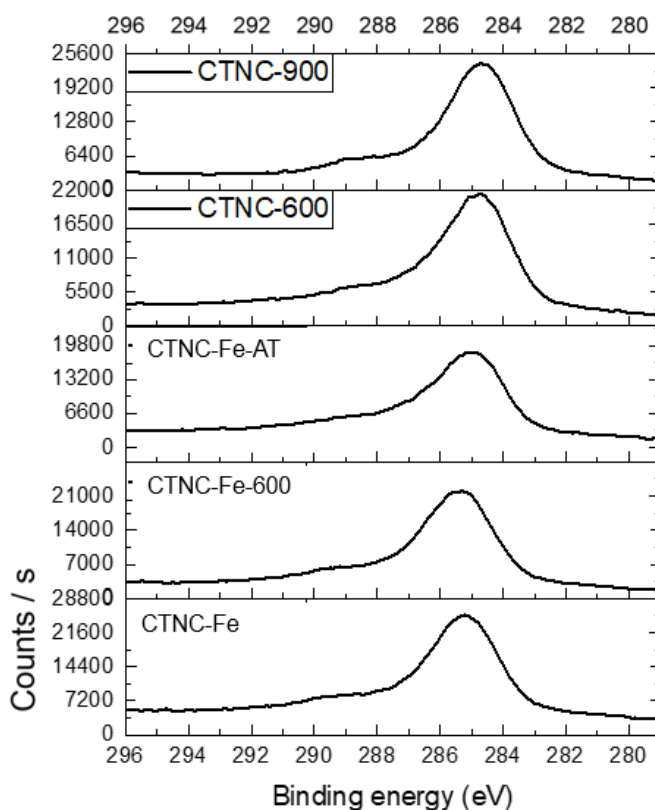


Figure 3.9. High resolution XPS C 1s spectra for CTNC-Fe at different steps during synthesis and pristine CTNC.

Table 3.4. C 1s deconvoluted peaks analysis for CTNC-Fe and pristine CTNC.

Binding Energy (eV)	285.2 eV	288.7 eV
CTNC-Fe	84.0	16.0
CTNC-Fe-600	83.5	16.5
CTNC-Fe-AT	80.3	19.7
CTNC-600	82.9	17.1
CTNC-900	85.8	14.4

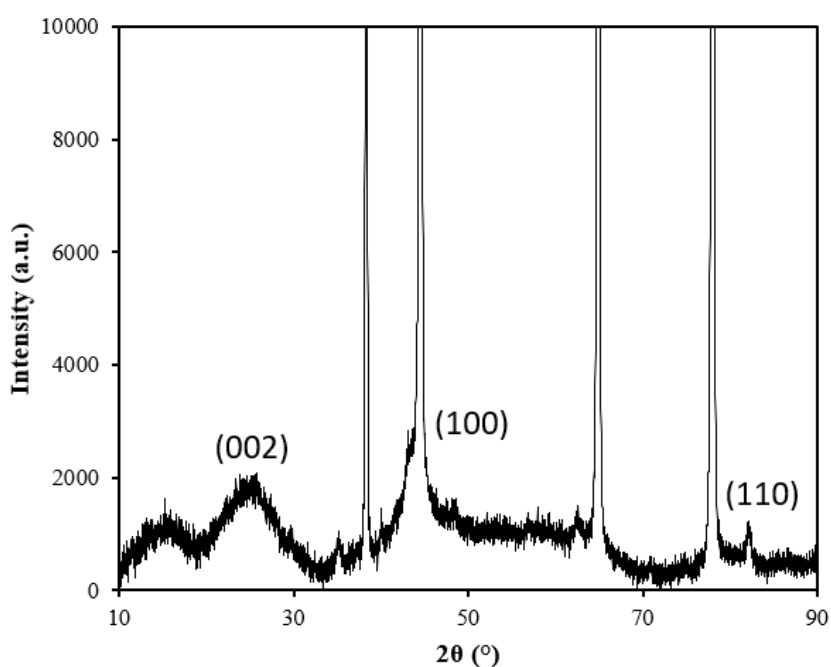


Figure 3.10. XRD profile of CTNC-Fe catalyst with labeled diffraction peaks for detecting π -stacking of nanographitic platelets (002) and assessing their lateral size (100).

3.4.3 Electrochemical Activity and Fuel Cell Performance

Although to this point, only one type of CTNC (obtained from the PBA₆₀-b-PAN₁₀₃ copolymer) was tested, we have been able to design a synthesis process that produces CTNC-Fe catalyst with significant electrochemical activity (Fig. 3.11). CTNC-Fe also served as a PGM-free catalyst for hydrogen fuel cells (Fig. 3.12). The best sample obtained to date has achieved a half-

wave potential of 0.781 V vs NHE with a limiting current density of approximately 3.5 mA/cm² as seen in Figure 3.11a. As with some of the characterization techniques used, we measured the electrochemical activity of the catalyst at different steps of the synthesis process. The half-wave potential for CTNC-Fe-600 was 0.631 V vs NHE, which is likely related to the low heat treatment temperature (600 °C) that resulted in insufficient electrical conductivity. However, the half-wave potential increases to 0.706 V vs NHE after the acid treatment (CTNC-Fe-AT). It is uncertain what may cause this effect since the actual surface area decreases according to the BET results seen in Table 3.1.

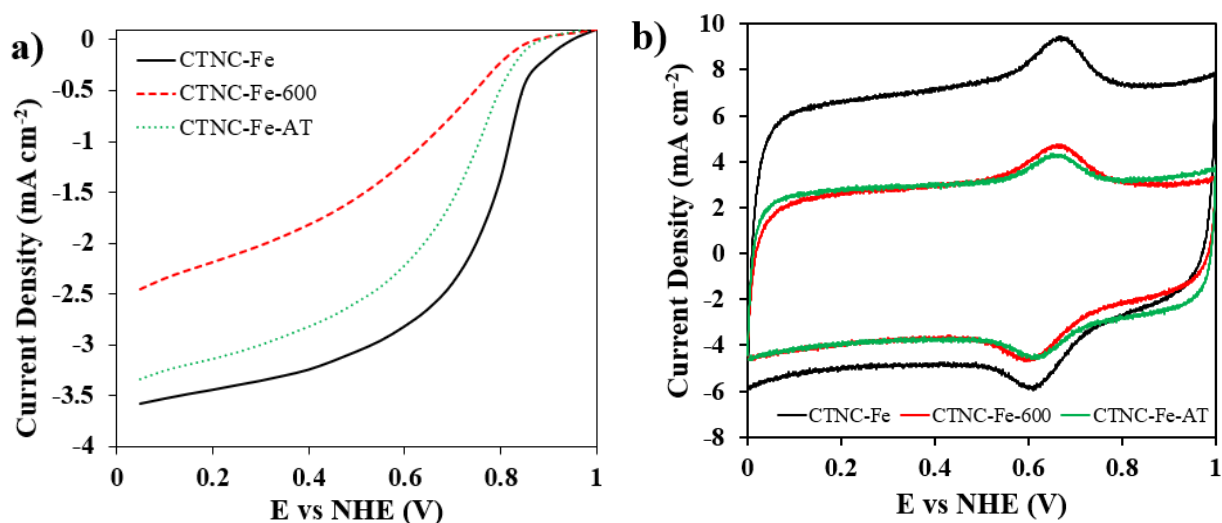


Figure 3.11. Electrochemical activity results on ORR of the CTNC-Fe catalyst tested at different steps in the synthesis process. a) Polarization curve of ORR in acidic environment obtained using chronoamperometry scans in oxygen saturated 0.5 M H₂SO₄ solution at room temperature. b) Cyclic voltammetry curve obtained in nitrogen saturated 0.5 M H₂SO₄ solution at room temperature.

In addition, Figure 3.11b shows a similar capacitive surface area response as noted by the cyclic voltammetry curves showing negligible differences. Therefore, it is likely that the increase in electrochemical activity from CTNC-Fe-600 to CTNC-Fe-AT might be due to the increase in

surface exposed nitrogen as shown by the XPS results in Table 3.3. Corrosion of the carbon by the acid treatment is likely the source of the increase in surface exposed nitrogen, which is lost to volatilization after the final heat treatment at 900 °C. This behavior is inherent to CTNC materials as observed by Zhong et al.³⁴

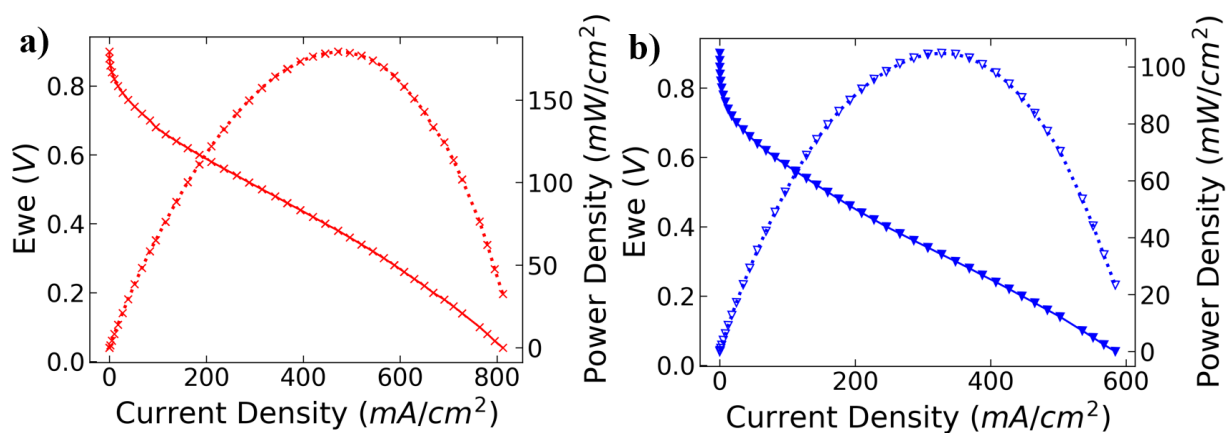


Figure 3.12. Results of fuel cell tests performed using a 4 mg/cm² CTNC-Fe cathode and 0.3 mg/cm² anode at 80 °C, 100% relative humidity, 50 kPa backpressure hydrogen in the anode and either a) 100% relative humidity, 50 kPa backpressure oxygen or b) 100% relative humidity, 50 kPa backpressure air in the anode.

The open circuit voltage for the fuel cell using pure oxygen flow reached 0.881 V. In terms of activity, the fuel cell was able to reach an activity of 17.9 mA/cm² (4.38 A/g) at a cell voltage of 0.8 V and 83.8 mA/cm² (20.85 A/g) at 0.7 V in addition to maximum power densities of 180 mW/cm² with pure oxygen flow in the cathode (Fig. 3.12a) and 105 mW/cm² with air flow (Fig. 3.12b). This was achieved despite the large particle sizes shown in the SEM images from Figure 3.7 which produced an electrode thickness of 78.3 μm, which is the likely cause of large ohmic overpotential issues. This is shown by the potentiostatic electrochemical impedance spectroscopy curve (Fig. 3.13) which produced a high-frequency resistance (HFR) of 0.065 Ω due to contact resistance. This value is significantly higher than the expected 0.01 Ω proton conduction resistance

of the Nafion 212 membrane. Furthermore, the apparent resistance of the fuel cell, obtained by calculating the slope of the IV curve in the linear (Ohmic) region, was 0.15Ω , which is three times the measured HFR. High apparent ohmic resistances in PGM-free cathode fuel cell polarization curves are often due to a liquid water saturated cathode in which the proton conduction across the flooded catalyst layer to the active zone at the hydrophobic MPL interface leads to a large ohmic loss that is not captured by EIS due to the electrode capacitance.⁹⁷

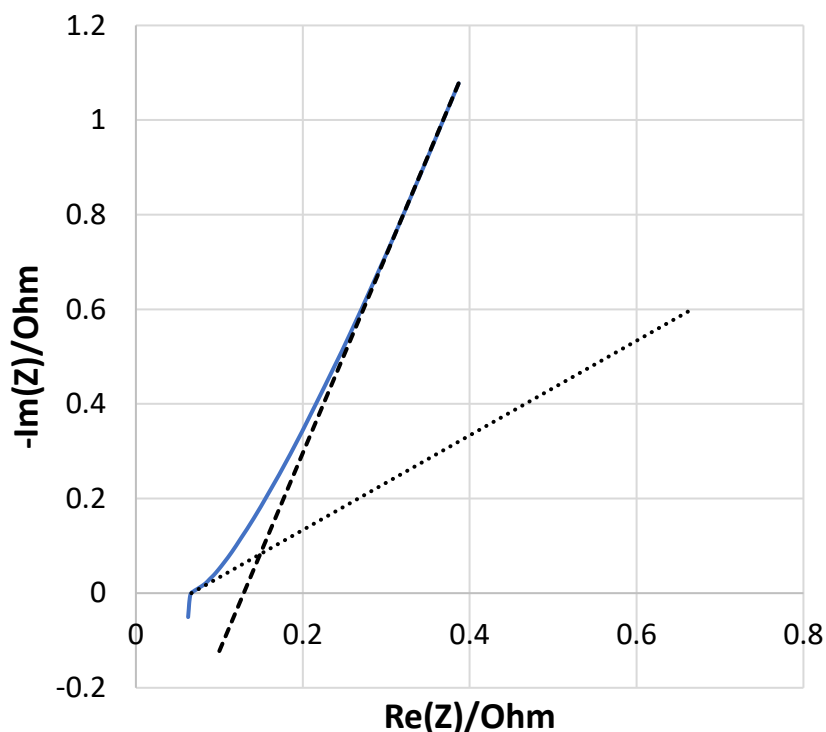


Figure 3.13. Potentiostatic electrochemical impedance spectroscopy scan of membrane electrode assembly with CTNC-Fe catalyst.

Furthermore, as seen in Fig. 3.14, the capacitive surface area of the electrode according to the cyclic voltammetry curve of the fuel cell showed a value of $238.7 \text{ m}^2/\text{g}$. This is significantly lower than the surface area value obtained using BET and no doubt led a small fraction of macropore formation which could be a cause of flooding.⁹⁷ Considering these fuel cell testing

results, a key area of future work is the control of the catalyst aggregate size, with a smaller, more uniform distribution of catalyst aggregate sizes. Conversely, perhaps a different amount of ionomer and a CTNC-Fe catalyst-optimized method of electrode preparation would produce higher fuel cell performance. Future work will include experimentation with CTNC-Fe electrode composition, thickness and assembling in MEA.

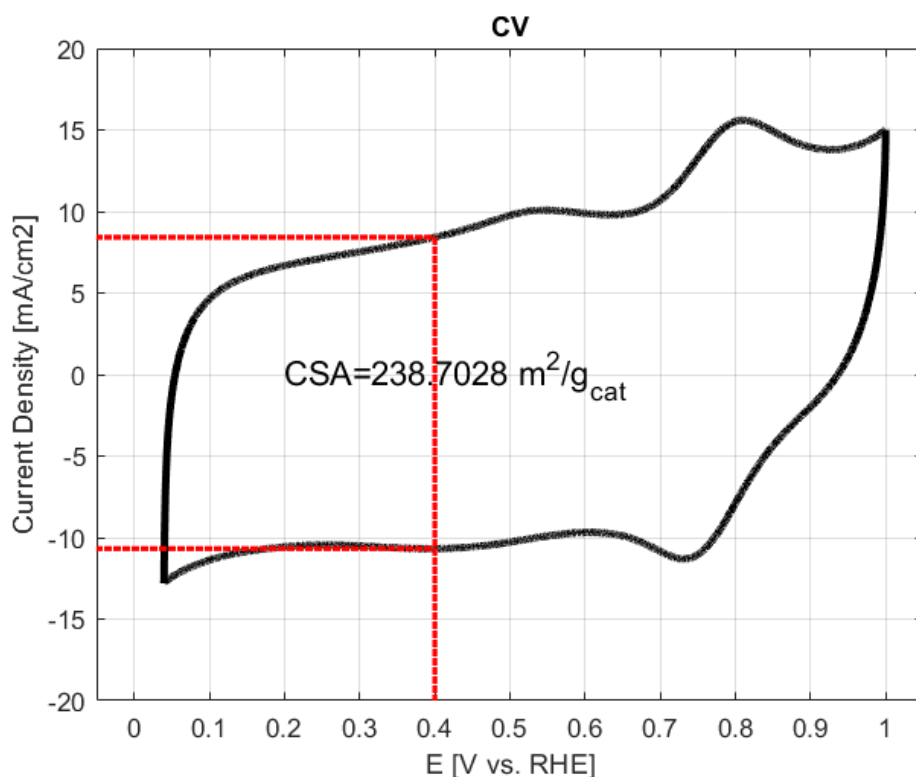


Figure 3.14. Cyclic voltammetry curve of fuel cell with CTNC-Fe cathode performed using N₂ flow with 100% RH at 80 °C with 50 kPa backpressure.

While the electrochemical activity of CTNC-Fe is not the highest when compared to other catalysts currently under development, its half-wave potential is higher than average.⁹⁷ In addition, CTNC-Fe is at an early stage of development compared to current top PGM-free catalysts. For example, the CM + PANI-Fe-C(Zn) catalyst mentioned in Table 2 in Beltran et al,⁵³ has a half-wave potential of 0.83 V vs NHE as of 2017. However, at the beginning of its development in

2008 the half-wave potential was approximately 0.75 V vs NHE.⁹⁸ Likewise, metal organic framework derived PGM-free catalysts currently reach some of the highest electrochemical activities above 0.85 V vs NHE according to recent work,⁹⁹ however, in 2010 when the catalyst was first reported⁸ the catalyst had a half-wave potential of 0.77 vs NHE. On the other hand, commercial catalysts such as those based on silica templating,¹⁰⁰ have low half-wave potentials (around 0.7 V vs NHE) but have great stability and durability.¹⁰⁰ Therefore, CTNC-Fe, is very well on its way as our group continues to experiment on it.

3.5 Conclusions

The PGM-Free catalyst, CTNC-Fe, was synthesized by Fe-doping a copolymer templated nitrogen rich carbon obtained from the copolymer PAN₁₀₃-b-PBA₆₀. The copolymer was the base of the catalyst where the PAN phase was the source of carbon and nitrogen and the PBA phase acted as a sacrificial component to generate a mesoporous structure. The nanostructure was controlled by the length and ratio of lengths of the polymer blocks to produce a bicontinuous morphology with an interconnected pore nanostructure. The morphology of the catalyst mesoporous structure was confirmed using BET surface area analysis and TEM and the composition and presence of FeN_x were analyzed by use of EDS and XPS. RDE potentiometry was used to test the electrochemical activity of the catalyst in an acidic environment and a fuel cell test with oxygen/air flows in the cathode and hydrogen gas flow in the anode was used to confirm its feasibility as an actual fuel cell catalyst. The catalyst achieved a 0.781 V vs NHE half-wave potential, and the fuel cell produced a maximum power of 180 mW/cm² which proved that the catalyst could perform ORR in a proton exchange membrane fuel cell. Further research on this topic is expected to continue improving on CTNC-Fe as it has done to its present state. Possible areas of future improvement on CTNC-Fe catalyst are the issue of particle size, nitrogen retention

at heat treatment temperatures over 600 °C and increase in pore surface area either by chemical treatment surface activation or by manipulation of the polymer blocks to produce a more efficient pore structure. This last method specifically makes the use of CTNC as a base for an Fe-N-C catalyst a unique and novel undertaking, not limited to affecting mass transport in fuel cell operation but also by the effects of pore structure on formation of Fe-N moieties which serve as catalytic active sites as theorized in previous works.^{48,49} By studying the effects of minor changes in pore size and structure afforded by the fine control and tunability of CTNC with the use of controlled/ “living” radical polymerization methods on the formation of active sites and electrochemical activity of CTNC-Fe, we aim to design a catalyst that may eventually reach the goal of matching and even surpassing the electrochemical activity of platinum group metal catalysts.

Chapter 4: Using Poly(vinyl-ferrocene)

Metallopolymer as an Iron Precursor in

CTNC-Fe Catalyst Synthesis

4.1 Introduction

The formation of active sites in Fe-N-C catalysts such as CTNC-Fe is dependent on many different factors which include nitrogen concentration, transition metal concentration, high surface area, heat treatment temperature, the process used to N/Fe-dope the carbon base of the catalyst, etc. A main step used in the synthesis process of Fe-N-C catalyst is acid washing,^{26,28,30,36,37,44,45,55-59,91} a pivotal step in both maximizing the usage of the iron and removing unstable species such as metallic Fe aggregates which tend to hinder mass transport when they block pores. To achieve a high electrochemical activity a large amount of iron and nitrogen is needed to penetrate through the mesoporous structure of the carbon base, however, there is an optimal maximum amount of Fe precursor that can be used before the carbon pore structure is clogged. Furthermore, too much iron tends to lead to nucleation more readily than formation of ligands with the nitrogen moieties present in the carbon surface.

Acid washing is also an important step of CTNC-Fe synthesis, and though we have attempted to increase the iron content to increase ORR electrochemical activity, as seen in Chapter 2, we encountered surface area reduction effects even when using acid treatments. Chapter 3 also shows that there is a minor amount of surface activation present when using acid washing with 0.5

M H₂SO₄ solution for 2 hours at 80 °C, therefore, if we attempted to perform a more rigorous acid washing process at higher temperatures, for a longer duration, or with higher acid concentration we would risk both degradation of catalytic active sites and destruction of the mesoporous nanostructure as previously observed when using surface activation with KOH.⁷¹

Consequently, we experimented with the use of a metallopolymer as an iron source to try to overcome this limitation. The use of a polymer as an iron source can prevent the formation of particles due in part to the process of incipient wetness impregnation¹⁰¹⁻¹⁰⁴ and the thermodynamic properties of polymers which tend to form films on solid surfaces when in a solution.¹⁰⁵ This is a similar process to that of synthesis of mesoporous carbons which use a hard template such as the mesoporous silica SBA-15. A monomer is introduced into the template and forced to permeate the entirety of the mesoporous structure through incipient wetness impregnation: a phenomenon in which liquid is drawn into the high surface porosity of the template when the volume of the liquid is close to or equal to the total pore volume.¹⁰¹ Once the solution has permeated the porous template, the polymerization of the monomers is incited either by introduction of an initiator, catalyst or by raising the temperature, this is dependent on the type of monomer use. The polymerization of the solution ensures that the contents will remain trapped inside the template and adhere to the surface then a round of carbonization and acid washing with hydrofluoric acid to remove the silica template leaves behind a perfect negative of the original template.¹⁰⁴

In this case, we relied on the use of vinyl-ferrocene (vFe) as the iron source and used it in an organic solvent solution to permeate CTNC. Although current results have not yet produced a high enough half-wave potential to overcome the use of FeSO₄, the main Fe source used in the synthesis of CTNC-Fe, we have noticed that the iron mass activity of the best catalyst samples made with vFe as the source (CTNC-vFe) have a significantly higher value than those obtained

using FeSO₄ (CTNC-Fe). It is only due to the lower Fe content of CTNC-vFe that overall activity is yet slightly lower than CTNC-Fe, an issue that we intend to address in future work.

4.2 Experimental Section

4.2.1 Materials

Azobisisobutyronitrile (AIBN), dimethylsulfoxide (DMSO), dimethylformamide (DMF) CuBr₂, tris(2-pyridylmethyl)amine (TPMA), acrylonitrile (AN), bipyridine nitrate (BPN), n-butyl acrylate (BA), HCl, methanol, ultrapure water, FeSO₄·7H₂O, vinyl-ferrocene, 0.5 M sulfuric acid aqueous solution, Nafion 5 wt% solution and ultra-pure water were used. All materials were obtained from Millipore Sigma. CuBr₂ was purified by stirring in glacial acetic acid followed by washing with ether and dried overnight under vacuum. Monomers were passed through a basic alumina column prior to use.

4.2.2 Preparation of PAN-*b*-PBA copolymer

The copolymers were synthesized by initiator for continuous activator regeneration (ICAR) ATRP using the technique reported in Chapters 2 and 3. The final copolymer composition was PAN₁₀₃-*b*-PBA₆₀, confirmed using ¹N-NMR and GPC.

4.2.3 Preparation of CTNC-Fe and CTNC-vFe Catalysts

BCP was stabilized in air at 280 °C for one hour then it was ball-milled for 90 min. Then each was separately heat treated at 600 °C for 30 mins in 50 mL/min N₂ to produce carbonized CTNC. For the CTNC-Fe catalyst, 58.7 mg of the carbonized CTNC was mixed in 5 mL of ultra-pure water with 18.0 mg of FeSO₄·7H₂O and was stirred for 12 hours. The solution was then heated to 80 °C and stirred for an additional 2 hours until water fully evaporated. The dry mixture was further dried for 4 hours in air at 60 °C and then it was heat treated at 600°C for 0.5 hours in 50

mL/min N₂ flow. The resulting product was ground in an agate mortar for 10 mins then was mixed into a 0.5 M H₂SO₄ solution at 80 °C and was stirred for 2 hours. Afterward, it was extracted using a vacuum filter and then was thoroughly rinsed with ultra-pure water followed by being dried in 60°C air for 4 hours. Finally, the product was heat treated a third time in 100 mL/min N₂ flow at 900 °C for 3 hours to complete the CTNC-Fe catalyst.

Several solutions with different AIBN initiator concentrations and different vFe monomer concentrations were prepared inside an argon atmosphere to prevent the presence of water and oxygen, the initiator and monomer concentrations can be seen in Table 4.1.

Table 4.1. List of vFe monomer solutions prepared for experiment in CTNC-vFe synthesis.

Solution #	Monomer Concentration (wt%)	Initiator Concentration (wt%)
1	21.6	0.17
2	21.6	0.33
3	21.6	0.66
4	21.6	1.3
5	21.6	2.6
6	5.9	0.17
7	7.8	0.17
8	9.3	0.17
9	11.4	0.17
10	15.0	0.17
11	25.0	0.17
12	30.0	0.17
13	35.0	0.17
14	40.0	0.17

Table 4.2. List of different CTNC-vFe samples synthesized with different solutions, volumes, and Fe amounts.

Sample	Volume (μL)	Iron mass (mg)	Fe (wt%)	Solution #
RMT144	33.5	2.01	3.86%	1
RMT145	83.3	4.998	9.09%	1
RMT146	22	1.32	2.57%	1
RMT147	45	2.7	5.12%	1
RMT148	55	3.3	6.19%	1
RMT149	65	3.9	7.24%	1
RMT156	67.5	2.7	5.12%	10
RMT157	90	2.7	5.12%	9
RMT158	112.5	2.7	5.12%	8
RMT159	135	2.7	5.12%	7
RMT160	180	2.7	5.12%	6
RMT165	38	2.7	5.12%	11
RMT166	30.9	2.7	5.12%	12
RMT167	25.9	2.7	5.12%	13
RMT168	22.2	2.7	5.12%	14
RMT169	40	2.842	5.38%	11
RMT170	42	2.984	5.63%	11
RMT173	35	3.058	5.76%	12
RMT174	25	2.184	4.19%	12
RMT175	31	3.232	6.07%	13
RMT176	20	2.085	4.00%	13
RMT177	27	3.284	6.16%	14
RMT178	17	2.068	3.97%	14
RMT161	45	2.7	5.12%	2
RMT162	45	2.7	5.12%	3
RMT163	45	2.7	5.12%	4
RMT164	45	2.7	5.12%	5

PAN₁₀₃-*b*-PBA₆₀ BCP was dissolved in a 20 wt% solution in NMP at room temperature and was stirred for 2 hours. Then ultra-pure water was added to precipitate and separate the BCP from the NMP solution. The BCP was extracted using a vacuum assisted filter and was thoroughly washed with ultra-pure water then dried in air at 60 °C for 12 hours. The BCP was stabilized at

280 °C for 1 hour in 150 mL/min air flow then ballmilled for 1.5 hours. Finally, it was heat treated at 600 °C for 30 mins in 50 mL/min N₂. CTNC-vFe catalysts were synthesized by adding different vFe solution volumes as seen in Table 4.2, the solution was added inside an argon atmosphere and then the mixture was sealed to prevent the presence of oxygen. The mixture was heated to 65 °C to activate the initiator and start the free-radical polymerization of vFe, it was left at this temperature for 12 hours. The mixture was dried first in air then in vacuum at 60 °C then it was heat treated at 900 °C for 3 hours in 100 mL/min N₂.

4.2.4 Testing Electrochemical Activity

Measurements of electrochemical activity were captured using rotary disk electrode (RDE) potentiometry. An ink was prepared using 5 mg of catalyst with 40 μL of 5% Nafion solution in alcohol dissolved in 0.5 mL n-propanol. The ink was sonicated in an ice bath for 1 hour and an aliquot of 17 μL was casted onto the glassy carbon electrode for a 0.8 mg/cm² catalyst loading. A 0.5 M sulfuric acid solution at room temperature with a mercury/mercurous sulfate reference electrode and a graphite counter electrode was used. Cyclic voltammetry was implemented from 0 to 1 V (vs. NHE) in 50 mV/sec steps at 200 rpm in nitrogen flow and chronoamperometry scans were captured at 50 mV per 30 second steps at 900 rpm under oxygen flow.

4.2.5 Materials Characterization

The polymer solution monomer conversion rate was tested at different times during the polymerization process to ensure proper controlled/ “living” radical polymerization using proton nuclear magnetic resonance (¹H-NMR). Polymer molecular mass and distribution was tested using gel permeation chromatography (GPC) equipped with a Wyatt Optilab T-rEX refractive index (RI) detector, using DMF as the mobile phase. The nature of the bonding of heteroatoms in the carbon matrix was determined using X-ray photoelectron spectroscopy (XPS) and X-ray diffraction

(XRD) and the surface area and pore size were measured using Brunauer-Emmett-Teller (BET) surface area analysis. Powder samples were first degassed at 120 °C for at least 4 hours before N₂ sorption measurement. The micropores were analyzed using the t-plot method with the Halsey equation. The slope of the t-plot was used to calculate the external SSA, while the micropore surface area (S_{micro}) was obtained from subtracting S_{external} from S_{BET} . The mesoporous size distribution was obtained from Barrett-Joyner-Halenda (BJH) method from the adsorption branch with KJS correction. Finally, the presence of mesopores was tested using a JEOL JEM 2000EX transmission electron microscope (TEM).

4.3 Results and Discussion

4.3.1 Electrochemical Activity Results

Before performing the analysis of the effects of using vFe to Fe-dope an Fe-N-C catalyst we had to figure out how to best use free-radical polymerization in the porosity of CTNC. For this reason, we experimented with the concentration of AIBN initiator, the results can be seen in Figure 4.1. As can be seen in Fig. 4.1a, the smallest concentration of AIBN initiator produced the best electrochemical results. This went against our initial hypothesis that a higher concentration of initiator would be needed inside the mesoporous structure of CTNC since it was likely that some of the monomers may be trapped in an individual mesopore and with a low enough concentration of initiator then there would be limited or no polymerization of vFe at all. Perhaps this would have been the case at lower concentrations, however, we have not yet experimented on it.

Based on the results in Fig. 4.1, we performed the rest of the synthesis of CTNC-vFe samples using an AIBN initiator concentration of 0.16 wt%. Different CTNC-vFe samples were made with monomer solution concentration and Fe mass as the variables. The results can be seen

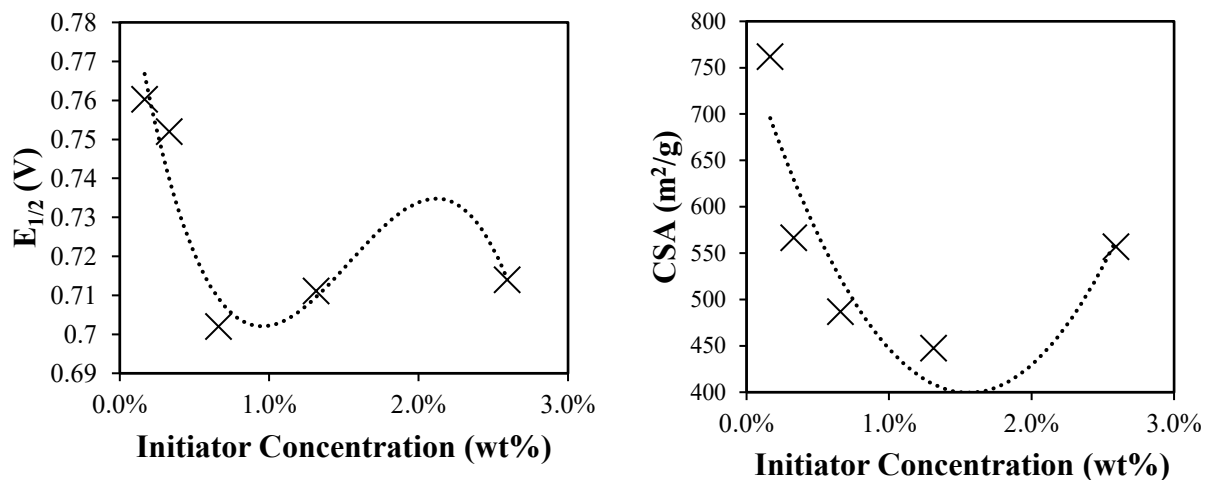


Figure 4.1. Summary RDE potentiometry results for CTNC-vFe samples with varied AIBN initiator concentrations. a) Half-wave potential results (V vs NHE) performed in 0.5 M H_2SO_4 solution under O_2 flow at 900 rpm b) Capacitive surface area results performed in 0.5 M H_2SO_4 solution under N_2 flow at 200 rpm.

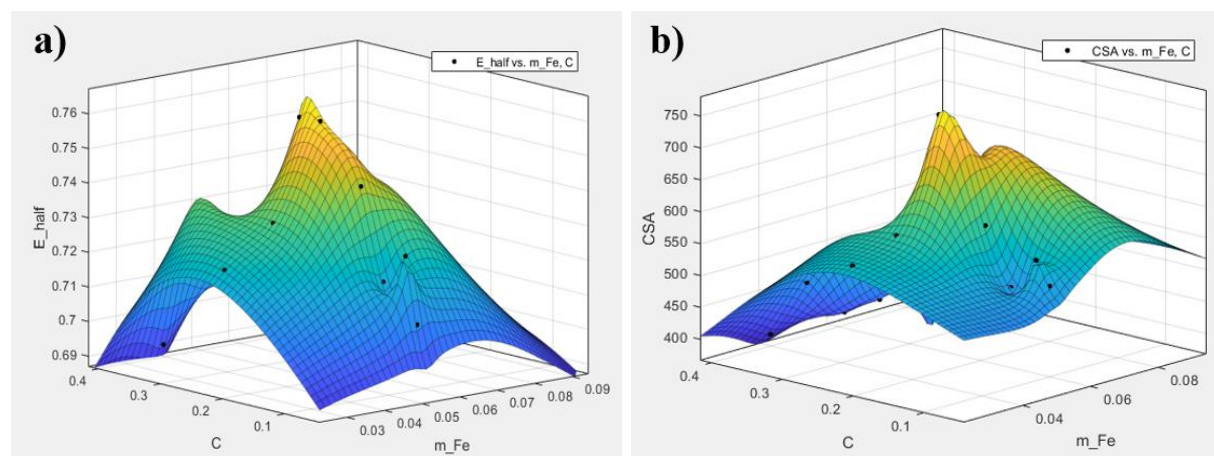


Figure 4.2. Summary RDE potentiometry results for CTNC-vFe samples with varied monomer concentration and Fe mass content a) Half-wave potential results (V vs NHE) performed in 0.5 M H_2SO_4 solution under O_2 flow at 900 rpm b) Capacitive surface area results performed in 0.5 M H_2SO_4 solution under N_2 flow at 200 rpm.

in Fig. 4.2 which presents both half-wave potential and capacitive surface area as a dependent variable of monomer solution concentration and Fe mass content. The Fe mass content represents the total amount added to the Fe mixture during synthesis not the actual final Fe mass content of the CTNC-vFe catalyst.

Based on the results seen in Fig. 4.2, the best performing CTNC-vFe catalyst sample was synthesized with solution 11 which contains 25% monomer concentration and 0.16 wt% AIBN initiator concentration. Its half-wave potential was 0.761 V vs NHE and its capacitive surface was 542.7 m²/g. Furthermore, the total Fe content added during synthesis was 5.12 wt% which is a lot lower than the Fe content of 16.7 wt% added when using FeSO₄ as the Fe-dopant. However, when comparing the overall electrochemical activity of CTNC-Fe and CTNC-vFe, as seen in Fig. 4.3 the CTNC-Fe sample still has a higher ORR electrochemical activity of 0.778 V vs NHE half-wave potential and a capacitive surface area of 638.1 m²/g.

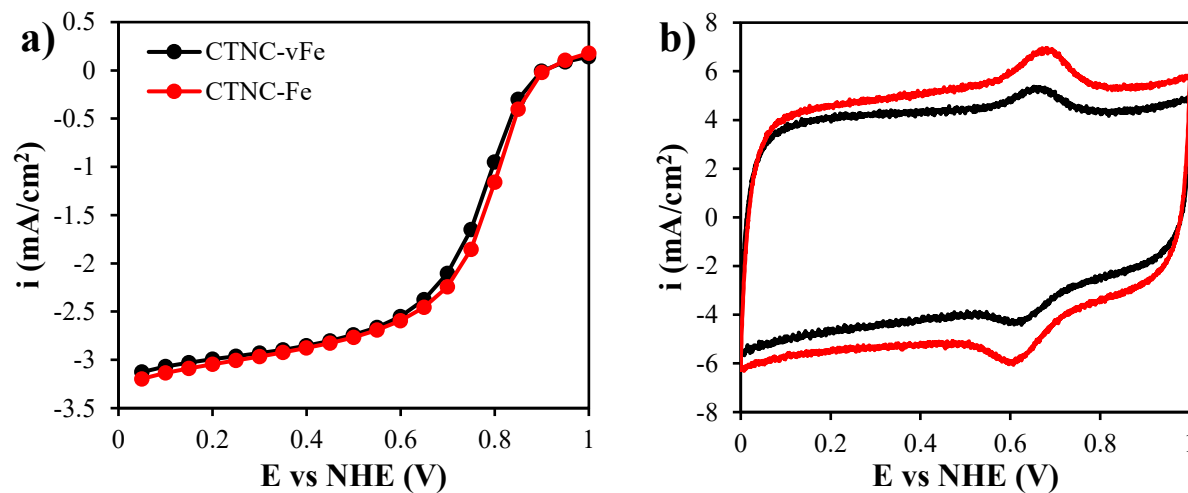


Figure 4.3. Comparison of RDE potentiometry results for CTNC-vFe and CTNC-Fe. a) Half-wave potential obtained in 0.5 M H₂SO₄ solution in O₂ flow at 900 rpm. b) Capacitive surface area obtained in 0.5 M H₂SO₄ solution in N₂ flow at 200 rpm.

4.3.2 Chemical Composition Analysis

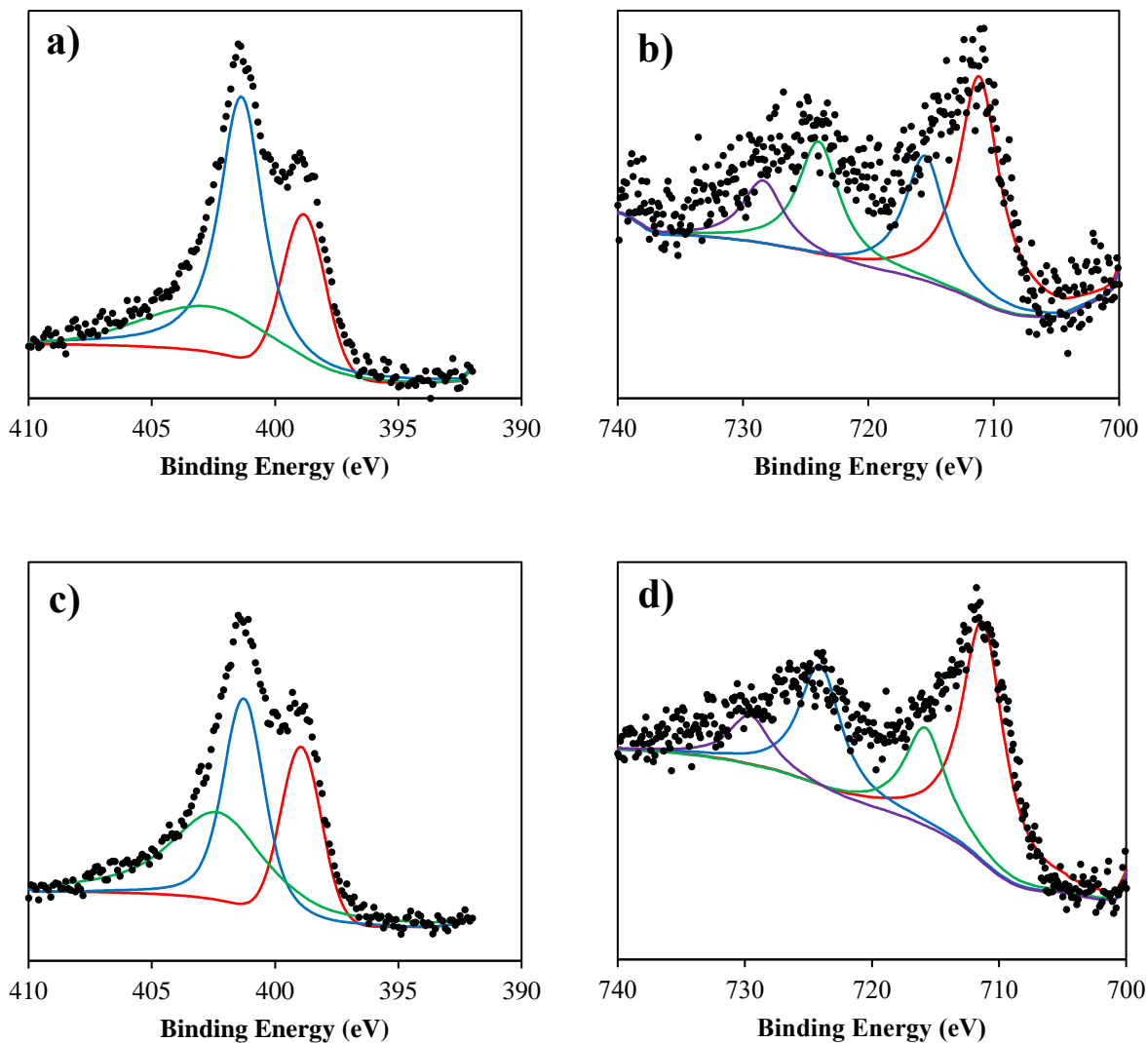


Figure 4.4. XPS high resolution spectra of CTNC-vFe and CTNC-Fe catalysts. a) CTNC-vFe N 1s spectrum, b) CTNC-vFe Fe 2p spectrum, c) CTNC-Fe N 1s spectrum, and d) CTNC-Fe Fe 2p spectrum.

As seen in Fig. 4.4, the nitrogen content is similar as expected since both catalyst samples used the same BCP (PAN_{103} - b - PBA_{60}). The deconvoluted peaks of nitrogen are at similar binding energies of 398.9 eV, 401.2 eV which represent pyridinic N, pyrrolic/graphitic N and Fe-N moieties. CTNC-vFe, however, has a higher content of pyrrolic/graphitic N, according to Table

4.3, so it is likely that Fe-N active sites are more likely to be associated with pyrrolic/graphitic N than pyridinic N. Furthermore, the N-O content of CTNC-vFe is half that of CTNC-Fe. The likely cause for this may be the use of vacuum drying during synthesis, therefore, it may be possible to increase the availability of nitrogen moieties for formation of Fe-N sites by vacuum drying.

In the case of Fe content, CTNC-vFe seems to have a lower content than CTNC-Fe as expected. However, thermogravimetric analysis revealed an Fe content of 9.16 wt% for CTNC-vFe and 4.62 wt% for CTNC. This probably means that the majority of the Fe content in CTNC-vFe is trapped inside the mesopores where XPS cannot detect. Unfortunately, this also means that some of the iron is not accessible for electrochemical activity and is the reason why the half-wave potential and CSA of CTNC-vFe is lower than that of CTNC-Fe. If we are going to be able to have full use of that iron then we will probably have to apply some surface activation process to CTNC.

Table 4.3. Surface elemental composition of CTNC-vFe and CTNC-Fe catalysts obtained using XPS.

Catalyst Sample	Sulfur (%)	C Graphitic (%)	C Amorphous (%)	Pyridinic N/Fe-N (%)	Pyrrolic / Graphitic N (%)	Oxygen (%)	Iron (%)	N-O (%)
CTNC-vFe	0.114	52.724	35.696	1.895	3.160	5.720	0.375	0.316
CTNC-Fe	0.262	52.233	36.083	2.041	2.387	5.727	0.649	0.620

4.3.3 Morphology and Porosity

The results for BET surface area analysis can be seen on Table 4.4, as can be seen, the surface area of CTNC-vFe is significantly lower than that of CTNC-Fe. Furthermore, the mesopore surface area of CTNC-vFe is especially lower, this suggests that the doping method of using poly(vinyl-ferrocene) was indeed successful in permeating the mesoporous surface of CTNC-vFe.

However, as the micropore surface area is also lower than that of CTNC-Fe, there is less access to the mesoporous phase of the catalyst.

Table 4.4. BET surface area analysis results for CTNC-vFe and CTNC-Fe catalysts.

Sample	BET Surface Area (m ² /g)	Total Pore Volume (cm ³ /g)	Mesopore (m ² /g)	Micropore (m ² /g)	Average Pore size (nm)
CTNC-vFe	348.1	0.566	213.3	134.8	9.2
CTNC-Fe	430.4	0.651	272.7	157.7	8.3

The pore morphology, seen in Fig. 4.5 also shows a significant difference between both catalyst types. The morphology of CTNC-vFe, seen in Fig. 4.5a, seems less uniform than that of CTNC-Fe which agrees with the results gleaned from the BET surface area analysis and the capacitive surface area.

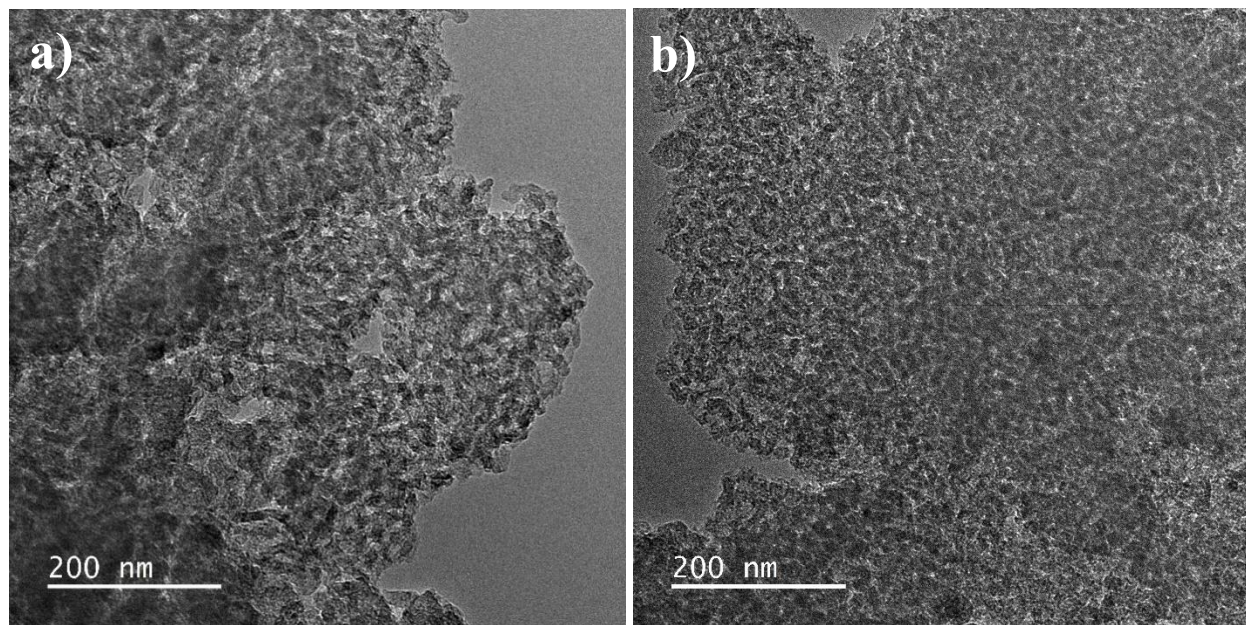


Figure 4.5. TEM images of a) CTNC-vFe and b) CTNC-Fe.

4.4 Conclusions and Future Work

We have developed a novel method of Fe-doping by the use of free radical polymerization of a metallopolymer to enhance permeation of Fe atoms into the mesoporous structure and to use the polymer to prevent metallic Fe aggregates by spreading the Fe source thanks to the properties of polymers to form thin films. We did this to improve on the density of active sites, increase iron mass activity and remove the need of acid washing which can have negative effects on the structure of the carbon. However, as shown by the electrochemical activity, elemental composition and BET surface area the results were exceeded by our previous synthesis method which uses FeSO_4 as an iron source and acid washing.

Nevertheless, there are still plenty other methods to improve this new Fe-doping process. Perhaps to incrementally add Fe atoms into the CTNC by successive vFe injections: this would need a quick heat treatment at $600\text{ }^\circ\text{C}$ for 30 minutes in between injections. As we have found, the process is actually able to permeate into the mesopores. These mesopores were perhaps blocked because we used too high a concentration of monomer solution, consequently, the multiple injections would need to be done with a much lower concentration. Every pass would add more iron but in a incrementally slow way that will not block pores and will slowly consume the nitrogen content present on the CTNC surface.

In addition, as was detected by BET surface area analysis the micropore surface area of CTNC-vFe was very low. Perhaps using a controlled method of surface activation such as ZnCl_2 may alleviate the issue. On the other hand, we used this method on CTNC produced from PAN₁₀₃-b-PBA₆₀, there is a possibility that this process may be more successful on a CTNC with a different pore size or morphology. This experiment is relatively new compared to the use of FeSO_4 and

there is still much more experimentation that can be performed before giving up on it. It is just another example of the trial and error nature of research in PGM-free catalysts.

Chapter 5: The Effects of Pore Morphology on CTNC-Fe Catalyst Electrochemical Performance

5.1 Introduction

Previously we had continued to experiment with a single BCP, namely PAN₁₀₃-b-PBA₆₀. This was due to the need of finding a reliable method to convert CTNC into a working Fe-N-C catalyst. Then, after reaching a half-wave potential of 0.781 V vs NHE there was a plateau in improvement of the electrochemical activity. It seems that is the limit of activity that can be achieved with this specific form of PAN-PBA BCP as a base for a PGM-free catalyst without adding any other nitrogen sources or using a surface activation process. However, one of the main reasons for experimentation with CTNC has been since the nanostructure can be controlled and tuned by use of controlled/ “living” radical polymerization which can control the length of the polymer blocks.

Several works have found that the formation of electrochemical active sites is not only due to the presence of nitrogen and iron species to form the most electrochemically active FeN_x sites and high surface area but also the structure of the porous carbon itself.⁴⁵⁻⁴⁹ It has been theorized that micropores of a certain size range are most likely to maximize the formation of active sites, however,⁴⁶ it is generally agreed that mesoporous structures are the best bases since they have the highest surface areas.⁸⁻¹⁶ Therefore, it comes to a balance between the mesopores and the micropores of the catalyst as well as the morphology of the nanostructure. This is especially true

for CTNC because not only is there a need for thorough access to pores during the Fe-doping process but also the migration of nitrogen heteroatoms to the pore surface.

Penetration of precursors into the porous structure during the Fe-doping process can be favorably affected by specific pore size distributions.¹⁰⁶ Furthermore, this access is especially important for ORR since thorough accessibility of porosity decreases mass transport overpotential.^{46,106} On the other hand, the movement of nitrogen heteroatoms in the CTNC carbon matrix also needs to be taken into consideration, especially when not using any other nitrogen precursor during synthesis. Although the migration of the N atoms is energetically favorable along the surface of graphene sheets,^{107,108} the presence of vacancies between adjacent sheets in graphite make orthogonal movement possible.¹⁰⁸ Furthermore, N atoms can occupy bridges between graphene sheets which makes intercalation much more likely.¹⁰⁸ Therefore, N atoms are able to move in all three dimensions in CTNC unobstructed at high temperatures due to the presence of a high number of vacancies in amorphous carbon. So, a morphology that can favorably conduct N atoms to the pore surface during synthesis would be ideal.

This is a significant point that can be addressed by CTNC for which the microporous and mesoporous structure can be controlled by the variation of the lengths of the polymer blocks of the BCP. In this chapter, we describe the effects of the variation of CTNC pore morphology by the composition of block copolymer.

5.2 Experimental Section

5.2.1 Materials

Azobisisobutyronitrile (AIBN), dimethylsulfoxide (DMSO), dimethylformamide (DMF) CuBr_2 , tris(2-pyridylmethyl)amine (TPMA), acrylonitrile (AN), bipyridine nitrate (BPN), n-butyl acrylate (BA), HCl, methanol, ultrapure water, $\text{FeSO}_4 \cdot 7\text{H}_2\text{O}$, 0.5 M sulfuric acid aqueous solution,

Nafion 5 wt% solution and ultra-pure water were used. All materials were obtained from Millipore Sigma. CuBr_2 was purified by stirring in glacial acetic acid followed by washing with ether and dried overnight under vacuum. Monomers were passed through a basic alumina column prior to use.

5.2.2 Preparation of PAN-*b*-PBA copolymers

The copolymers were synthesized by initiator for continuous activator regeneration (ICAR) ATRP using the technique reported in Chapters 2 and 3. In this case, however, the polymerization was terminated at various times as calculated by measuring the rate of polymerization using ^1H nuclear magnetic resonance. According to the measurements the final four copolymer compositions were the following: $\text{PAN}_{60}\text{-}b\text{-PBA}_{37}$, $\text{PAN}_{76}\text{-}b\text{-PBA}_{47}$, $\text{PAN}_{103}\text{-}b\text{-PBA}_{60}$, and $\text{PAN}_{165}\text{-}b\text{-PBA}_{99}$.

5.2.3 Preparation of CTNC-Fe Catalysts

Each BCP was stabilized in air at 280 °C for one hour then it was ball-milled for 90 min. Then each was separately heat treated at 600 °C for 30 mins in 50 mL/min N_2 to produce carbonized CTNC. For each of the catalysts, 58.7 mg of the carbonized CTNC was mixed in 5 mL of ultra-pure water with 18.0 mg of $\text{FeSO}_4 \cdot 7\text{H}_2\text{O}$ and was stirred for 12 hours. The solution was then heated to 80 °C and stirred for an additional 2 hours until water fully evaporated. The dry mixture was further dried for 4 hours in air at 60 °C and then it was heat treated at 600°C for 0.5 hours in 50 mL/min N_2 flow. The resulting product was ground in an agate mortar for 10 mins then was mixed into a 0.5 M H_2SO_4 solution at 80 °C and was stirred for 2 hours. Afterward, it was extracted using a vacuum filter and then was thoroughly rinsed with ultra-pure water followed by being dried in 60°C air for 4 hours. Finally, the product was heat treated a third time in 100 mL/min N_2 flow at 900 °C for 3 hours to complete the CTNC-Fe catalyst. Pristine CTNC for each

BCP was made from stabilized BCP heat treated at 600 °C for 30 minutes and then at 900 °C for 3 hours under nitrogen flow.

5.2.4 Testing Electrochemical Activity

Measurements of electrochemical activity were captured using rotary disk electrode (RDE) potentiometry. An ink was prepared using 5 mg of catalyst with 40 μL of 5% Nafion solution in alcohol dissolved in 0.5 mL n-propanol. The ink was sonicated in an ice bath for 1 hour and an aliquot of 17 μL was casted onto the glassy carbon electrode for a 0.8 mg/cm^2 catalyst loading. A 0.5 M sulfuric acid solution at room temperature with a mercury/mercurous sulfate reference electrode and a graphite counter electrode was used. Cyclic voltammetry was implemented from 0 to 1 V (vs. NHE) in 50 mV/sec steps at 200 rpm in nitrogen flow and chronoamperometry scans were captured at 50 mV per 30 second steps at 900 rpm under oxygen flow.

5.2.5 Materials Characterization

The polymer solution monomer conversion rate was tested at different times during the polymerization process to ensure proper controlled/ “living” radical polymerization using proton nuclear magnetic resonance ($^1\text{H-NMR}$). Polymer molecular mass and distribution was tested using gel permeation chromatography (GPC) equipped with a Wyatt Optilab T-rEX refractive index (RI) detector, using DMF as the mobile phase. The nature of the bonding of heteroatoms in the carbon matrix was determined using X-ray photoelectron spectroscopy (XPS) and X-ray diffraction (XRD) and the surface area and pore size were measured using Brunauer-Emmett-Teller (BET) surface area analysis. Powder samples were first degassed at 120 °C for at least 4 hours before N_2 sorption measurement. The micropores were analyzed using the t-plot method with the Halsey equation. The slope of the t-plot was used to calculate the external SSA, while the micropore surface area (S_{micro}) was obtained from subtracting S_{external} from S_{BET} . The mesoporous size

distribution was obtained from Barrett-Joyner-Halenda (BJH) method from the adsorption branch with KJS correction. Finally, the presence of mesopores was tested using a JEOL JEM 2000EX transmission electron microscope (TEM).

5.3 Results and Discussion

5.3.1 Electrochemical Activity

According to the results obtained using RDE potentiometry (Fig. 5.1) the catalyst with the highest ORR electrochemical activity was the one obtained from using PAN_{76-b}-PBA₄₇ as a base. Its electrochemical activity reached a value of 0.8 V vs NHE whereas the lowest one, PAN_{60-b}-PBA₃₇, got a value of only 0.72 V vs NHE (Table 5.1).

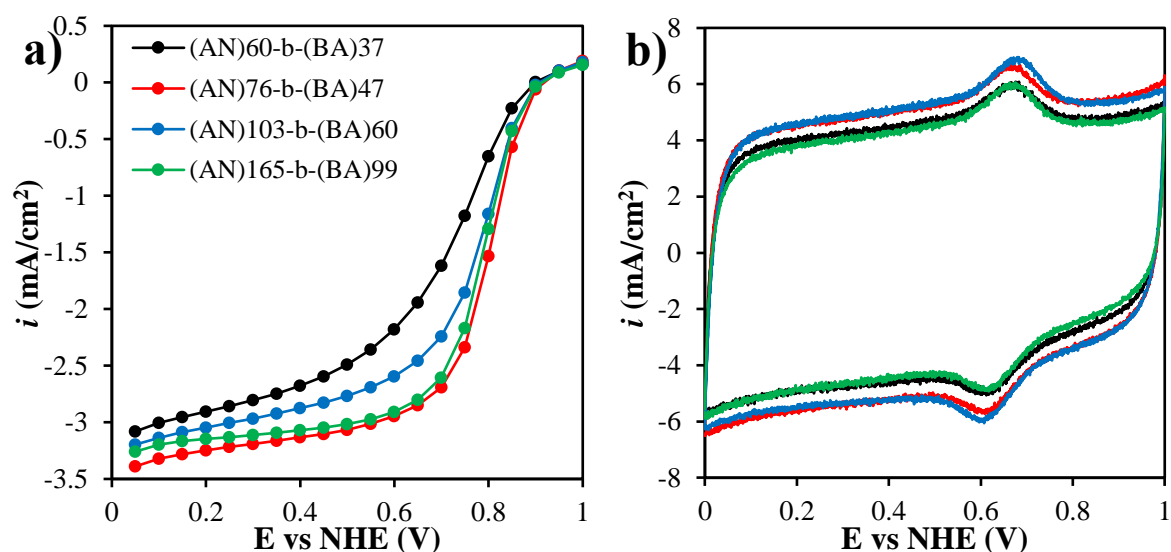


Figure 5.1. Electrochemical activity results on ORR of CTNC-Fe catalysts made with different BCP compositions. a) Polarization curve of ORR in acidic environment obtained using chronoamperometry scans in oxygen saturated 0.5 M H₂SO₄ solution at room temperature. b) Cyclic voltammetry curve obtained in nitrogen saturated 0.5 M H₂SO₄ solution at room temperature.

Table 5.1. RDE potentiometry results for the CTNC-Fe catalysts synthesized using different BCP compositions.

BCP Composition	E_{1/2} (V vs NHE)	CSA (m²/g)	A_{mass} (A/g)
PAN ₆₀ - <i>b</i> -PBA ₃₇	0.72	563.5	0.32
PAN ₇₆ - <i>b</i> -PBA ₄₇	0.80	641.9	0.798
PAN ₁₀₃ - <i>b</i> -PBA ₆₀	0.78	638.1	0.565
PAN ₁₆₅ - <i>b</i> -PBA ₉₉	0.79	550.5	0.6

As seen in Fig. 5.1a, the four samples tested have a similar limiting current value between 3 and 3.5 mA/cm² which means a good base for comparison between samples since it shows that it is unlikely that mass loading or any other issues are skewing results. Furthermore, the variation in CSA is not significant and does not appear to be a pattern for qualifying the quality of each sample. Based on this, it is likely that surface area is not a factor in the determination of electrochemical activity.

5.3.2 Catalyst Porosity and Morphology

Table 5.2. BET surface area analysis results for pristine CTNCs and CTNC-Fe catalysts.

BCP Composition	BET Surface Area (m²/g)	Micropore (m²/g)	Mesopore (m²/g)	Average Pore size (nm)	Peak Pore Size (nm)	Pore Volume (cm³/g)
(AN)60- <i>b</i> -(BA)37 - Fe	347.9	114.6	233.4	5.7	5.9	0.38
(AN)60- <i>b</i> -(BA)37	464.1	232.4	231.7	5.2	6.6	0.38
(AN)76- <i>b</i> -(BA)47 - Fe	370.6	121.6	248.9	7.8	11.6	0.59
(AN)76- <i>b</i> -(BA)47	379.7	132.8	246.9	7.8	9.3	0.57
(AN)103- <i>b</i> -(BA)60 - Fe	430.4	157.7	272.7	8.3	11.5	0.66
(AN)103- <i>b</i> -(BA)60	528.6	276.4	252.1	8.7	11.5	0.68
(AN)165- <i>b</i> -(BA)99 - Fe	322.4	105.1	217.4	11.5	19	0.72
(AN)165- <i>b</i> -(BA)99	417.6	209.7	207.9	10.4	19	0.67

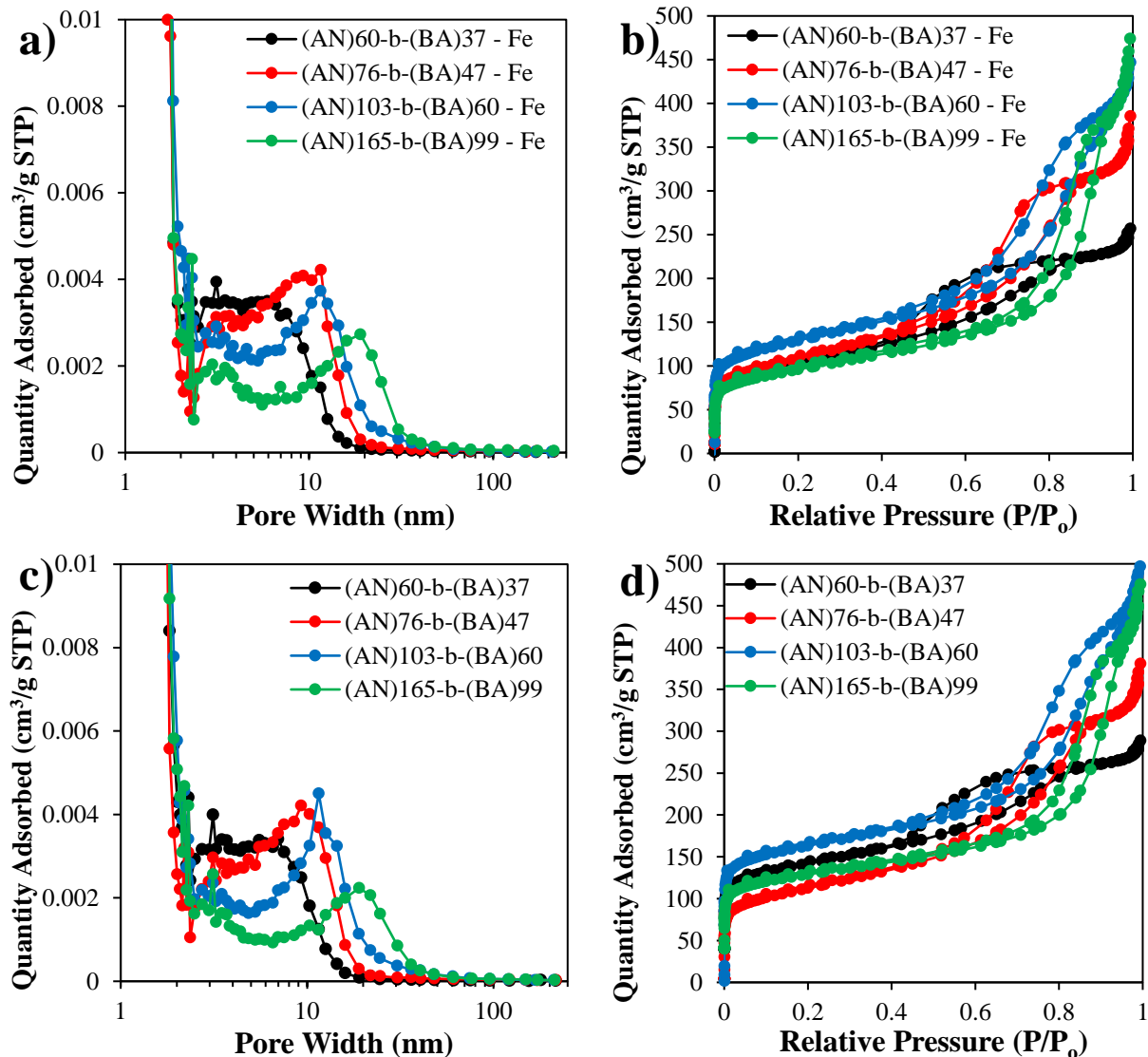


Figure 5.2. BET surface area analysis results for pristine CTNC and CTNC-Fe catalysts. a) Pore width distribution for CTNC-Fe catalysts, b) adsorption-desorption isotherms for CTNC-Fe catalysts, c) Pore width distribution for pristine CTNCs, and d) adsorption-desorption isotherms for pristine CTNCs.

The results obtained from BET surface area analysis showed that despite all the processes involved in Fe-doping for turning CTNC into a CTNC-Fe catalyst, the overall carbon structure was maintained as shown in Fig. 5.2. All the CTNC-Fe catalysts show similar mesopore surface area values to that of their respective pristine CTNC, however, this is not reflected in the micropore

surface area values. Only CTNC-Fe catalyst synthesized from PAN₇₆-*b*-PBA₄₇ shows a similar micropore surface area value to that of its matching pristine CTNC. Perhaps this is the reason why this CTNC-Fe catalyst showed the highest half-wave potential and mass activity since the pattern is not reflected in any of the overall values as shown in Fig. 5.3.

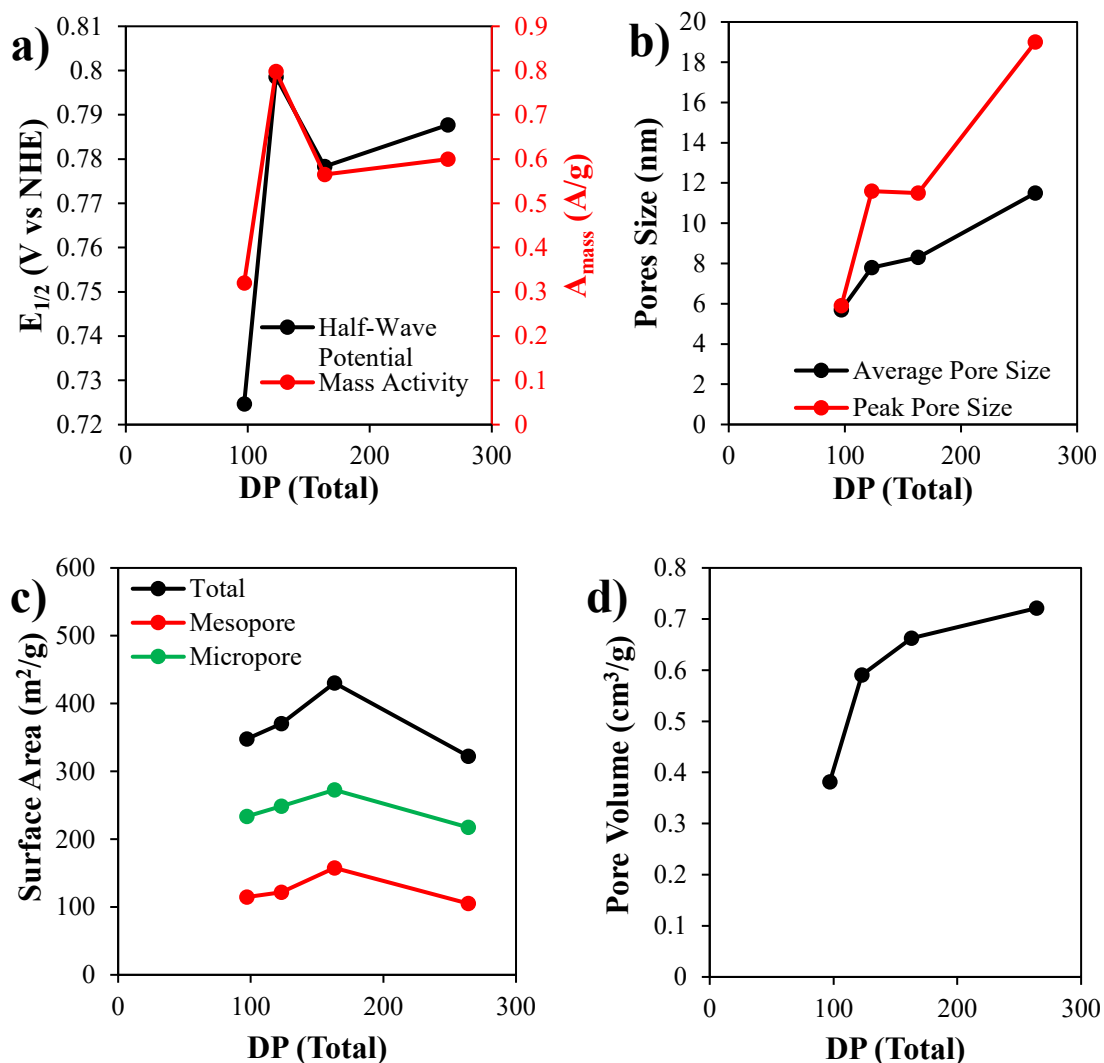


Figure 5.3. Performance and BET results comparison for CTNC-Fe catalysts synthesized using different BCP degrees of polymerization (DP). a) Electrochemical activity, b) Peak and average pore sizes, c) Total, mesopore and micropore surface area values, and d) Total pore volumes.

Fig. 5.3 shows that although PAN₇₆-*b*-PBA₄₇ produced the best results in electrochemical activity, it is PAN₁₆₅-*b*-PBA₉₉ which produces the greatest pore sizes and total pore volumes and PAN₁₀₃-*b*-PBA₆₀ produces the greatest total, mesopore and micropore surface areas. According to these results, it is unlikely that any of these factors by themselves have a significant effect on how the catalyst will turn out. There is probably a more complex relationship between the pore morphology and the electrochemical results.

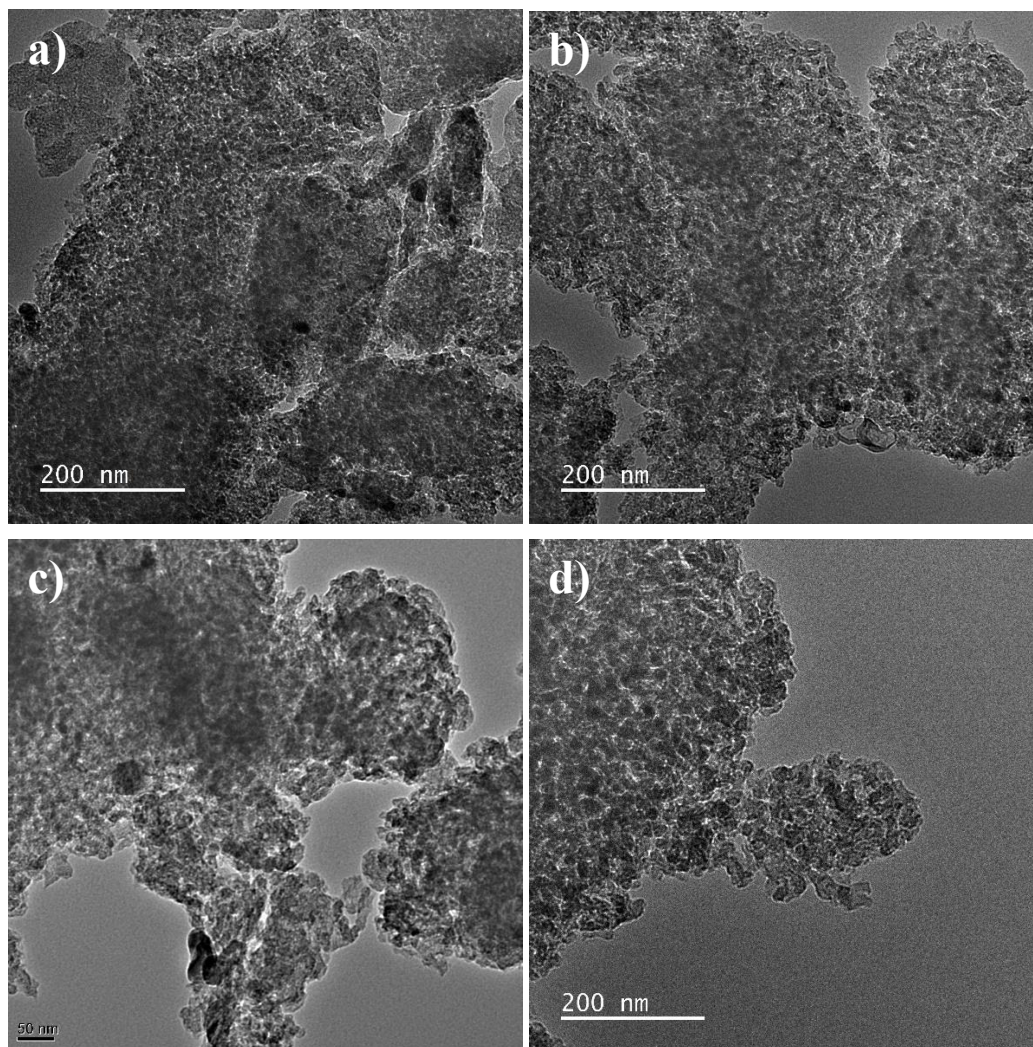


Figure 5.4. TEM images of the pore morphology of CTNC-Fe catalysts synthesized from different BCP compositions. a) PAN₆₀-*b*-PBA₃₇, b) PAN₇₆-*b*-PBA₄₇, c) PAN₁₀₃-*b*-PBA₆₀ and d) PAN₁₆₅-*b*-PBA₉₉.

Fig. 5.4 shows the morphology of each of the catalysts obtained using TEM. The morphology of PAN₇₆-*b*-PBA₄₇ does indeed show a great deal of connectivity between the largest and smallest pores which make it likely that this is the reason for it having the best performance, however, both PAN₁₀₃-*b*-PBA₆₀ and PAN₁₆₅-*b*-PBA₉₉ also show this aspect. Therefore, the results are likely due to the specific formation of active sites being aided by the overall morphology of the porous structure and not any singular factor such as having the greatest pore volume or surface area.

5.3.3 Elemental Composition of CTNC-Fe Catalysts

While the overall elemental composition does not seem to be completely different amongst the different CTNC-Fe catalysts, the two best samples (CTNC-Fe catalysts made with PAN₇₆-*b*-PBA₄₇ and PAN₁₆₅-*b*-PBA₉₉) show a significantly lower pyridinic and oxidized N content compared to the other samples as shown in Table 5.3. PAN₇₆-*b*-PBA₄₇ also shows the lowest Fe content, at least that detected by XPS. It is when looking at the graphitic carbon and oxygen content where we see a significant difference between the best sample and the rest. PAN₇₆-*b*-PBA₄₇ has approximately over 10% higher graphitic content than the average amongst all the samples. It is possible that this higher graphitic carbon content gives the CTNC-Fe catalyst a significantly greater electrical conductivity than all the others which would indeed be a source of higher electrochemical activity.

Table 5.3. CTNC-Fe surface elemental composition according to 200 eV scan using XPS.

BCP Composition	Graphitic C (at%)	Amorphous C (at%)	Pyridinic N (at%)	Graphitic /Pyrrolic N (at%)	Oxygen (at%)	Fe (at%)	N-O (at%)
(AN)60-(BA)37	54.33	33.54	1.23	3.35	6.21	0.68	0.67
(AN)76-(BA)47	61.14	26.58	1.13	2.01	7.63	0.46	1.05
(AN)103-(BA)60	52.23	36.08	2.04	2.39	5.73	0.65	0.62
(AN)165-(BA)99	55.83	33.24	1.04	2.54	5.91	0.53	0.92

Furthermore, its oxygen content is also the maximum value amongst CTNC-Fe catalysts with a value 20% higher than the average. Although oxygen content is unlikely to affect the electrochemical activity directly, perhaps its presence produces a negatively charged effect on the surface of the catalyst which would cause a greater affinity to attracting H^+ ions from the electrolyte, thereby increasing proton transfer rate in ORR.

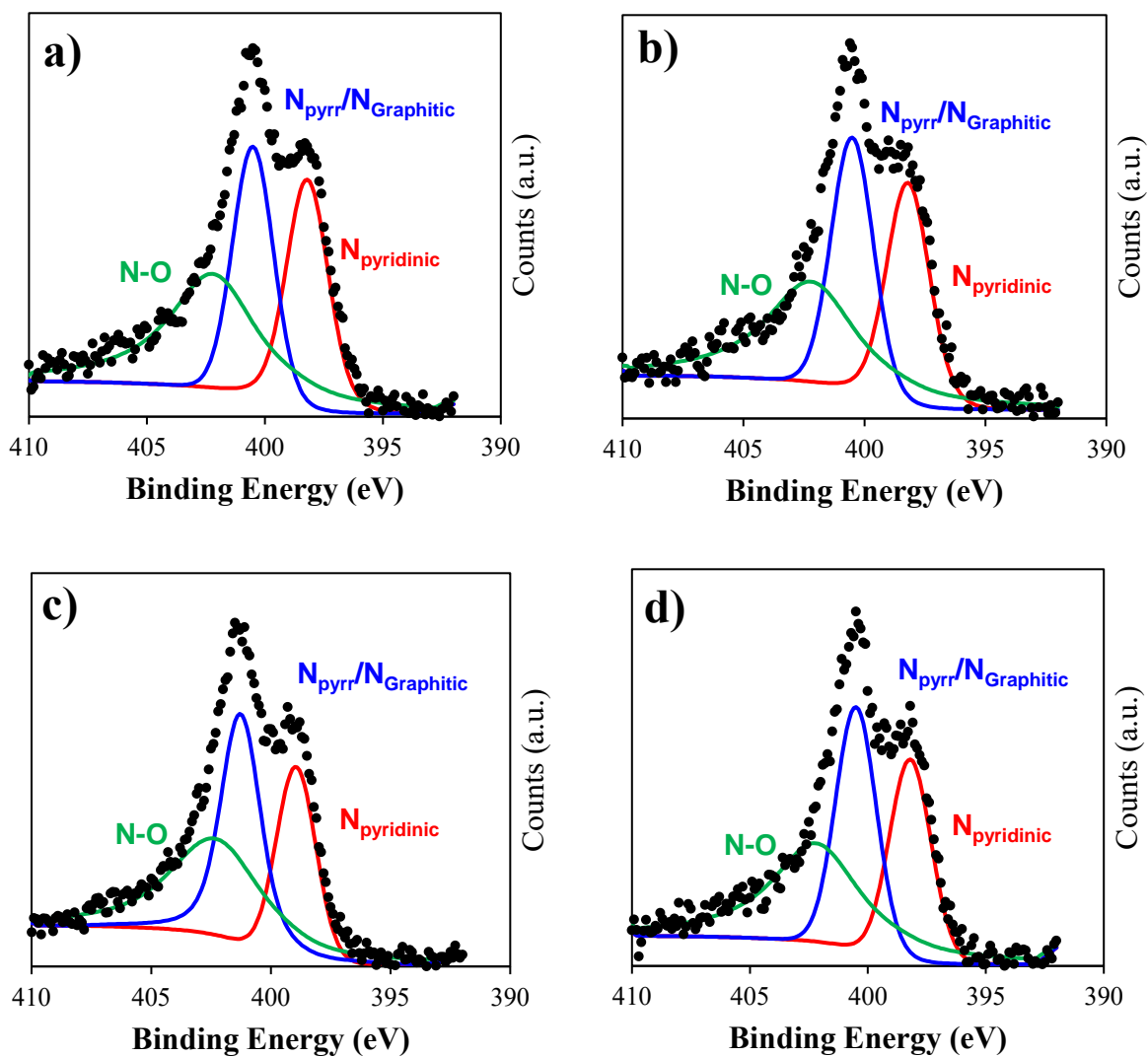


Figure 5.5. High resolution N 1s XPS spectra for CTNC-Fe catalysts. a) PAN₆₀-*b*-PBA₃₇, b) PAN₇₆-*b*-PBA₄₇, c) PAN₁₀₃-*b*-PBA₆₀ and d) PAN₁₆₅-*b*-PBA₉₉.

The N 1s XPS spectra showed no significant difference in binding energy, in fact most of the samples showed the same energy. PAN₁₀₃-*b*-PBA₆₀ had slightly higher energies for all three deconvoluted peaks, however, this sample was measured separately to the other three, so it was likely an issue with the XPS instrument. This was confirmed by taking the difference between the pyridinic and pyrrolic/graphitic peaks which resulted in a value of 2.3 eV for all samples.

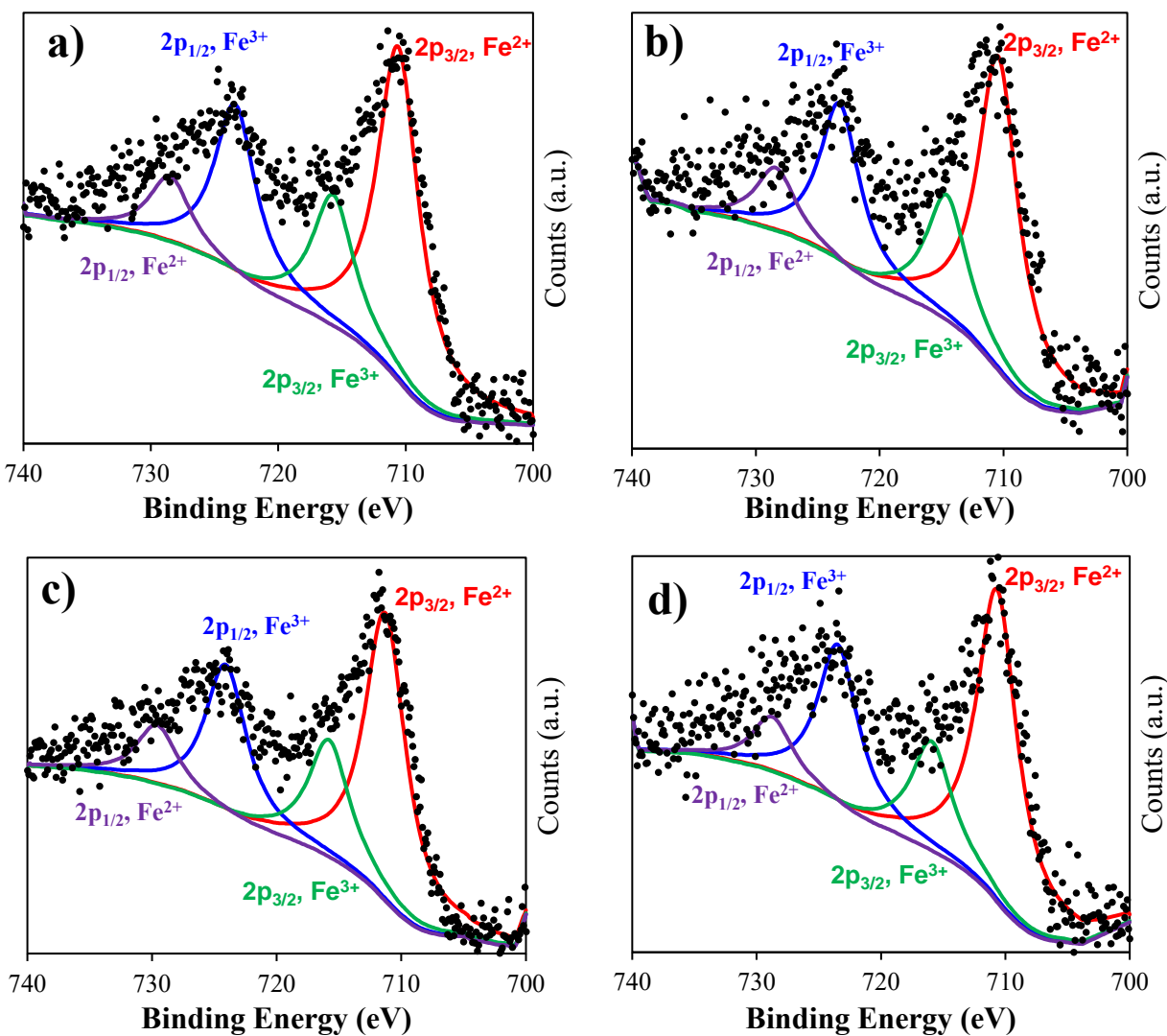


Figure 5.6. High resolution Fe 2p XPS spectra for CTNC-Fe catalysts. a) PAN₆₀-*b*-PBA₃₇, b) PAN₇₆-*b*-PBA₄₇, c) PAN₁₀₃-*b*-PBA₆₀ and d) PAN₁₆₅-*b*-PBA₉₉.

As seen in Fig. 5.6, it is Fe 2p spectra which shows the greatest difference between all four CTNC-Fe catalyst types. Because it is not so easy to see the deconvoluted peak binding energies, they are included in Table 5.4. PAN_{76-b}-PBA₄₇ showed the lowest energy of all CTNC-Fe catalysts' iron moieties which could possibly mean that the stability of the active sites for this catalyst is the best compared to the other CTNC-Fe samples. Additionally, the energy difference between the 2p_{3/2} peak and its satellite peak is the lowest energy difference meaning that cycling between Fe²⁺ and Fe³⁺ for the most active and most prevalent Fe moiety has the smallest energy barrier. According to the ORR reaction pathway, the first step in oxygen reduction is the binding of O₂ by an active site.⁶¹ Whether by chemisorption of the O₂ molecule or by actual formation of a bond between the active site it is unclear. What is clear, however, is that O₂ is very electronegative and formation of super oxide (O₂⁻) is not unusual in ORR, especially in enzymes such as cytochrome c oxidase which also use an Fe ion as an active site.²² Therefore, this smaller energy barrier present in CTNC-Fe synthesized using PAN_{76-b}-PBA₄₇ as a base is a likely explanation of why this catalyst produces the best electrochemical activity. The iron content itself, seen in Table 5.5 does not exactly explain the trend in electrochemical activity either. Although it does provide the measure of iron mass activity as follows: 4.267 A/g for PAN_{60-b}-PBA₃₇, 14.934 A/g for PAN_{76-b}-PBA₄₇, 12.092 A/g for PAN_{103-b}-PBA₆₀ and 7.51 A/g for PAN_{165-b}-PBA₉₉. This again proves that PAN_{76-b}-PBA₄₇ produced the best catalyst, however, to explain the reason for this more exacting elemental composition analysis could shed more light on the reason.

Table 5.4. Binding energy values for deconvoluted peaks of Fe 2p XPS spectra.

BCP Composition	2p _{3/2} , Fe ²⁺ (eV)	2p _{1/2} , Fe ³⁺ (eV)	2p _{3/2} , Fe ³⁺ (eV)	2p _{1/2} , Fe ²⁺ (eV)	Fe ²⁺ to Fe ³⁺ (eV)	Fe ³⁺ to Fe ²⁺ (eV)
(AN)60-(BA)37	710.7	723.5	715.8	728.6	5.1	5.1
(AN)76-(BA)47	710.5	723.4	714.7	728.5	4.2	5.1
(AN)103-(BA)60	711.4	724.2	715.9	729.7	4.5	5.5
(AN)165-(BA)99	710.8	723.6	716.1	728.9	5.3	5.3

Table 5.5. Fe content of CTNC-Fe catalysts made from different BCP compositions obtained from TGA.

BCP Composition	Fe ₂ O ₃ residue wt%	Fe wt%
(AN)60-(BA)37	10.6	7.39
(AN)76-(BA)47	7.5	5.27
(AN)103-(BA)60	6.6	4.61
(AN)165-(BA)99	11.3	7.88

5.4 Conclusion

We have been able to develop a CTNC-Fe catalyst and have shown that we can improve the results by controlling the nanostructure of the carbon through tuning the block copolymer composition and degree of polymerization. Although we initially hypothesized that the larger the pore size the better the electrochemical activity, this was disproved by the results for PAN₇₆-*b*-PBA₄₇ which though having the second smallest pore size from the four tested block copolymers, it produced the best electrochemical activity in its resultant CTNC-Fe catalyst. Analysis of the microstructure showed no significant pattern in the cause for these results; pore size, surface area and pore volume were not factors upon which the electrochemical activity of the catalyst was significantly dependent, at least not by themselves. The most likely explanation is that there is a more complex relationship between the pore morphology of the carbon and the resulting electrochemical activity. This was evident by analysis of the Fe 2p spectra which showed that the main Fe moiety identity which is often attributed to have the most positive effect on electrochemical activity on Fe-N-C catalysts, that is Fe²⁺ 2p_{3/2}, had the smallest energy barrier between its ground state and its high energy state. This suggests a lesser energy barrier to bind and

react with oxygen molecules, making ORR activation overpotential lower and causing a greater affinity for its catalysis. Overall composition also suggests that the graphitic phase of the CTNC-Fe synthesized using PAN₇₆-*b*-PBA₄₇ was significantly greater than that of the other catalysts.

From the fact that all the catalysts were synthesized using the same Fe-doping process and handled the exact same way, it can be concluded that most if not all the results recorded in this chapter can be attributed to the differences caused by the composition and degree of polymerization of each block copolymer tested. It is evident that this control can significantly influence electrochemical activity of CTNC-Fe therefore future work needs to focus on optimizing the Fe-doping process for each specific block copolymer composition and the iteration process of degrees of polymerization tested needs to be exacting down to single digits. It is likely that the difference to achieve the best catalyst performance could be one monomer unit.

Chapter 6: Conclusions

6.1 Overview

As presented in Chapters 2 to 5, we have been able to produce a reliable Fe-doping method to synthesize CTNC into an Fe-N-C catalyst that works significantly well as a PGM-free fuel cell catalyst. We were able to use the nitrogen content in CTNC to form FeN_x moieties that serve as active sites for ORR in an acidic environment and the carbon nanostructure was retained despite the use of multiple processing steps that included heat treatments and acid washing. This was done using PAN₁₀₃-b-PBA₆₀, and approximately 160 catalyst samples were synthesized to test different Fe-doping methods. The best results obtained with this block copolymer were a half-wave potential of 0.781 V vs NHE, a mass activity of 0.565 A/g and a capacitive surface area of 798 m²/g. The nanostructure retention was confirmed using TEM imaging and BET surface area and although there was some loss of surface area, especially micropore surface area, the mesopore structure remained mostly intact in terms of negative effects by the Fe-doping process. The catalyst synthesis process, however, produced large particles over 10 μm in width which was the likely cause behind the high ohmic overpotential displayed during the fuel cell tests. This is a point where the catalyst synthesis process requires improvement and a focus of future work.

Furthermore, through testing the effects of various block copolymers with different compositions and degrees of polymerization (different block lengths with a similar AN to BA ratio) we found that we can influence the formation of active sites through the control of the block copolymer composition. Although density of sites and overall chemical composition of each catalyst has not been measured, the surface area elemental analysis performed using XPS showed that the Fe moieties of PAN₇₆-b-PBA₄₇ had the most advantageous binding energies in terms of

most active Fe moiety having the smallest energy barrier for activation. Furthermore, this catalyst also showed a significantly larger graphitic phase, meaning its electrical conductivity is greater than that of the other catalysts which reduces ohmic overpotential in ORR. Although pore size and volume seem to have some effects on improving electrochemical activity as shown by the electrochemical activity results for PAN₁₆₅-b-PBA₉₉, there appears to be an even greater, more complex effect intrinsic to the overall architecture of the nanostructure of the CTNC. Whether to produce greater Fe retention or dispersion during synthesis, or that the N content is better conducted towards the formation of active sites, or the nanostructure leads to more accessible locations for FeN_x active site formation, there is indeed an intrinsic relationship between the formation of active sites and the CTNC pore morphology.

Finally, we were able to develop a new method of Fe-doping through the use of poly(vinyl ferrocene), a metallopolymer used to improve the dispersion of Fe moieties and prevent the formation of large, electrochemically inactive particles in the catalyst. Although this method still has not produced a better electrochemical activity than the one using FeSO₄ salt, we were able to improve the electrochemical activity relatively quickly. We have only tested approximately 40 samples using this method and have already reached a half-wave potential of 0.77 V vs NHE, whereas it took much longer to get to this level of activity when developing the method using FeSO₄. This could be partially attributed to the experience on handling CTNC we acquired when testing FeSO₄ before, however, it cannot be denied that the use of a metallopolymer allows for a more intuitive and predictable result that cannot be matched by the aqueous solution heat stirring methods using Fe salts.

The overall performance of CTNC-Fe has shown promise and as seen in Fig. 6.1, it is already a competent alternative when compared to other PGM-free catalysts. Some of them have

been in development for over 10 years, and since CTNC-Fe has only been under development for approximately 4 years, it is very likely that if it continues to improve, we will soon be able to compete if not overcome some of the best examples. Our hope for our catalyst to reach the level of activity of Pt/C catalysts and be able to make hydrogen fuel cells an affordable alternative to energy storage and conversion technologies.

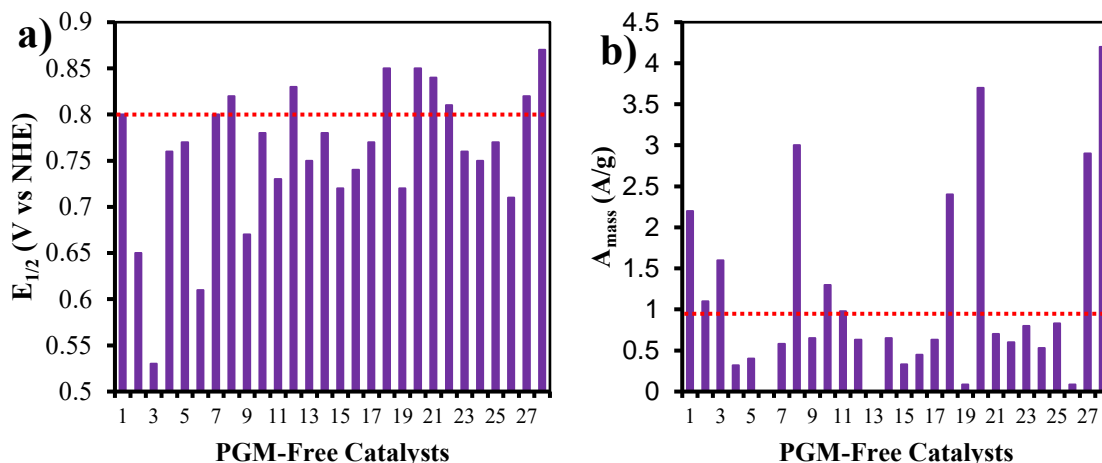


Figure 6.1. Electrochemical performance of other PGM-free catalysts currently under development. The red line represents the highest performance of CTNC-Fe. a) Half-wave potentials, b) Mass Activities.

6.2 Contributions

This dissertation made the following contributions:

1. *Explored the use of copolymer templated nitrogen rich carbon as a precursor for PGM-Free catalyst synthesis and its effectiveness.*

The use of CTNC is a new method of PGM-free catalyst synthesis introduced in this work and as such it was up to us to explore the capabilities of the copolymer and the feasibility of the

process. Our work will provide with a significant amount of nitrogen available for the generation of active sites, especially used in conjunction with other nitrogen sources.

- 2. Developed a reliable method of Fe-doping copolymer templated nitrogen rich carbon to synthesize an Fe-N-C catalyst for hydrogen proton exchange membrane fuel cells.*

Although this method of Fe-doping will doubtlessly be improved as the research progresses, we have been able to develop a method to convert CTNC into a working PGM-free fuel cell catalyst that has been tested in standard fuel cell conditions. This method of Fe-doping did not only generate the desired active sites known for ORR catalytic activity but also allowed for the retention of the pore morphology of the CTNC.

- 3. Confirmed the ability to affect the electrochemical activity of CTNC-Fe catalysts by control of pore morphology through the tuning of copolymer degree of polymerization and composition.*

One of the main methods used for improving the electrochemical activity of Fe-N-C catalysts is usually the Fe-doping process which creates the active sites on the carbon surface area. Though, there has been theoretical work with the conjecture that the pore morphology greatly affects the formation of active sites, there has not been much experimental work performed that confirms this theory. With the use of CTNC, we can tune the porous structure of the carbon by control of the block copolymer degree of polymerization and composition. Our experiments confirmed that when the pore morphology is the only variable in the synthesis we can vary the formation of active sites in the catalyst.

- 4. Developed a novel synthesis method that addresses the issue of lack of control of pore morphology and pore size in PGM-free fuel cell catalysts.*

Recently, there has been a great deal of research to study the nature of the catalytic active sites of PGM-free catalysts. Many works have concluded that a certain pore morphology and pore size is greatly beneficial for the formation of the active sites and their availability during the catalytic process. Through our work, we have made not only experimentally confirmed these assertions but have developed a method to make it possible to control the pore morphology of the catalyst. This is thanks to the use of a carbon base synthesized from a block copolymer made using controlled/ “living” radical polymerization which for decades has allowed for the control of the length and composition of polymers with many different applications. The use of this advanced polymerization technique, which is also highly scalable, may be the solution to the limitations of current PGM-free catalysts.

- 5. Developed a new form of Fe-doping carbon using the metallopolymer poly(vinyl-ferrocene) as the source of iron.*

According to the research literature, most PGM-free catalyst synthesis methods use a transition metal containing salt as the iron source. Except for those using MOF formation, the salt is expected to disperse throughout the surface of the carbon, however, there are issues with formation of particles. Poly(vinyl ferrocene) is meant to alleviate this problem although more work is needed to make it work with CTNC.

6.3 Future Work

The nature of PGM-free catalyst research and development is very trial-and-error reliant, and our catalyst is no different. We have worked on it for over for years and we continue to see improvements, although by small steps. There are many methods that we have attempted but were unable to see little to no improvements over the overall catalyst performance. But this is not

necessarily because they did not work. There is a process of testing where we can only include one variable at the time so that a pattern in improvement can be connected to the specific variable used each time. There have been times when we have been able to observe a small improvement over the use of a specific precursor or process but were unable or have yet to include this step into the overall best method of synthesis. This was a necessary form of testing which was used because we had a limited amount of block copolymer and could not afford to perform a complete union of different processes due to either lack of block copolymer, lack of time or other resources. Other times, simply the process or precursor worked well in a control sample but was affected by other variables or processes in the overall synthesis process. Herein, we discuss future work which includes some of these processes that have not yet been properly included in the overall synthesis.

6.3.1 Using Additional Nitrogen Source in the Synthesis

Chapter 2 focused on the development of the best Fe-doping method to synthesize an Fe-N-C catalyst from use of PAN-b-PBA block copolymers as a base. This took most of the time spent on this research since there are so many ways to introduce iron into the system. However, there are still many options to test such as Fe-porphyrin which already has the desired molecular structure of FeN₄ for active sites and has been tested before with promising results.¹⁰⁹ Inclusion of this iron source would not even be limited to a sol-gel solution type such as has been done with FeSO₄, but there is a possibility of including this into the polymer during precipitation and perhaps even co-polymerized into the PAN or PBA blocks. In addition, there are iron acetate and iron nitrate which have often been used in Fe-N-C catalyst solution in other processes before.⁸⁻¹⁶

On the other hand, we have neglected to include other nitrogen sources into the synthesis process. CTNC provides an advantage in this regard because it is a carbon that already has a rich nitrogen content. But as observed in Chapter 3, we retained about a third of the nitrogen content

initially present in material after heat treatment at 600 °C. This is because we are heat treating the catalyst material at 900 °C for three hours to increase electrical conductivity, however, as measured before using XPS the nitrogen content and electrical conductivity of CTNC are inversely proportional.⁷³ This is understandable since to have good electrical conductivity, CTNC must form a graphitic phase which can be impeded by presence of heteroatoms such as nitrogen. Therefore, to make up for this loss at high temperatures we need to make up for the loss by including an additional N source. Some tests have been performed before, during the first months of experimentation with CTNC, using cyanamide and aniline though these were not fully studied and have yet to be integrated into a process that can improve the overall performance of the catalyst.

6.3.2 Use of Surface Area Activation Methods

Retention of nanostructure throughout the Fe-N-C synthesis process was a major goal of this work and it was achieved. But if we want to improve the electrochemical activity of the catalyst a higher surface area is necessary. CTNC has been subjected to surface area activation before and it has been found that too intensive methods of surface area activation such as KOH soaking do destroy the nanostructure.⁷¹ Other methods, like heat treatment with carbon dioxide have produced better results. We have tested the use of ZnCl₂ on CTNC-Fe catalyst before and have observed small increases in half-wave potential of approximately 10-20 mV. These experiments were previously performed on CTNC-Fe made with PAN_{103-b}-PBA₆₀, synthesized with a now obsolete Fe-doping process.

The best performance with surface activation was achieved with a mixture of 1:10 ZnCl₂ to CTNC-Fe catalyst in 5 mL ultra-pure water, stirred for 12 hours and heat stirred till evaporation. The product was dried for 4 hours in air at 60 °C right before final heat treatment at 900 °C. The performance of the catalyst went up from 0.74 to 0.76 V vs NHE after surface area treatment. It is

likely that this process will need to be improved when integrating with the current best Fe-doping process, but it should not be too time consuming and after having achieved 0.8 V vs NHE, any improvement to the electrochemical activity will be significant.

6.3.3 Reducing Catalyst Particle Size

As seen in Chapter 3, particle size of CTNC-Fe catalyst is relatively large when compared to other PGM-free catalysts. The high ohmic overpotential measured in the fuel cell test is likely a consequence of the particle size. We have attempted to reduce particle size by using more intensive methods of comminution: varying the ball size and using harder ball materials for ball-milling. This has, unfortunately, produced a slightly lower performance in RDE potentiometry tests (approximately 20 mV lower). BET surface area analysis performed on these samples show a significant reduction in surface area of about 30 %, so it is likely that more intensive ball-milling is destroying some of the pore structure. This, however, was the case when using PAN₁₀₃-*b*-PBA₆₀ as the CTNC so it may produce better results with catalyst samples synthesized from lower degree of polymerization BCPs.

6.3.4 Composition Analysis of CTNC-Fe Catalysts

As seen in Chapter 5, there is a difference in performance when using BCPs with different degrees of polymerization. XPS pointed to the ionization of the Fe content being a factor, however, there is likely to be more causes for the results. Although XPS measured the amount of nitrogen in the surface of the catalyst, overall N content could be significantly different as well and maybe a cause of the differences in performance. Therefore, it would be prudent to send some samples to MidWestMicro Lab again to measure the amount of nitrogen in each catalyst sample. XPS also showed some major differences in carbon types so calculating the amount of graphitic versus amorphous carbon may explain the results.

Finally, using an extremely sensitive form of chemical analysis such as Mossbauer Spectroscopy could help give a rough count on active sites so it should be a priority.

6.3.5 Fuel Cell Testing

As seen in Chapter 3, fuel cell tests did not show very high electrochemical activity in our catalyst. Now though we have improved on the old catalyst by reaching an electrochemical activity of 0.8 V vs NHE, so the next step is to test this in a fuel cell to see how much our catalyst has improved when tested in conditions that simulate a more life-like scenario. Furthermore, it is probable that the pore morphology of CTNC-Fe made using PAN₁₆₅-*b*-PBA₉₉ will produce much better results as the pore size is much larger and will likely aid in mass transport so we could learn more about the effects of different catalyst pore morphology with a fuel cell test of each. In addition, until we can reduce particle size without negatively affecting the electrochemical activity of the catalyst it may be prudent to design an electrode casting and membrane electrode assembly more suited to this catalyst.

6.3.6 Testing Other BCP Degrees of Polymerization

As seen in Chapter 5, the pore morphology of the CTNC has a great effect on the formation of active sites and the electrochemical activity of the CTNC-Fe catalyst. From our current results, we found that PAN₇₆-*b*-PBA₄₇ produces the best electrochemical activity results when using the current Fe-doping process. But we have only performed four data points overall, therefore, if we want to find the optimal pore size and pore morphology that works the best for our CTNC-Fe catalyst we need to test at least a few more BCP compositions. Furthermore, having more data points will be greatly beneficial to strengthen our conclusions on the effects of pore morphology.

6.3.7 Optimization of Fe-doping Process for each Type of CTNC

Although we have spent over three years developing the Fe-doping process for synthesizing CTNC into an Fe-N-C fuel cell catalyst, this was done using one type of BCP: PAN₁₀₃-*b*-PBA₆₀. It is highly probable that this specific process may not be the best method for CTNC-Fe's made with BCPs with different compositions and degrees of polymerization. Chapter 5 shows that the iron contents of all CTNC-Fe's are different, so it is possible that because of the differences in pore size, surface area and pore volume each CTNC-Fe may work better when the Fe-doping process is optimized for each specific BCP. This does not mean that it will take as long as it has for PAN₁₀₃-*b*-PBA₆₀ since a lot of the time spent working on it was in trying to figure out how best to handle these materials in a new application. Therefore, the ab initio stage has long been surpassed so most of the optimization on other BCPs would take the form of optimizing the iron content, the level of comminution and the acid treatment.

6.3.8 Optimization of the Fe-doping Process using Poly(vinyl-ferrocene)

Fe-doping performed with vinyl ferrocene has only been tested a few times. Given its results which such few samples made there is a possibility that it could potentially produce even better results if we are able to optimize the process. As observed in Chapter 4, currently the process is causing some reduction in mesoporous surface area which is probably due to the use of high solution concentration used during injection. We also have only used this process on one type of BCP, PAN₁₀₃-*b*-PBA₆₀, since that was the only one we had available. Therefore, the next steps will involve using lower polymerization solution concentrations (lower than 25 wt%) but multiple injections to achieve the same Fe content of the best performing sample. In addition, we need to test this process on the other BCPs and observe how each react to this specific type of Fe-doping process.

References

- [1] Trogadas, P., Ramani, V., Strasser, P., Fuller, T.F., Coppins, M.-O., 2016, “Hierarchically Structured Nanomaterials for Electrochemical Energy Conversion,” *Angewandte Chemie Int. Ed.*, 55, pp. 122-148.
- [2] Budischak, C., Sewell, D., Thomson, H., Mach, L., Veron, D. E., Kempton, W., 2013, “Cost-Minimized Combinations of Wind Power, Solar Power and Electrochemical Storage, Powering the Grid up to 99.9% of the Time,” *Journal of Power Sources*, 225, pp. 60-74.
- [3] Zhu, Y. P., Guo, C., Zheng, Y., Qiao, S.-Z., 2017, “Surface and Interface Engineering of Noble-Metal-Free Electrocatalysts for Efficient Energy Conversion Processes,” *Accounts of Chemical Research*, 50, pp. 915-923.
- [4] Miranda, P.E., 2018, “Science and Engineering of Hydrogen Based Energy Technologies,” Amsterdam: Elsevier.
- [5] Martinez, U., Babu, S. K., Holby, E. F., Chung, H. T., Yin, X., Zelenay, P., 2019, “Progress in the Development of Fe-Based PGM-Free Electrocatalysts for the Oxygen Reduction Reaction,” *Advanced Materials*, 31, pp. 1806545.
- [6] Carmo, M., Fritz, E. L., Mergel, J., Stolten, D., 2013, “A Comprehensive Review on PEM Water Electrolysis,” *International Journal of Hydrogen Energy*, 38, pp. 4901-4934.
- [7] Papageorgopoulos, D., 2018, “Merit Review and Peer Evaluation Meeting in the U.S. Department of Energy,” Washington DC, Office of Energy Efficiency and Renewable Energy, Fuel Cell Technologies Program.
- [8] Barkholtz, H. M., Liu, D.-J., 2017, “Advancements in Rationally Designed PGM-Free Fuel Cell Catalysts Derived from Metal-Organic Frameworks,” *Materials Horizons*, 4, pp. 20-37.

- [9] Chen, M., He, Y., Spendelow, J. S., Wu, G., 2019, "Atomically Dispersed Metal Catalysts for Oxygen Reduction," *ACS Energy Letters*, 4, pp. 1619-163.
- [10] Wu, G., Santandreu, A., Kellogg, W., Gupta, S., Ogoke, O., Zhang, H., Wang, H.-L., Dai, L., 2015, "Carbon Nanocomposite Catalysts for Oxygen Reduction and Evolution Reactions: From Nitrogen Doping to Transition Metal Addition," *Nano Energy*, 29, pp. 83-110.
- [11] Wu, G., 2017, "Current Challenge and Perspective of PGM-Free Cathode Catalysts for PEM Fuel Cells," *Front. Energy*, 11(3), pp. 286-298.
- [12] Thompson, S. T., Wilson, A. R., Zelenay, P., Myers, D. J., More, K. L., Neyerlin, K. C., Papageorgopoulos, D., 2018, "ElectroCat: DOE's Approach to PGM-Free Catalyst and Electrode R&D," *Solid State Ionics*, 319, pp. 68-76.
- [13] Shao, Y., Dodelet, J.-P., Wu, G., Zelenay, P., 2019, "PGM-Free Cathode Catalysts for PEM Fuel Cells: A Mini-Review on Stability Challenges," *Advanced Materials*, 31, pp. 1807615.
- [14] Jaouen, F., Proietti, E., Lefevre, M., Chenitz, R., Dodelet, J.-P., Wu, G., Chung, H. T., Johnston, C. M., Zelenay, P., 2011, "Recent Advances in Non-Precious Metal Catalysis for Oxygen-Reduction Reaction in Polymer Electrolyte Fuel Cells," *Energy & Environmental Science*, 4, pp. 114-130.
- [15] Osmieri, L., 2019, "Transition Metal-Nitrogen-Carbon (M-N-C) Catalysts for Oxygen Reduction Reaction. Insights on Synthesis and Performance in Polymer Electrolyte Fuel Cells," *ChemEngineering*, 3, pp. 16-48.
- [16] Shen, M., Wei, C., Ai, K., Lu, L., 2017, "Transition Metal-Nitrogen-Carbon Nanostructured Catalysts for the Oxygen Reduction Reaction: From Mechanistic Insights to Structural Optimization," *Nano Research*, 10(5), pp. 1449-1470.

- [17] Artyushkova, K., Serov, A., Rojas-Carbonell, S., Atanassov, P., 2015, “Chemistry of Multitudinous Active Sites for Oxygen Reduction Reaction in Transition Metal-Nitrogen-Carbon Electrocatalysts,” *J. Phys. Chem. C*, 119, pp. 25917–25928.
- [18] Capuano, C. B., Yamaguchi, S., Mukerjee, S., Kishi, H., Artyushkova, K., Atanassov, P., Serov, A., Sakamoto, T., Danilovic, N., Doan, H., 2019, “Application of X-Ray Photoelectron Spectroscopy to Studies of Electrodes in Fuel Cells and Electrolyzers,” *J. Electron Spectroscopy and Related Phenomena*, 231, pp. 127–139.
- [19] Chen, Y., Artyushkova, K., Rojas-Carbonell, S., Serov, A., Matanovic, I., Santoro, C., Asset, T., Atanassov, P., 2018, “Inhibition of Surface Chemical Moieties by Tris(Hydroxymethyl)Aminomethane: A Key to Understanding Oxygen Reduction on Iron–Nitrogen–Carbon Catalysts,” *ACS Applied Energy Materials*, 1, pp. 1942–1949.
- [20] Workman, M. J., Serov, A., Tsui, L. K., Atanassov, P., Artyushkova, K., 2017, “Fe-N-C Catalyst Graphitic Layer Structure and Fuel Cell Performance,” *ACS Energy Letters*, 2, pp. 1489–1493.
- [21] Jasinski, R., 1964, “A New Fuel Cell Cathode Catalyst,” *Nature*, 201, pp. 1212–1213.
- [22] Kaila, V. R. I., Verkhovsky, M. I., Wikstrom, M., 2010, “Proton-Coupled Electron Transfer in Cytochrome Oxidase,” *Chemical Reviews*, 110, pp. 7062-7081.
- [23] Subramanian, N. P., Li, X., Nallathambi, V., Kumaraguru, S. P., Colon-Mercado, H., Wu, G., Lee, J.-W., Popov, B. N., 2009, “Nitrogen Modified Carbon-Based Catalysts for Oxygen Reduction Reaction in Polymer Electrolyte Membrane Fuel Cells,” *Journal of Power Sources*, 188, pp. 28-44.

- [24] Qiao, J.; Xu, L.; Ding, L.; Zhang, L.; Baker, R.; Dai, X.; Zhang, J. Using Pyridine as Nitrogen-Rich Precursor to Synthesize Co-N-S/C Non-Noble Metal Electrocatalysts for Oxygen Reduction Reaction. *Applied Catalysis B: Environmental*, 125, 197-205.
- [25] Jaouen, F., Carreteur, F., Dodelet, J. P., 2006, "Fe-Based Catalysts for Oxygen Reduction Reaction in PEMFCs," *Journal of the Electrochemical Society*, 153(4), pp. A689-A698.
- [26] Osmieri, L., Escudero-Cid, R., Armandi, M., Monteverde Videla, A. H. A., Garcia Fierro, J. L., Ocon, P., Specchia, S., 2017, "Fe-N/C Catalysts for Oxygen Reduction Reaction Supported on Different Carbonaceous Materials. Performance in Acidic and Alkaline Direct Alcohol Fuel Cells," *Applied Catalysis B: Environmental*, 205, pp. 637-653.
- [27] Schilling, T., Bron, M., 2008, "Oxygen Reduction at Fe-N-Modified Multi-Walled Carbon Nanotubes in Acidic Electrolyte," *Electrochimica Acta*, 53, pp. 5379-5385.
- [28] Byon, H. R., Suntivich, J., Shao-Horn, Y., 2011, "Graphene-Based Non-Noble-Metal Catalysts for Oxygen Reduction Reaction in Acid," *Chemistry of Materials*, 23, pp. 3421-3428.
- [29] Zhang, L., Kim, J. D. E., Ban, S., Tsay, K.-C., Kawai, H., Shi, Z., Zhang, J., 2013, "Synthesis of Novel Mesoporous Carbon Spheres, and their Supported Fe-Based Electrocatalysts for PEM Fuel Cell Oxygen Reduction Reaction," *Electrochimica Acta*, 108, pp. 480-485.
- [30] Wu, G., More, K. L., Xu, P., Wang, H.-L., Ferrandon, M., Kropf, A. J., Myers, D. J., Ma, S., Johnston, C. M., Zelenay, P., 2013, "A Carbon-Nanotube-Supported Graphene-Rich Non-Precious Metal Oxygen Reduction Catalysts with Enhanced Performance Durability," *Chemical Communications*, 49, pp. 2391-3293.
- [31] Chokai, M., Taniguchi, M., Moriya, S., Matsubayashi, K. S. T., Nabae, Y., Kuroki, S., Hayakawa, T., Kakimoto, M.-A., Ozaki, J.-I., Miyata, S., 2010, "Preparation of Carbon Alloy

- Catalysts for Polymer Electrolyte Fuel Cells from Nitrogen-Containing Rigid-rod Polymers,” *Journal of Power Sources*, 195, pp. 5947-5951.
- [32] Wang, M., Woo, K., Lou, T., Zhai, Y. K. D., 2005, “Defining Catalyst Layer Ingredients in PEMFC by Orthogonal Test and C-V Method,” *International Journal of Hydrogen Energy*, 30, pp. 381-384.
- [33] Ding, S. Y., Wang, W., 2013, “Covalent Organic Frameworks (COFs): from Design to Applications,” *Chemical Society Reviews*, 42, pp. 548-568.
- [34] Lu, S., Jin, Y., Gu, H., Zhang, W., 2017, “Recent Development of Efficient Electrocatalysts Derived from Porous Organic Polymers for Oxygen Reduction Reaction,” *Science China Chemistry*, 60, pp. 1000-1006.
- [35] Day, N. U., Wamser, C. C., Walter, M. G., 2015, “Porphyrin Polymers and Organic Frameworks,” *Polymers Int*, 64, pp. 833-857.
- [36] Wang, Q., Zhou, Z.-Y., Lia, Y.-J., You, Y., Liu, J.-G., Wu, X.-L., Terefe, E., Chen, C., Song, L., Rauf, M., Sun, S.-G., 2014, “Phenelynediamine-Based FeN_x/C Catalyst with High Activity for Oxygen Reduction in Acid Medium and its Active-Site Probing,” *Journal of the American Chemical Society*, 136, pp. 10882-10885.
- [37] Wang, Y.-C., Lai, Y., Song, L., Zhou, Z.-Y., Liu, J., Wang, Q., Yang, X. D., Chen, C., Shi, W., Zheng, Y.-P., Rauf, M., Sun, S.-G., 2015, “S-Doping of an Fe/N/C ORR Catalyst for Polymer Electrolyte Membrane Fuel Cells with High Power Density,” *Angewandte Chemie Int. Ed.*, 54, pp. 9907-9910.
- [38] Zhao, D., Shui, J.-L., Grabstanowicz, L. R., Chen, C., Commet, S. M., Xu, T., Lu, J., Liu, D.-J., 2014, “Highly Efficient Non-Precious Metal Electrocatalysts Prepared from One-Pot Synthesized Zeolitic Imidazolate Frameworks,” *Advanced Materials*, 26, pp. 1093-1097.

- [39] Ma, S., Goenaga, G. A., Call, A. V., Liu, D.-J., 2011, "Cobalt Imidazolate Framework as Precursor for Oxygen Reduction Reaction Electrocatalysts," *Chem. Eur. J.*, 17, pp. 2063-2067.
- [40] Gross, A. F., Sherman, E., Vajo, J. J., 2012, "Aqueous Room Temperature Synthesis of Cobalt and Zinc Sodalite Zeolitic Imidazolate Frameworks," *Dalton Transactions*, 41, pp. 5458.
- [41] Zhao, D., Shui, J.-L., Chen, C., Chen, C., Chen, X., Reprogie, B. M., Wang, D., Liu, D.-J., "Iron Imidazolate Framework as Precursor for Electrocatalysts in Polymer Electrolyte Membrane Fuel Cells," *Chemical Science*, 3, pp. 3200.
- [42] Chen, Y.-Z., Wang, C., Wu, Z.-Y., Xiong, Y., Xu, Q., Yu, S.-H., Jiang, H.-L., 2015, "From Bimetallic Metal-Organic Framework to Porous Carbon: High Surface Area and Multicomponent Active Dopants for Excellent Electrocatalysis," *Advanced Materials*, 27, pp. 5010-5016.
- [43] Tian, J., Morozan, A., Sougrati, M. T., Lefevre, M., Chenitz, R., Dodelet, J.-P., Jones, D., Jaouen, F., 2013, "Optimized Synthesis of Fe/N/C Cathode Catalysts for PEM Fuel Cells: A Matter of Iron-Ligand Coordination Strength," *Angewandte Chemie Int. Ed.*, 52, pp. 6867-6870.
- [44] Lefèvre, M., Proietti, E., Jaouen, F., Dodelet, J.P., 2009, "Iron-Based Catalysts with Improved Oxygen Reduction Activity in Polymer Electrolyte Fuel Cells," *Science*, 324, pp. 71-74.
- [45] Kramm, U. I., Herranz, J., Larouche, N., Arruda, T. M., Lefèvre, M., Jaouen, F., Bogdanoff, P., Fiechter, S., Abs-Wurmbach, I., Mukerjee, S., Dodelet, J.-P., 2012, "Structure of the

- catalytic sites in Fe/N/C-catalysts for O₂-reduction in PEM fuel cells,” *Phys. Chem. Chem. Phys.*, 14, pp. 11673–11688.
- [46] Artyushkova, K., Rojas-Carbonell, S., Santoro, C., Weiler, E., Serov, A., Awais, R., Gokhale, R. R., Atanassov, P., 2019, “Correlations between synthesis and performance of Fe-Based PGM-free catalysts in acidic and alkaline media: evolution of surface chemistry and morphology,” *ACS Applied Energy Materials*, 2, pp. 5406-5418.
- [47] Wan, X., Liu, X., Shui, J., 2020, “Stability of PGM-free fuel cell catalysts: Degradation mechanisms and mitigation strategies,” *Progress in Natural Science: Materials Int.*, 30, pp. 721-731.
- [48] Szakacs, C. E., Lefevre, M., Kramm, U. I., Dodelet, J.-P., Vidal, F., 2014, “A Density Functional Theory Study of Catalytic Sites for Oxygen Reduction in Fe/N/C Catalysts used in H₂/O₂ Fuel Cells,” *Phys. Chem. Phys. Chem.*, 16, pp. 13654.
- [49] Kattel, S., Wang, G., 2013, “A Density Functional Theory Study of Oxygen Reduction Reaction on Me-N₄ (Me = Fe, Co, or Ni) Clusters Between Graphitic Pores.,” *J. Mater. Chem. A*, 1, pp. 10790.
- [50] Lamson, M., Kopec, M., Ding, H., Zhong, M., Matyjaszewski, K., 2016, “Synthesis of Well-Defined Polyacrylonitrile by ICAR ATRP with Low Concentrations of Catalyst,” *J. of Polymer Science*, 54, pp. 1961-1968.
- [51] Espinoza, E. M., Clark, J. A., Soliman, J., Derr, J. B., Morales, M. V. V. I., 2019, “Practical Aspects of Cyclic Voltammetry: How to Estimate Reduction Potentials When Irreversibility Prevails,” *J. Electrochem. Soc.*, 166, pp. H3175-H3187.

- [52] Lukaszewski, M., Soszko, M., Czerwinski, A., 2016, "Electrochemical Methods of Real Surface Area Determination of Noble Metal Electrodes – an overview," *Int. J. Electrochem. Sci.*, 11, pp. 4442-4469.
- [53] Beltran, D. E., Litster, S., 2019, "Half-Wave Potential or Mass Activity? Characterizing Platinum Group Metal-Free Fuel Cell Catalysts by Rotating Disk Electrodes," *ACS Energy Letters*, 4, pp. 1158-1161.
- [54] Chung, H. T., Johnston, C. M., Artyushkova, K., Ferrandon, M., Myers, D. J., Zelenay, P., 2010, "Cyanamide-Derived Non-Precious Metal Catalyst for Oxygen Reduction," *Electrochem. Comm.*, 12, pp. 1792-1795.
- [55] Peng, H. M. Z., Liao, S., Liang, H., Yang, L., Luo, F., Song, H., Zhong, Y., Zhang, B., 2013, "High Performance Fe- and N- Doped Carbon Catalyst with Graphene Structure for Oxygen Reduction," *Sci. Reports*, 3, pp. 1765-1771.
- [56] Wu, G., More, K. L., Johnston, C. M., Zelenay, P., 2011, "High-Performance Electrocatalysts for Oxygen Reduction Derived from Polyaniline, Iron, and Cobalt," *Science*, 332, pp. 443-449.
- [57] Wu, G., Johnston, C. M., Mack, N. H., Artyushkova, K. F. M., Nelson, M., Lezama-Pacheco, J. S., Conradson, S. D., More, K. L., Myers, D. J., Zelenay, P., 2011, "Synthesis-Structure-Performance Correlation for Polyaniline-Me-C Non-Precious Metal Cathode Catalysts for Oxygen Reduction in Fuel Cells," 2011, *J. of Mat. Chem.*, 21, pp. 11392.
- [58] Ferrandon, M., Kropf, A. J., Myers, D. J., 2012, "Multitechnique Characterization of Polyaniline-Iron-Carbon Oxygen Reduction Catalyst," *ACS J. of Phys. Chem.*, 116, pp. 16001-16013.

- [59] Wu, G., Artyushkova, K., Ferrandon, M., Kropf, J. M. D., Zelenay, P., 2009, "Performance Durability of Polyaniline-Derived Non-Precious Cathode Catalysts," *ECS Trans.*, 25, pp. 1299-1311.
- [60] Stanczyk, K., Dziembaj, R., Piwowarska, Z., Witkowski, S., 1995, "Transformation of Nitrogen Structures in Carbonization Model Compounds Determined by XPS" *Carbon*, 33(10), pp. 1383-1392.
- [61] Martinez, U., Holby, E. F., Babu, S. K., Artyushkova, K., Lin, L., Choudhury, S., Purdy, G. M., Zelenay, P., 2019, "Experimental and Theoretical Trends of PGM-Free Electrocatalysts for the Oxygen Reduction Reaction with Different Transition Metals," *J. Electrochem. Soc.*, 166, pp. F3136-F3142.
- [62] Collman, J. P., Herrmann, P. C., Boitrel, B., Zhang, X., Eberspacher, T. A., Fu, L., 1994, "A Synthetic Analogue for the Oxygen Binding Site in Cytochrome c Oxidase," *J. Am. Chem. Soc.*, 116, pp. 9783-9784.
- [63] Collman, J. P., Eberspacher, T., Fu, L., Herrmann, P. C., 1997, "Functional Models for the Oxygen Binding/Activating Hemeproteins, Myoglobin and Cytochrome c Oxidase," *J. Mol. Catalysis A*, 117, pp. 9-20.
- [64] Thomas, A., Goettmann, F., Antonietti, M., 2008, "Hard templates for soft materials: Creating nanostructured organic materials," *Chem Mater*, 20 (3), pp. 738-755.
- [65] Kowalewski, T., Tsarevsky, N. V., Matyjaszewski, K., 2002, "Nanostructured Carbon Arrays from Block Copolymers of Polyacrylonitrile," *J. Am. Chem. Soc.* 124, pp. 10632-10633.
- [66] Hamley, I. W., 1998, *The Physics of Block Copolymers*, Oxford University Press, Oxford.

- [67] Bates, F. S., Fredrickson, G. H., 1999, "Block copolymers - Designer soft materials," *Phys. Today*, 52(2), pp. 32-38.
- [68] Mai, Y. Y., Eisenberg, A., 2021, "Self-assembly of block copolymers," *Chem Soc Rev*, 41(18), pp. 5969-5985.
- [69] Darling, S. B., 2007, "Directing the self-assembly of block copolymers," *Prog. Polym. Sci.*, 32, pp. 1152-1204.
- [70] Tang, C., Tracz, A., Kruk, M., Zhang, R., Smilgies, D.-M., Matyjaszewski, K., Kowaleski, T., 2005, "Long-Range Ordered Thin Films of Block Copolymers Prepared by Zone-Casting and Their Thermal Conversion into Ordered Nanostructured Carbon," *J. Am. Chem. Soc.*, 127, pp. 6918-6919.
- [71] Zhong, M., Kim, E. K., McGann, J. P., Chun, S.-E., Whitacre, J. F., Jaroniec, M., Matyjaszewski, K., Kowalewski, T., 2012, "Electrochemically Active Nitrogen-Enriched Nanocarbons with Well-Defined Morphology Synthesized by Pyrolysis of Self-Assembled Block Copolymer," *J. Am. Chem. Soc.*, 134, pp. 14846-14857.
- [72] Zhong, M., Tang, C., Kim, E. K., Kruk, M., Celer, E. B.; Jaroniec, M., Matyjaszewski, K., Kowalewski, T., 2014, "Preparation of Porous Nanocarbons with Tunable Morphology and Pore Size from Copolymer Templated Precursors," *Mater. Horiz.*, 1, pp. 121-124.
- [73] Zhong, M., Jiang, S., Tang, Y., Gottlieb, E., Kim, E. K., Star, A., Matyjaszewski, K., Kowalewski, T., 2014, "Block Copolymer-Templated Nitrogen-Enriched Nanocarbons with Morphology-Dependent Electrocatalytic Activity for Oxygen Reduction," *Chem. Sci.*, 5, pp. 3315-3319.
- [74] Kopeć, M., Yuan, R., Gottlieb, E., Abreu, C. M. R., Song, Y., Wang, Z., Coelho, J. F. J., Matyjaszewski, K., Kowalewski, T., 2017, "Polyacrylonitrile-b-poly(butyl acrylate) Block

- Copolymers as Precursors to Mesoporous Nitrogen-Doped Carbons: Synthesis and Nanostructure,” *Macromolecules*, 50, pp. 2759-2767.
- [75] Yuan, R., Wang, H., Sun, M., Damodaran, K., Gottlieb, E., Kopeć, M., Eckhart, K., Li, S., Whitacre, J., Matyjaszewski, K., Kowalewski, T., 2019, “Well-Defined N/S Co-Doped Nanocarbons from Sulfurized PAN-b-PBA Block Copolymers: Structure and Supercapacitor Performance,” *ACS Appl. Nano Mater.*, 2, pp. 2467-2474.
- [76] Yuan, R., Wang, H., Sun, M., Whitacre, J., Matyjaszewski, K., Kowalewski, T., 2020, “Copolymer-Derived N/B Co-Doped Nanocarbons with Controlled Porosity and Highly Active Surface,” *Journal of Polymer Science*, 58, pp. 225-232.
- [77] Matyjaszewski, K., 2012, “Atom Transfer Radical Polymerization (ATRP): Current Status and Future Perspectives,” *Macromolecules*, 45, pp. 4015-4039.
- [78] Matyjaszewski, K., 2018, “Advanced Materials by Atom Transfer Radical Polymerization,” *Adv. Mater.*, 30, pp. 1706441.
- [79] Wang, J.-S., Matyjaszewski, K., 1995, “Controlled/“living” Radical Polymerization. Atom Transfer Radical Polymerization in the Presence of Transition-Metal Complexes,” *J. Am. Chem. Soc.*, 117(20), pp. 5614-5615.
- [80] Kopeć, M., Lamson, M., Yuan, R., Tang, C., Kruk, M., Zhong, M., Matyjaszewski, K., Kowalewski, T., 2019, “Polyacrylonitrile-derived Nanostructured Carbon Materials,” *Progress in Poly. Sci.*, 92, pp. 89-134.
- [81] Bajaj, P., Roopanwal, A. K. J., 1997, “Thermal Stabilization of Acrylic Precursors for the Production of Carbon Fibers: An Overview,” *Journal of Macromol. Sci.*, C37, pp. 97-147.
- [82] Rufford, T. E., Hulicova-Jurcakova, D., Khosla, K., Zhu, Z., Lu, G. Q., 2010, “Microstructure and Electrochemical Double-Layer Capacitance of Carbon Electrodes

- Prepared by Zinc Chloride Activation of Sugar Cane Bagasse,” *J. Power Sources*, 195, pp. 912-918.
- [83] Yang, K., Peng, J., Srinivasakannan, C., Zhang, L., Xia, H., Duan, X., 2010, “Preparation of High Surface Area Activated Carbon from Coconut Shells Using Microwave Heating,” *Bioresource Tech.*, 101, pp. 6163-6169.
- [84] Buczek, B., 2016, “Preparation of Active Carbon by Additional Activation with Potassium Hydroxide and Characterization of Their Properties,” *Adv. Mat. Sci. Eng.*, pp. 2016.
- [85] Lee, K., Zhang, L., Lui, H., Hui, R., Shi, Z., Zhang, J., 2009, “Oxygen Reduction Reaction (ORR) Catalyzed by Carbon-Supported Cobalt Polypyrrole (Co-PPy/C) Electrocatalysts,” *Electrochimica Acta*, 54, pp. 4704-4711.
- [86] Villers, D., Jacques-Bedard, X., Dodelet, J.-P., 2004, “Fe-Based Catalysts for Oxygen Reduction in PEM Fuel Cells,” *J. ECS*, 151(9), pp. A1507-A1515.
- [87] Sha, H.-D., Yuan, X., Hu, X.-X., Lin, H., Wen, W., Ma, Z.-F., 2013, “Effects of Pyrrole Polymerizing Oxidant on the Properties of Pyrolyzed Carbon-Supported Cobalt-Polypyrrole as Electrocatalysts for Oxygen Reduction Reaction,” *J. ECS*, 160(6), pp. F507-F513.
- [88] Martinez Millan, W., Smit, M. A., 2009, “Study of Electrocatalysts for Oxygen Reduction Based on Electroconducting Polymer and Nickel,” *J. of Applied Pol. Sci.*, 112, pp. 2959-2967.
- [89] Yin, X., Chung, H. T., Martinez, U., Lin, L., Artyushkova, K., Zelenay, P., 2019, “PGM-Free ORR Catalysts Designed by Templating PANI-Type Polymers Containing Functional Groups with High Affinity to Iron,” *J. ECS*, 166(7), pp. F3240-F3245.

- [90] Chung, H. T., Cullen, D. A., Higgins, D., Sneed, B. T., Holby, E. F., More, K. L.; Zelenay, P., 2017, "Direct Atomic-Level Insight into the Active Sites of a High-Performance PGM-free ORR Catalyst," *Science*, 357, pp. 479-484.
- [91] Peng, H., Liu, F., Liu, X., Liao, S., You, C., Tian, X., Nan, H., Luo, F., Song, H., Fu, Z., Huang, P., 2014, "Effect of Transition Metals on the Structure and Performance of the Doped Carbon Catalysts Derived from Polyaniline and Melamine for ORR Application," *ACS Catal.*, 4, pp. 3797-3805.
- [92] Marshall-Roth, T., Libretto, N. J., Wrobel, A. T., Anderton, K. J., Pegis, M. L., Ricke, N. D., Voorhis, T. V., Miller, J. T.; Surendranath, Y., 2020, "A Pyridinic Fe-N₄ Macrocyclic Models the Active Sites in Fe/N-doped Carbon Electrocatalysts," *Nature Comm.*, 11, pp. 5283.
- [93] Zhang, J., Chen, J., Luo, Y., Chen, Y., Luo, Y., Zhang, C., Xue, Y., Liu, H., Wang, G., Wang, R., 2021, "A Defect-Driven Atomically Dispersed Fe-N-C Electrocatalyst for Bifunctional Oxygen Electrocatalytic Activity in Zn-air Batteries," *J. Mater. Chem. A.*, 9, pp. 5556.
- [94] Lesiak, B., Kover, L., Toth, J., Zemek, J., Jiricek, P., Kromka, A., Rangam, N., 2018, "C 2p²/sp³ Hybridisations in Carbon Nanomaterials – XPS and (X)AES Study," *Appl. Surf. Sci.*, 452, pp. 223-231.
- [95] Fonino, F., Brutti, S., Reale, P., Scrosatti, B., Ghergel, L., Wu, J., Mullen, K., 2005, "A Disordered Carbon as a Novel Anode Material in Lithium-Ion Cells," *Adv. Mater.*, 17, pp. 743-747.
- [96] Kinoshita, K., 1988, *Carbon: Electrochemical and Physicochemical Properties*, Wiley: NY.

- [97] Babu, S. K., Chung, H. T., Zelenay, P., Litster, S., 2017, "Modeling Electrochemical Performance of the Hierarchical Morphology of Precious Group Metal-Free Cathode for Polymer Electrolyte Fuel Cell," *J. of ECS*, 164(9), pp. F1037-F1047.
- [98] Wu, G., Chen, Z., Artyushkova, K., Garzon, F. H., Zelenay, P., 2008, "Polyaniline-Derived Non-Precious Catalyst for the Polymer Electrolyte Fuel Cell Cathode," *ECS Transac.*, 16, pp. 159-170.
- [99] Uddin, A., Dunsmore, L., Zhang, H., Hu, L., Wu, G., Litster, L., 2020, "High Power Density Platinum Group Metal-Free Cathodes for Polymer Electrolyte Fuel Cells," *ACS Appl. Mater. Interfaces*, 12, pp. 2216-2224.
- [100] Serov, A., 2020, "Active and Durable PGM-Free Cathodic Electrocatalysts for Fuel Cell Application," DOE Hydrogen and Fuel Cell Program Review.
- [101] Park, S. S., Chu, S.-W., Xue, C., Zhao, D., Ha, C.-S., 2011, "Facile Synthesis of Mesoporous Carbon Nitrides Using the Incipient Wetness Method and the Application as Hydrogen Adsorbent," *J. Mater. Chem.*, 21, pp. 10801.
- [102] Borchardt, L., Kockrick, E., Wollmann, P., Kaskel, S., 2010, "Ordered Mesoporous Boron Carbide Based Materials via Precursor Nanocasting," *Chem. Mater.*, 22, pp. 4660-4668.
- [103] Park, S. S., Choe, S. J., Park, D. H., 2003, "The Effect of Phosphate Treatment on Nickel Dispersion on MCM-41 Mesoporous Material," *Korean J. Chem. Eng.*, 20, pp. 256-261.
- [104] Choi, M., Ryoo, R., 2003, "Ordered Nanoporous Polymer-Carbon Composites," *Nature Mater.*, pp. 473-478.

- [105]Owens, D. K., 1970, "Some Thermodynamic Aspects of Polymer Adhesion," *J. Appl. Pol. Sci.*, 14, pp. 1725-1730.
- [106]Pyun, S. I., Rhee, C.-K., 2004, "An Investigation of Fractal Characteristics of Mesoporous Carbon Electrodes with Various Pore Structures," *Electrochimica Acta*, 49, pp. 4171-4180.
- [107]Katakoski, J., Krasheninnikov, A. V., Ma, Y., Foster, A. S., Nordlund, K., Nieminen, R. M., "B and N Implantation into Carbon Nanotubes: Insight from Atomistic Simulations," *Phys. Rev. B.*, 71, pp. 205408.
- [108]Ma, Y., Foster, A. S., Krasheninnikov, A. V., Nieminen, R. M., 2005, "Nitrogen in Graphite and Carbon Nanotubes: Magnetism and Mobility," *Phys. Rev. B.*, 72, pp. 205416.
- [109]Zion, N., Douglin, J. C., Cullen, D. A., Zelenay, P., Dekel, D. R., Elbaz, L., "Porphyrin Aerogel Catalysts for Oxygen Reduction Reaction in Anion-Exchange Membrane Fuel Cells," *Adv. Funct. Mater.*, 31, pp. 2100963.